Design, Modeling, Fabrication and Testing of a Membrane Piezoelectric Tactile Sensor with Four Sensing Elements

Ashkan Mirbagheri

A Thesis

in

The Department

of

Mechanical and Industrial Engineering

Presented in Partial Fulfillment of the Requirements

of the Degree of Master of Applied Science (Mechanical Engineering) at

Concordia University

Montreal, Quebec, Canada

April 2007

Your file Votre référence
ISBN: 978-0-494-34711-9
Our file Notre référence
ISBN: 978-0-494-34711-9

ABSTRACT

Design, Modeling, Fabrication and Testing of a Membrane Piezoelectric Tactile Sensor with Four Sensing Elements

Ashkan Mirbagheri

The fundamental requirement of a competent tactile sensor for manipulating an object is to determine the magnitude and the position of an applied force on it. In addition, it is important to determine orientation of the object in relation to the tactile sensor. In order to achieve these goals, most investigators have attempted to design a tactile sensor using an array of sensing elements arranged in matrix form. There are several problems associated with this type of tactile sensors. These problems include cross-talk between sensing elements, fragility, and complexity. This thesis reports on the design, modeling, fabrication and testing of a membrane tactile sensing system with only four sensing elements. By using membrane stress combined with triangulation approach, it is shown that it is possible to overcome the above problems. The prototype sensor consists of a single film of 25 micron thick Polyvinylidene Fluoride (PVDF) film, which is held between two 12 mm-thick flat Plexiglass plates, each with a 90 mm-diameter center hole. Four square sensing elements, each 3 mm side, were fabricated around the center of the membrane. The fabrication of the sensing elements is performed using photolithographic and etching techniques. By applying force with a probe of various shapes and sizes at various points away from the sensing elements, and using a geometric mapping process, the sensor is calibrated. As the result of calibration various isocharge contours were

drawn. Using both finite element and experimental analysis, it is shown that it is possible to determine the position, orientation and the magnitude of the applied load though various flat shaped probes, by using only four sensing elements. The experimental and the finite element results are compared. It is shown that there is a good correlation between the finite element predictions and experimental data.

ACKNOWLEDGEMENT

The path to a Master's degree has been an exciting and winding one. The route was not always well illuminated and at times it became very bumpy. Nonetheless, there have been many people who provided guidance and support along the way. I am grateful for their time, friendship, and words of wisdom.

First I would start thanking my supervisors, Dr. Javad Dargahi, Dr. Farhad Aghili and Dr. Kouroush Parsa for their invaluable support and suggestions at various stages of this research. Their support will be remembered time and again. I would also like to express my gratitude to the staff of micro-fabrication lab of Ecole Polytechnique school for their timely assistance.

I have been fortunate enough to work with some extremely talented and friendly members of the Tactile Sensors and Robotics Surgery Lab. I would like to express my sincere thanks to Mr. Mohammad Amin Changizi, Mr. Reza Ramezanifard, Mr. Saeed Sokhanvar and finally Mr. Alireza Hajimesgar for their assistance and friendly support during my research work.

Last, but by no means the least, I would express my sincerest gratitude, love to my parents and my family for their continuous motivation and emotional support. I would like to thank my mom Mrs. Fereshteh Mahdavi and my dad Mr. Mansour Mirbagheri

who taught me the value of patience, hard work and commitment without which I could not have completed my Master's degree.

TABLE OF CONTENTS

LIST OF FIGURES

LIST OF TABLES

Chapter 1 - Introduction and Literature Review

Out of the five human senses, two are used in robotic applications: vision and touch. The human being uses these senses as supplementary to each other. Vision is crucial in object identification and obstacle avoidance. It is considered as a prerequisite for locating, positioning, and identifying objects. The sense of touch, or tactile sensing, comes into picture either in parallel with vision or shortly afterwards. It takes over for subsequent manipulations whereby force, pressure, compliance, surface texture, and temperature become important parameters. There are numerous applications in which the above senses should be used, combined, and integrated properly. However, due to some practical considerations, the possibility of using vision is noticeably reduced in several important and frequent applications. Examples include some medical procedures such as endoscopy and surgery. While performing these procedures, the operator of the endoscopic device or the surgeon should greatly rely on his/her sense of touch. This is exactly when *tactile sensing* comes into the picture.

Tactile sensing is the process of determining physical properties through contact with objects [1]. Tactile sensors offer exciting possibilities for use in mechatronic devices and instrumentation in many areas of science and engineering. Robotics and industrial automation are the application areas that have generated the most interest because contact interactions are a fundamental feature of any physical manipulation system. However, there are many other potential application areas including minimally invasive surgery

(MIS), agriculture, food processing, medicine, dentistry, entertainment, and future domestic and service industries. Therefore, the dependence on tactile sensing and its resulting data processing will become more prominent.

Usually, two different kinds of grasps are defined: power grasps and precision grasps. Power grasps are typically used for larger objects and in tasks that do not require more than simple manipulation of the object. Grasping a chair to lift it is an example. The significant fact about a power grasp is that the object is held tight by the palm and as much finger area as possible. On the other hand, more delicate objects are typically held in a precision grasp. When lifting a glass, rotating an object, and in other precision tasks, the fingertips are primarily used for contact. The precision grasp has advantages such as enabling better control of contact forces, but it is also typically less stable than the power grasp. One important application area of precision grasp is MIS. Because of its nature, which incorporates both visual and tactile capabilities of the surgeons, any deficiency in one should be compensated with the other as much as possible. In MIS procedures, the tactile sensory perception is lessened. On the other hand, the success in any such procedure highly depends on the surgeon's ability in feeling the tissues and manipulating them. Considering these along with the fact that biological organs and tissues are delicate objects, it is important to develop methods by which these biological tissues could be handled safely and accurately. To this end, two physical parameters should be determined: the magnitude and the location of the applied force. The determination of these two parameters is the fundamental requirement of any competent robotic tactile sensor for manipulation purposes [1].

1.1. Polyvinylidene Fluoride and its applications in sensing

Although piezoelectricity was discovered by Jacques and Pierre Curie in 1880, Polyvinylidene Fluoride (PVDF) was the first polymer to be found, by Kawai in 1969 [2], to have such property. Two years later the pyroelectric effect in PVDF was found by Bergman et al. [3] and by Nakamura and Wada [4]. Both piezoelectric and pyroelectric effects have been observed in some other polymers such as vinylidene cyanide, polyurea, odd-numbered nylons, and polyvinylidene fluoride-trifluoroethylene copolymer (P(VDF-TrFE)). Among all these polymers only PVDF and P(VDF-TrFE) have found numerous applications. Some ferroelectric ceramics such as PZT-4 exhibit excellent properties such as high piezoelectric and pyroelectric coefficients. However, piezoelectric polymers such as PVDF posses some features which enhance their versatility and ease of application. For PVDF, those properties heavily outweigh its lower piezoelectric constants and pyroelectric coefficient. Like other polymers, PVDF can be fabricated in very thin, large sheets at relatively small costs. The thickness of PVDF sheets could be as low as 9μm [5]. The pie chart of Figure 1.1 shows the approximate distribution of papers published during the five-year period from 1999 through 2004 on various applications [6,7].

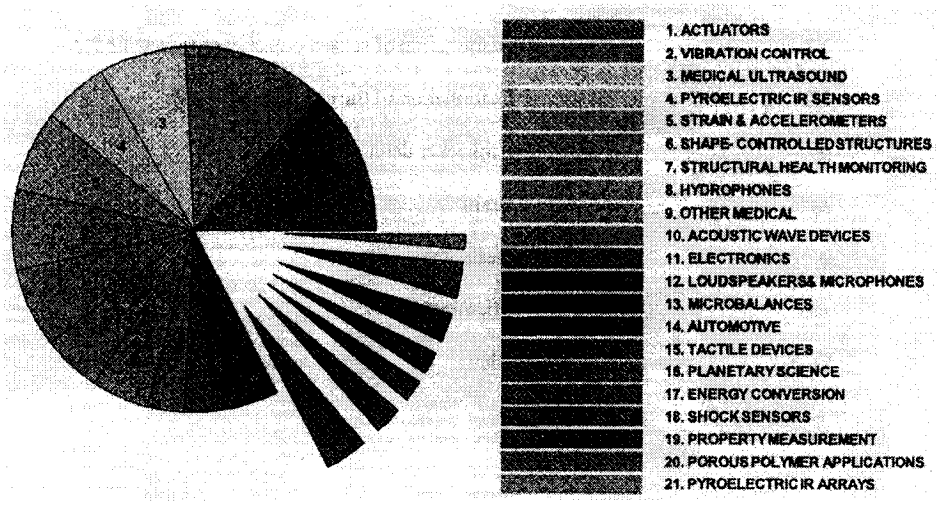

Figure 1.1 -- Pie chart showing piezoelectric and pyroelectric applications of eletroactive polymers between 1999 to 2004

The five most frequently areas of application are reported as actuators, vibration control, medical ultrasound, single-element pyroelectric infrared sensors, and finally strain and acceleration measurement devices. However, there are some other areas which are less known: tactile devices, energy conversion, porous polymers, property measurement, pyroelectric infrared sensors, shock sensors, and space science. As for tactile devices, PVDF has been used in developing a tri-axial pressure transducer for measuring tri-axial pressure inside shoes by Razian and Pepper [8]. The research was conducted in line with increasing awareness of the necessity to measure forces between the plantar surface of the foot and the shoe for the diagnosis and treatment of various foot disorders. In Japan, several groups developed tactile sensors for monitoring skin conditions using PVDF. Jiang et al. made a soft tribo-sensor that simulated a human finger [9]. A "haptic finger" was developed by Tanaka et al. which was translated across various fabrics as well as human skin of persons with diverse skin disorders [10]. The same group also developed an active palpation sensor for the detection of prostrate cancer and hypertrophy [11]. Its initial results were consistent with conventional medical examinations.

As in MIS, the desired data for the operators and surgeons is the ability to feel the tissue during the procedure. Therefore, a tactile sensor is required that can determine the magnitude of the applied force between the sensor and the tissue. Dargahi et al. developed an endoscopic grasper with a tooth-like structure formed of silicon [12,13]. It could find the magnitude of the applied force based on the magnitude of the output of PVDF. The position of the load was found from the slope of the output. Kim et al. presented the design, fabrication, and calibration of a piezoelectric polymer-based instrumented micro-gripper [14]. Experimental results it showed that it could successfully provide force feedback to the operator through the haptic device and play a main role in preventing damage to assembly parts. As for applications in energy conversion, Taylor et al. developed a device using piezoelectric polymers (more specifically, PVDF) for converting the mechanical flow energy available in oceans and rivers to electrical power [15]. It was noted by some researchers that vast amounts of industrial heat are emitted to the environment because of the unfavorable economics of recovering waste heat or converting it to more useful forms of energy. That drove Ikura [16,17] to study a system for direct conversion of low-grade waste heat to electricity using pyroelectric conversion based on the Olsen cycle [18].

Energy conversion in very small scales is also of interest. Shenk and Paradiso made a shoe generator by inserting a PVDF film under the insole of an athletic shoe [19]. They found out that the average power dissipated in a 250kΩ load at a 0.9Hz walking pace was 1.3mW. Sohn et al [20] considered the possibility of power generation in piezoelectric films that were subjected to fluctuating pressure sources such as human blood pressure. It

was observed that if the device was operated at a frequency closer to that of the human pulse rate, more energy could be harvested for the same applied pressure.

A soft piezoelectric transducer material made from cellular polymers has been recently developed [21-23]. A number of applications have been developed and commercialized in Finland such as push buttons for keyboards, keypads and control panels with small areas. Because the films are soft and flexible, various shapes of keyboards can be made [24]. In addition, some devices useful in nursing homes or hospitals have been devised. An example is a pad placed in front of a door that will signal an alarm if a person exits through the door [25]. This can be used to track persons with dementia. It can also be used as a fall sensor. A range of microphones and musical pickups can be constructed from the polymers. One example is a bridge-mounted transducer pickup for a double bass and a special stomp box mixer [26]. Heikkinen et al. developed a sensor that can be used to detect forces acting upon dog limbs [27]. It was light enough in weight and had no side effect on the biomechanics of the limbs. Other applications for piezoelectric polymers and especially PVDF include orthopedic diagnostics, sports studies, respiration monitoring, loudspeakers, hydrophones, pressure distributions between vocal chords, etc.

In a broad sense, piezoelectric materials are widely used as active elements in stress gauges used to provide nanosecond, time-resolved stress measurements of rapid impulsive stress pulses produced by impact or explosion. Piezoelectric PVDF devices are the sensors of choice for a wide range of measurement applications due to their unique characteristics, i.e. rapid responses (ns), large stress range (kPa to GPa), large signal-to-noise ratio and high sensitivity (4 μCcm^{-2} for 10GPa). Besides, the PVDF sensors are very thin (even less than 25μm thick), self-powered and adaptable to complex contours.

Their direct stress-derivative or stress-rate signals of a few nanoseconds duration and higher operating stress limits provide capabilities not reachable by any other technique. Bauer reported early results on PVDF shock sensors [28] and, in 1995, described the first detonation profiles obtained with these devices [29]. Photopyroelectric spectroscopy (PPES) is a technique for photothermal measurements of properties of solids, and in special cases, liquids and gases. Extensive studies of PPES have been carried out at the University of Toronto, Institute of Molecular and Isotopic Technology of Romania, and at IBM Almaden Research Center in the USA. An early, very dramatic demonstration of the power of the technique was presented by Coufal [30,31]. He developed a method called thermal wave phase shifter for measuring both absorption and transmission spectra on the same sample. Another recent application has been the development of a Pd/PVDF thin film hydrogen sensor by Wang, Mandelis and Garcia [32]. A related approach was used by Wang and Mandelis to measure the thermal diffusivity of air [33].

Another application field of piezoelectric polymers such as PVDF can be cited as pyroelectric sensor array. Linear array sensors made from 70/30 (P(VDF-TrFE)) with 128 pixels were developed by Kohler et al. [34] and Neumann et al. [35]. The sensing elements consisted of a bottom electrode, the pyroelectric film and a top electrode, all mounted on a SiO_2/Si_3N_4 membrane created by back etching on a (100) Silicon wafer. Binnie et al. have developed a two-dimensional 16×16 pyroelectric sensor consisting of a 9 μm thick PVDF film sandwiched between a polymer surface electrode/absorber of polyethylene dioxythiophene polystryrene sulphonate (PEDT/PSS) and a rear metal reflector electrode [36]. Measurement Specialties Inc. of the U.S.A. tried generating power using PVDF on a credit card [37]. A piece of metallized 28 μm PVDF was cut to

53×80 mm dimensions and bonded to a simple 0.8 mm credit card using double-coated adhesive tape. It was concluded that reasonable energy levels are practical from a credit-card size piece of piezo film, but are limited by the means and/or rate of application of force to the substrate.

PVDF has found its way into aerospace applications as well. On Feb.7th 1999, NASA launched a spacecraft named Stardust that made a close encounter with the comet 81P/Wild 2 on Jan.2nd 2004. Included among the spacecraft instruments was the Dust Flux Monitor Instrument (DFMI) [38,39]. This device contained two PVDF sensors and provided real-time data on variations in the particle flux and mass distribution in the coma of the comet as well as measurements of dust in interplanetary space. This structure on such a short physical scale in the coma was unexpected and offered insights into the physical mechanisms at work in the coma. Health monitoring and non-destructive evaluation of structures and components such as finished composite structures are two other examples of application of PVDF in aerospace. Removable and reusable sensors are essential in applications such as health monitoring or the nondestructive evaluation of newly produced or finished composite structures. In such tests, a major requirement is that the tested structures are not altered during either bonding or removal of the sensor. Luo and Hanagud developed a simple PVDF sensor which incorporated all the aforementioned features [40,41]. This sensor demonstrated its capabilities through selected applications where it was ideally suited, namely, for detection of defects such as impact damage, saw cuts, and delaminations in elastic structures. These defects change the local curvature in beams, plates, or shell structures, and PVDF sensors are ideally suited to detect these changes in curvatures.

Nowadays there are growing interests in computer-human interaction systems that allow users to interact or to operate virtual 3D objects. In these devices, it is important to develop shape recognition devices for producing or manipulating virtual 3D objects. This has fueled some researchers such as Kato et al. to develop shape recognition devices using PVDF thin films [42].

1.2. Review of tactile sensors

During the past decade, various types of tactile sensors have been tested in different robotic-related applications [43-45]. Two important factors influence and motivate designing tactile sensors. The first one is the type of application and the second is the type of object to be contacted [46-48]. In general, tactile sensors can be divided into the following categories: capacitive, magnetic, optical, piezoelectric, piezoresistive (strain gauges), and silicon-based (micro-electromechanical). Furthermore, smart sensors are a new and special type of silicon-based tactile sensors, which have been developed to integrate signal processing with the sensors themselves [49]. Tactile sensors have various applications in improving the performance of different types of robots [50-52]. One example of these applications is the construction of artificial sensing fingers for robots which can probe and explore the environment [53]. These kinds of sensors have also been incorporated into industrial robots and grippers. Another application is in the area of autonomous mobile robots [54]. These machines have been evolving very rapidly and the requirement for absolute safety is the principal restrainer. Research has been done on automatic guidance of agricultural tractors as well as of industrial, mining and drilling

vehicles [50]. Semiautomatic operation with human supervision is essential in applications where autonomous operation is considered risky, such as handling containers and tele-operated forest harvesting [50,54].

One of the most exciting and relatively new application areas for tactile sensor is in the robotic surgery [55-58]. Nowadays, modern surgical procedures are far more intricate than those of the past and the surgeon's knowledge and his/her skilled, steady hand may not guarantee the success of an operation [59]. Robotic surgery can bring numerous benefits such as reducing the stress on the surgeons, decreasing the duration of surgery, and reducing the time required for a patient to recover from an operation [58,60-61].

1.3. Applications of PVDF in tactile sensing

PVDF has been used as a tactile sensor in medical applications whereby hardness and softness via palpation were investigated [62-63]. Dargahi et al. discussed design, fabrication, and theoretical analysis of a micro-machined piezoelectric tactile sensor for an endoscopic grasper [64]. The designed sensor exhibited high signal-to-noise ratio, high dynamic range, high force sensitivity, and good linearity. Dargahi et al. also designed and fabricated an endoscopic and robotic micro-machined sensor using a PVDF film. The development of the prototype of an endoscopic tooth-like piezoelectric tactile sensor has been discussed by Dargahi [12]. The main purpose of this design was measuring both force/position and surface profiles of biological tissues. Singh et al. investigated the finite element analysis and the experimental studies of this proposed sensor [57]. A preliminary micro-machined version of the same sensor was successfully

built and reported by Rao et al. [45]. Dargahi used various methods for separating pyroelectric and piezoelectric effects of PVDF-based tactile sensors [65,66]. By using only a single PVDF layer of film, the designed device showed an alternative transient approach to distinguish between piezoelectric and pyroelectric signals and therefore reduced the complexity of the sensor. As for the layout and sensing technique of a sensor, the bulk of efforts so far has been focused on designing and fabricating sensors with a large number of discrete sensing elements arranged in a matrix form [67,68]. These researches were motivated by two needs: measuring the magnitude of the applied force and identifying its position during the manipulation of objects. The most considerable setback with these designs was reported as *crosstalk* [69]. When a force is applied to a sensing element of a matrix tactile sensor, undesirable responses from the nearest neighbouring sensing elements often occur and lead into errors in measurement. This is the meaning of crosstalk. Dario and Buttazzo reported crosstalk problems in cases where the PVDF film was used as the basis for the design of a matrix of high spatial resolution tactile sensor [63]. Another feature of a matrix array of PVDF sensing elements is that it requires one coaxial cable per sensing element. The micro-miniature coaxial cables, of outer diameter between 0.6 and 2 mm, form a bundle that turns out to be the Achilles' heel of such sensors due to its size and poor flexibility. Besides, it is evident that the more the number of sensing elements becomes, the higher the number of connection points gets. Consequently, this leads to sensor fragility and causes the design to get bulky and this is indeed disadvantageous, especially in medical applications. In this regard, a research was carried out and published on the testing of a piezoelectric membrane tactile sensor with only three sensing elements [70,71].

1.4. Objective and scope of this research

As stated above, a piezoelectric membrane tactile sensor with only three sensing elements was fabricated and tested by Dargahi [70,71]. The sensor showed good results in detecting the magnitude and position of an applied force within a certain range of force magnitude. The sensor also showed sensitivity to the orientation of objects with sharp corners. However, this sensor was basically tailored for identifying point (or concentrated) loads. After all, in practical applications forces are rarely applied as concentrated or point loads. For instance, when an object touches the sensor area, the applied force is actually distributed over the contact area. This raised the questions which motivated the following research: Is the three sensing element layout prone to inaccuracy for detecting distributed forces? If the force is applied through, for example, a rectangular or triangular probe, how does the sensor respond? Is it still feasible to detect the magnitude of the applied force and to locate the centroid of the contacting object? All of these questions motivated the idea of adding another sensing element and rerunning the model in order to investigate its strong and weak points. This research focuses on a membrane-type PVDF-based tactile sensor with four sensing elements. This sensor enjoys freedom from some of the essential setbacks associated with their matrix type counterparts. While it still incorporates PVDF, it is easier to operate for its simplicity. However, it has its own limitations, which restrict its applications. No particular immediate application has been envisioned for this sensor so far. In fact, this report is mainly a proof of concept. In the following chapters, the steps taken toward completion of this work will be described. First, the theoretical works together with their results and related discussions will be presented. Then the fabrication of the sensor and its

experimental results and discussions will be presented. Finally, some concluding remarks and suggestions for future works will follow. The results are substantiated by numerous figures, plots, and tables wherever required.

Chapter 2 – Design and Finite Element Analysis of the sensor

The design of the sensor is shown below in Figure 2.1.

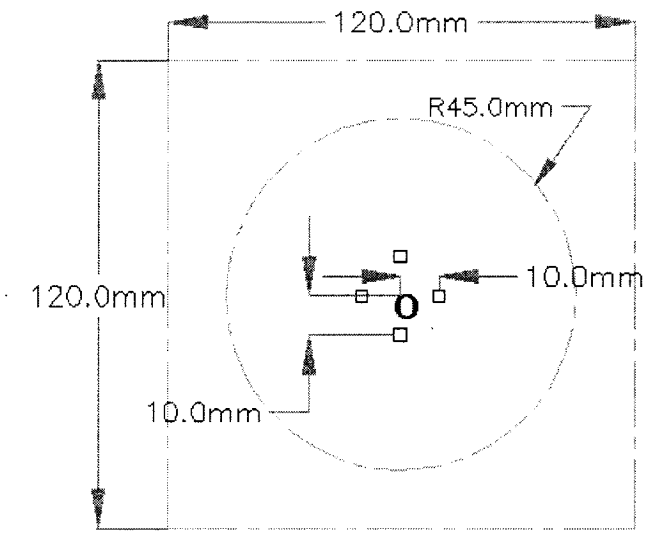

Figure 2.1 -- Design of the sensor

The sensor is comprised of a PVDF film, two square-shaped plexiglass plates and four aluminum square-shaped sensing elements. The plexiglass plates have a side of 120 mm and an inner circle with a radius of 45 mm. The central circle is the area of the PVDF film used for sensing. In other words, the PVDF film is exposed to external forces only within this circle. The thickness of the PVDF film is 25 μm. The material properties of the PVDF film are listed below in Table 2.1. These properties are based on the data from the GoodFellow Company of USA.

Table 2.1 -- Material properties of biaxial PVDF film

Young's modulus along drawn and transverse directions (GPa)	2
Poisson's ratio	0.34
Density (kg/m^3)	1760
Tensile strength in drawn and transverse directions (MPa)	180
Piezoelectric coefficient in drawn and transverse directions d_{31},d_{32} (pC/N)	8
Coefficient of thermal expansion ($x10^{-6}$ K^{-1})	110

Manufacturers of the PVDF films report the mechanical and electromechanical properties of PVDF films along three mutually perpendicular directions. These directions are shown below in Figure 2.2.

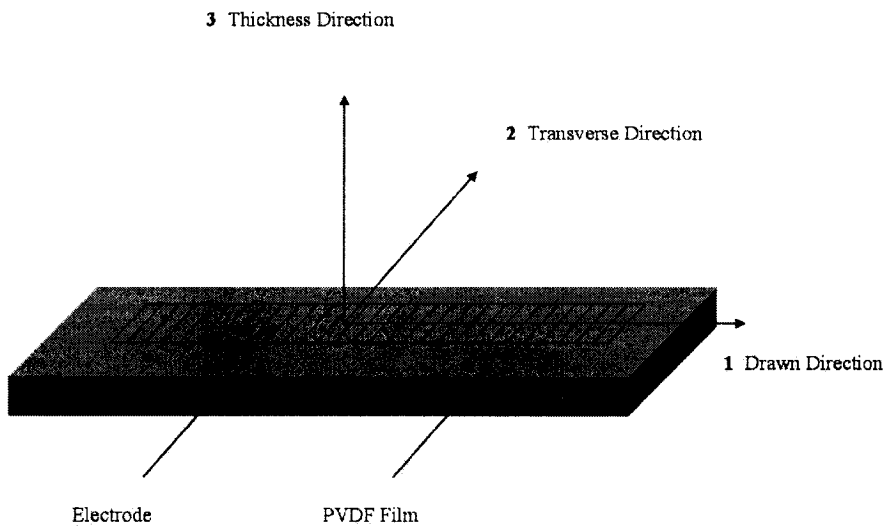

Figure 2.2 --The main three directions of a PVDF film

As shown in the above figure, the main three directions are mutually perpendicular. For biaxial PVDF films, such as the one used in this study, the mechanical and electromechanical properties along drawn and transverse directions are identical. The

sensor design also includes four sensing elements made of Aluminum. Each of them is a 3 mm × 3 mm square. The center of each sensing element is located 10 mm away from the center of the circular area, which is denoted by the letter O. Considering Figure 2.1, for theoretical analysis of the sensor, the PVDF film is considered as a circle of 45 mm radius which is clamped around its entire perimeter.

For theoretical analysis of the sensor, several challenges were faced. First of all, there is no exact or closed-form solution for the problem at hand. Closed-form solutions for the static or harmonic loading of a membrane can be found in some textbooks [72,73] or papers but with very special conditions; the force is applied either at the center of the membrane as a concentrated one or it is uniformly distributed across the entire surface of the membrane. Research on the mechanical behaviour and deflections of axisymmetrically loaded membranes has been immense, and numerous papers have been published on this issue. The literature covers both small and large deflection of membranes of different shapes, especially rectangular and circular ones. However, little effort has been made towards asymmetric loading of such membranes. In this research, as will be shown later, the loading is mostly non-symmetric. Furthermore, the problem is considered as a nonlinear, large-deflection-type which makes it more cumbersome. A few papers have been published on the behaviour of membranes in their most general case; membranes with an arbitrary shape, with arbitrary boundary and initial conditions and subject to any type of loads [74-78]. Although they have developed and presented equations for calculating the out-of-plane deflections at any point and any time, this does not satisfy the requirements for this project. The developed equations are very intricate

and appear impractical and inefficient for the numerical calculations. Even if they can be used and solved by the related mathematical softwares, the big challenge remains in effect: the out-of-plane deflections should be converted to strains and/or stresses and, later, converted to electrical charges. However, this is a too complex task to perform. An alternative approach for studying the most general loading cases of membranes is "The Analog Equation" method, which relies on the Boundary Element Method (BEM). With the help of this technique, it is possible to find out-of-plane deflections, strains, and stresses within any point of a membrane, with any type of shape, under any type of load and at any time [79-81]. Unfortunately, however, using this approach is neither simple nor straightforward. An excellent and in-depth knowledge of BEM technique is a prerequisite for utilizing the analog equation method. All of these resulted in adopting the Finite Element Method (FEM) as the best theoretical tool for analyzing the problem.

2.1. Finite Element Analysis (FEA)

For this purpose, ANSYS software (version 9.0) was extensively used. Since ANSYS is capable of running multidisciplinary simulations like piezoelectric problems, at first an attempt was made to run a piezoelectric analysis. This analysis enables the user to input load or deflection and directly obtain the generated output charges (or voltages) developed on the surfaces of electrodes. There are a number of elements available in ANSYS which are ideally suited for piezoelectric analysis of volumes such as SOLID 5, SOILD 98, SOLID 226, and, SOLID 227. Unfortunately, however, regardless as to the type of piezoelectric element used, all of the meshing attempts failed due to the extremely

large aspect ratio of the circular membrane ($\frac{\text{radius}}{\text{thickness}} \equiv \frac{45\,\text{mm}}{25\,\mu\text{m}} \equiv 1800$). Since the ANSYS version used in this research was designed for use by students only, it had particular limitations in terms of the maximum number of elements (16,000) and/or nodes (32,000) it can support. This was the most significant obstacle encountered in meshing. To fix this issue, the dimensions of the model were modified so that its aspect ratio drops. For example, the radius was reduced to 10 mm and the thickness was increased to 110 microns yet new problems still arose: either the produced meshes were too coarse or a large number of shape violations were reported by ANSYS, sometimes even up to a quarter of the total number of elements. A summary of different runs, along with their related parameters, is presented in Appendix 2. An alternative solution was considered in which it was proposed to run a structural analysis, extract the resultant stresses, and finally convert them to charges using piezoelectric formulae.

2.1.1. Element type

The most suitable element for a structural analysis of shells and membranes is SHELL 63 element. This element has both bending and membrane capabilities in which both in-plane and normal loads are permitted. The element has six degrees of freedom at each of its nodes: three translations and three rotations. Stress stiffening and large deflection capabilities are included. A consistent tangent stiffness matrix option is available for use in large deflection (finite rotation) analyses. Not to mention, SHELL 41 element can also be used effectively for satisfying the needs of this research. It is a three-dimensional element having membrane (in-plane) stiffness but no bending (out-of-plane) stiffness. It

is actually intended for shell structures where bending of the elements is of secondary importance. The element has freedom in the x, y, and z nodal directions. Although SHELL 41 element seems more appropriate for the proposed simulations, and easier to work with, it is worth mentioning that SHELL 63 element has the option of being a "membrane only" element.

2.1.2. Modeling

After creation of the PDVF film and its sensing elements, the shape of the probe, either triangular or rectangular, was added. Afterwards, all of the created geometries were first overlapped and then glued together using the AOVLAP and the AGLUE commands. Material properties of the PVDF film were input according to the Table 2.1. It should be mentioned that the value for the last property in the Table 2.1, the coefficient of thermal expansion, is the average of its lower and upper limits published by the GoodFellow Corporation (which are respectively $80\times10^{-6}\,K^{-1}$ and $140\times10^{-6}\,K^{-1}$). As will be explained later, it is used for introducing a uniform pretension to the area of the membrane.

2.1.3. Meshing

After creation of all the areas, a meshing process was performed. To achieve this goal, an element size of 0.75 mm was selected for meshing the probe and four square sensing elements. For the remainder of the membrane area, a size of 1 mm was chosen. Because

of the nonlinearity of the static problem, and in accordance with ANSYS recommendations, all of the areas were meshed using triangular elements. For a planar element such as SHELL 63, it is often possible to choose two geometries: quadrilateral and triangular. At first, the quadrilateral element was selected but two problems occurred. The first one was that using quadrilateral elements resulted in non-uniform meshing as shown in Figure 2.3.

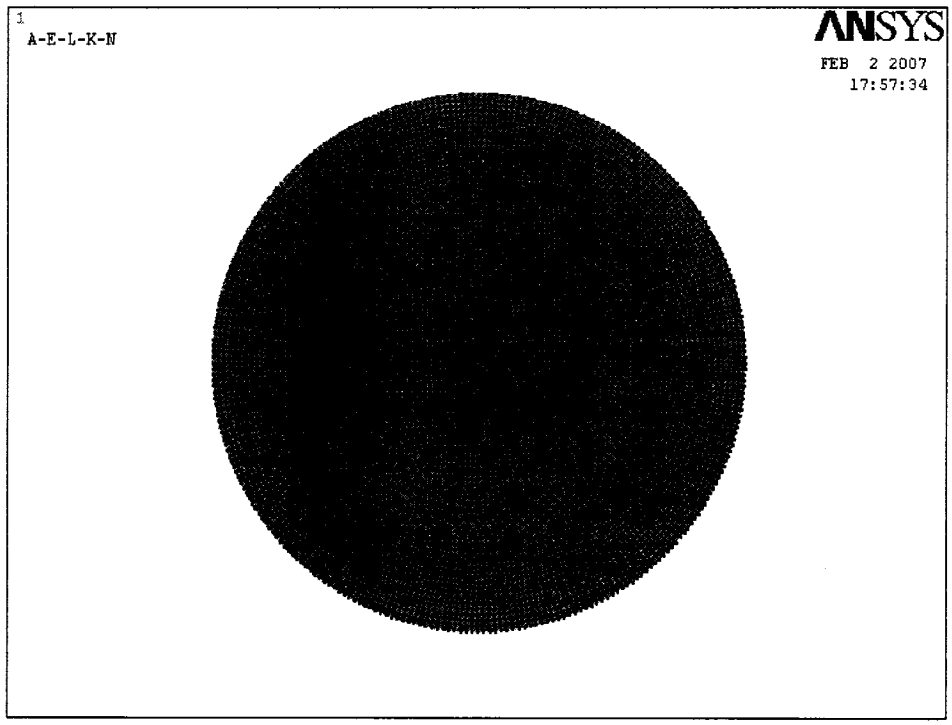

Figure 2.3 -- Meshing with quadrilateral elements

The second and even more important problem is that ANSYS is only capable of solving such a problem when the element has a triangular shape. When choosing a

quadrilateral element, as shown in Figure 2.4, the following message appeared which

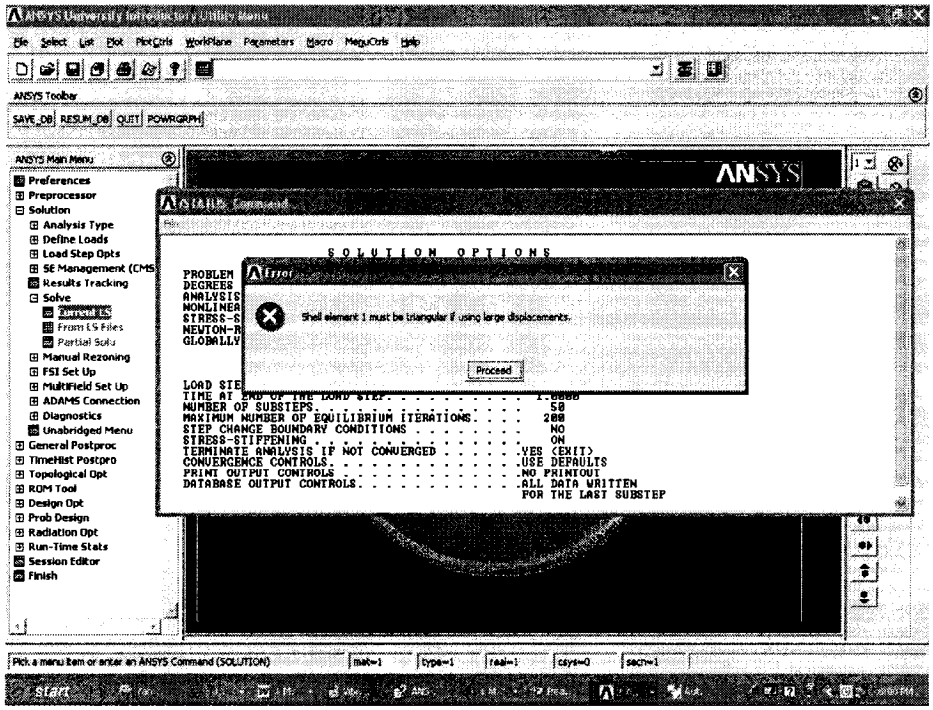

Figure 2.4 -- ANSYS message

stated: "Shell element must be triangular if using large displacements.". Following that, the solver proceeded no further.

Because of these obstacles, a triangular element was selected. The associated meshing was considerably more uniform this time as depicted below in Figure 2.5.

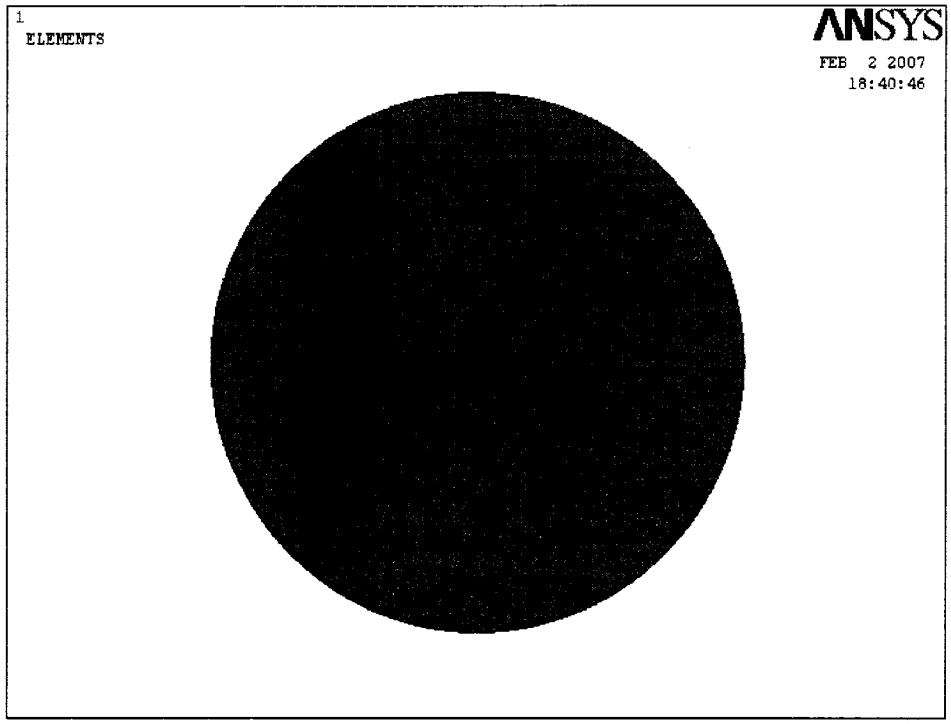

Figure 2.5 -- Meshing with triangular elements

Although the number of generated elements varied from one model to another, depending upon the shape and location of the probe, the number typically fell in the range of 13,000 to 14,000. This might seem too big but it ensures that the produced mesh is sufficiently uniform and captures the entire geometry well enough.

Before applying the loads, it is very important to issue the NLGEOM and SSTIF commands. Both of these should be set to the ON mode so that the model could be solved accurately.

2.1.4. Structural nonlinearity

Geometrically speaking, the problem at hand can be categorized as a nonlinear type. In a broader sense, structural nonlinearity or nonlinear structural behavior arises from a number of causes including changing status, material nonlinearities and geometric nonlinearities.

In the case of changing status, many common structural features exhibit nonlinear behaviour that is *status-dependent.* For example, a tension-only cable is either slack or taut; a roller support is either in contact or not in contact. Status changes might be directly related to load (as in the case of the cable), or they might be determined by some external cause. Situations in which *contact* occurs are common to many different nonlinear applications. Contact problem forms a distinctive and important subset to the category of changing-status nonlinearities. However, the problem in this research does not fall into the above category.

For material nonlinearity, this is not applicable either because PVDF exhibits good linearity. The relationship between the applied force and the output charge is linear for stresses up to 40 MPa [82].

It is geometric nonlinearity, however, that is the main reason for nonlinear behavior of the model at hand. Generally speaking, if a structure experiences large deformations, its changing geometric configuration can make it respond nonlinearly. An example is the fishing rod. Geometric nonlinearity is characterized by "large" displacements and/or

rotations. For the PVDF model of this project, geometric nonlinearity can be explained on the grounds of dimensional properties of the model and also the magnitude of the applied load. Although a load of 1 N might seem too small to cause large deflections and any sort of nonlinearity, it must be realized that this load is applied only to the area of the probe – which is very small. If this is applied by a rectangular probe of 14 mm by 7 mm dimensions, this gives a lateral pressure of 10204.082 $\frac{N}{m^2}$. For an equilateral triangular probe of 7 mm side, this pressure rises to 47130.684 $\frac{N}{m^2}$. These are huge pressures exerted over very small areas and that, coupled with the dimensional properties of the PVDF film, leads to a geometrically nonlinear system.

By issuing the NLGEOM command and setting it to the ON mode, ANSYS includes large-deflection effects in a static analysis which are categorized as being either large deflection (or large rotation) or large strain, depending on the element type. For the PVDF film and SHELL 63 element, due to the extremely small thickness of the membrane it cannot be taken as being a large strain but rather as one of large-deflection.

Issuing SSTIF command and setting its key to the ON mode, activates and includes stress stiffness effects in a nonlinear analysis. Stress stiffening (also called in other literature as geometric stiffening, incremental stiffening, initial stress stiffening or differential stiffening in other literature), is the stiffening (or sometimes weakening) of a structure due to its stress state. This stiffening effect normally needs to be considered for thin structures with bending stiffness very small compared to axial stiffness, such as cables,

thin beams, shells and membranes and couples the in-plane and transverse displacements. This effect also augments the regular nonlinear stiffness matrix produced by large strain or large deflection effects (which are produced by issuing the NLGEOM, ON command). The effect of stress stiffening is accounted for by generating, and then using, an additional stiffness matrix, also called the "stress stiffness matrix". The stress stiffness matrix is added to the regular stiffness matrix in order to give the total stiffness.

The stress stiffness matrix is computed based on the stress state of the previous equilibrium iteration. Thus, to generate a valid stress-stiffened problem, at least two iterations are normally required of which the first is used to determine the stress state that will be used to generate the stress stiffness matrix of the second iteration. If this additional stiffness affects the stresses, further iterations are required to reach a solution.

2.1.5. Loads and boundary conditions

Loads are applied after issuing NLGEOM and SSTIF commands. For the PVDF film, as stated earlier, the film is modeled as a circular membrane which is clamped all around its perimeter.

Using the "solid modeling" feature of ANSYS, boundary conditions were applied as constraining the outer perimeter of the circle. In "solid modeling", instead of dealing with nodes and elements generated during the meshing process, the model is treated as a solid or continuum. Hence, as for fixing the outermost nodes on the PVDF film, in lieu of setting the translational degrees of freedom to zero on each of the nodes, the whole

perimeter is fixed. The same approach can be utilized for applying the external lateral pressure. Instead of counting the number of nodes generated on the probe area and distributing the lateral pressure among them uniformly, the pressure is applied to the whole probe area as one entity.

Since the problem is a static loading, no temporal initial condition needs to be defined. However, in order to introduce the pretension to the membrane and make it taut, first a coefficient of thermal expansion is defined at 25 °C. Then a uniform temperature of 24 °C is applied across the entire PVDF area. This, coupled with the fact that the circular PVDF film is clamped all around its perimeter, leads to a uniform pretension in the membrane and makes it taut.

Two other important parameters to take care of are respectively: 1) the *"number of substeps"* and 2) the *"maximum number of equilibrium iterations"*. A proper setting of these two variables plays a crucial role in the convergence of the solution as well as the accuracy of the results. For the model at hand, the *"number of substeps"* was set to 50 using the NSUBST command. The *"maximum number of equilibrium iterations"* was set to 200 using the NEQIT command. These two values were determined by trial and error.

2.1.6. Postprocessing

Since the type of analysis was selected as "structural", evidently the generated results are stresses and/or deflections. By writing a code, it was possible to obtain directly the output electrical charges that surfaced on the sensing elements in ANSYS. First, for the meshing process, the element edge size for each electrode was 0.75 mm as depicted in the Figure 2.6.

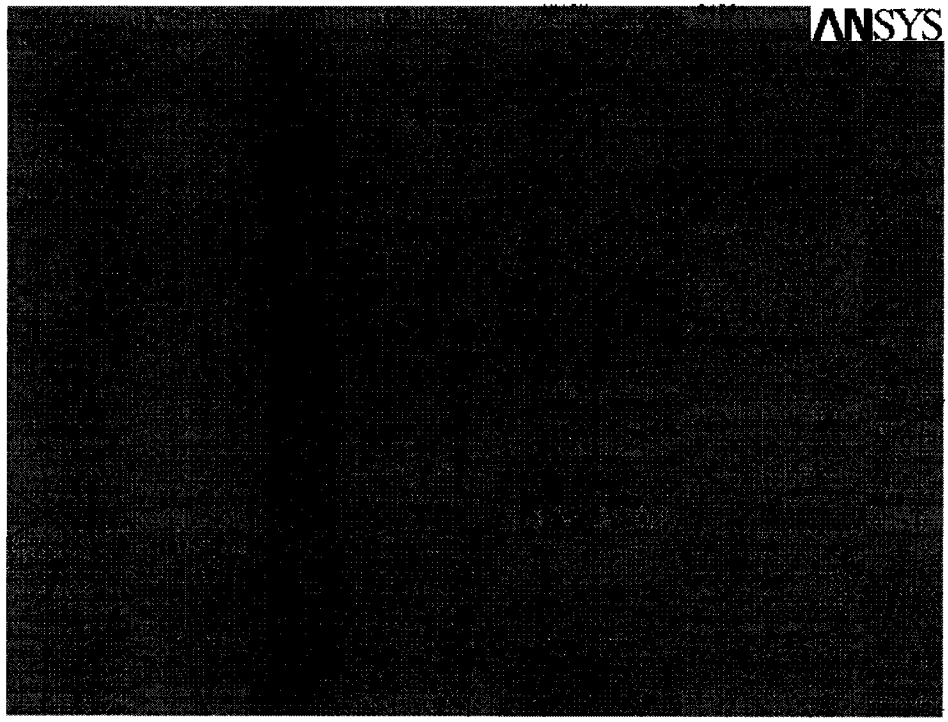

Figure 2.6 -- A meshed electrode

The edges of electrode are the lines connecting nodes 6&10, nodes 6&2, nodes 2&1 and nodes 1&10. As illustrated, with an element size of 0.75 mm, 16 nodes are generated on the edges of a square-shaped electrode. The formula for computing the electrical charge is:

$$Q = (d_{31}\sigma_x + d_{32}\sigma_y) \times A$$

whereby A is the area of the electrode surface. Since the stresses along both directions x- and y- vary within an electrode area from point to point (or from node to node in terms of finite element analysis), an important question is raised: How is it possible to take the average of each of these two stress components across an electrode surface? To answer this question, the calculation of the average value of σ_x along the surface of electrode A is considered first. An improved method for this calculation was developed which was

based on the PATH feature in ANSYS. Using the PATH and its relevant commands, it is possible to define a path, establish and map a certain parameter onto it, and eventually perform some mathematical operations on the path. The first impression is that performing integration across the surface of an electrode yields more accurate results for both of the stress components. Although this is true, it is unfortunately based on the contents of ANSYS help in which surfaces can be defined only in models containing three-dimensional solid elements. Shells, beams, and two-dimensional element types are not supported. Since the selected element type is SHELL 63, and due to the inherent problems when choosing three-dimensional solid elements, surface operation was discarded and the effort was switched to doing a line integration. This is not necessarily inaccurate because in piezoelectric studies for computing the charge or voltage developed on a piezoelectric part, as shown in Figure 2.2, stress components along the outer-most edges come into picture.

Hence, if the average stress components along the outermost edges are found and plugged into the piezoelectric formulae, the corresponding obtained charge is precise. In accordance with these discussions, considering once again σ_x for electrode A as an example, first line integrations of σ_x along its right and left edges were done. Then, the result for each edge was divided by its length and the average of two sides was considered as the final value for σ_x . This is better illustrated in the following equation:

$$\sigma_x = \frac{(\sigma_x)_{left} + (\sigma_x)_{right}}{2} = \frac{\frac{\int_{left} \sigma_x ds}{s} + \frac{\int_{right} \sigma_x ds}{s}}{2} = \frac{\int_{left} \sigma_x ds + \int_{right} \sigma_x ds}{2s}$$

In the above equation **s** is the total length of the path (which is the edge of the electrode) and **ds** is the incremental length of each edge. So the value for **s** is 3 mm for all the four edges of all the four electrodes A, B, C, and D. The PATH command comes into the picture at this time. Using the coordinates of nodes created on the right and left edges of electrode A, each of the edges is defined as a path. Another important parameter to be defined while using the PATH command is the number of divisions between adjacent points which is 20 by default and selected here. By writing a computer program that is capable of going through all the arithmetic operations, it was possible to see the charges on all four electrodes in a table which appeared after the processing was complete. Therefore, there was no need for further graphical operations like selecting the middle nodes on each edge, finding its developed stress, and converting it into charge.

An important application of this sensor, and indeed its main purpose, is to determine the magnitude and position of an applied force. Initially it was presumed that using three electrodes would give a precise and reliable indication as to where the force is located and its magnitude. But the question was raised as to whether or not this method is applicable only for concentrated loads only. When the shape of the object in contact with the PVDF membrane changes to a non-symmetric one, or even for a symmetric shape but with unequal sides and sharp points such as an equilateral triangle or a rectangle, the triangulation approach may not work well enough. In order to investigate and verify this, a large number of simulations were implemented with ANSYS. The following chapters report the results of those simulations, coupled with graphs, figures, results and final conclusions.

2.2. Summary

This chapter began with an explanation of the design and layout of the sensor. It was explained that, due to the dimensions of the membrane, the problem is classified as a large-deformation one. Geometrically speaking, the problem is nonlinear. Because of the complexities involved in closed-form solution of such problems, Finite Element Analysis was the only viable theoretical approach. This was done by ANSYS 9.0, student version. Because of the limitations of student version, it was not possible to use piezoelectric elements. Instead, a structural analysis was performed. By writing a code, combined with using the basic piezoelectric formula, it was possible to extract the stresses developed in the membrane, along the edges of the sensing elements, and convert them to output electrical charges.

Chapter 3 - Detecting the position and magnitude of an applied force

Both this chapter and the next are entirely devoted to the theoretical results obtained through ANSYS simulations. In the current chapter, simulations are focused on the application of the sensor for detecting the magnitude and position of an applied force. The adapted method for attaining the theoretical results via ANSYS simulations was detailed in the previous chapter. The next set of simulations to follow is for two shapes of probe touching the sensor area: triangle and rectangle.

3.1. Triangulation approach and mapping scheme

The identification of a point on a two-dimensional plane requires the value of its coordinates to be known. The position of a point on the plane can be found from knowledge of its distance from three reference points, the coordinates of which are known. This approach used for position detection is similar to the concept behind global positioning system (GPS). The need for the distances from three reference points can be easily seen by considering the case where the distances from only two reference points are known. These distances define a circle about each of the reference points, and their intersection gives the position of the unknown point. There are, however, two intersections so that these distances do not unambiguously define the position of the

unknown point. This is shown in Figure 3.1, where points a, b, and c represent three arbitrary points on a plane.

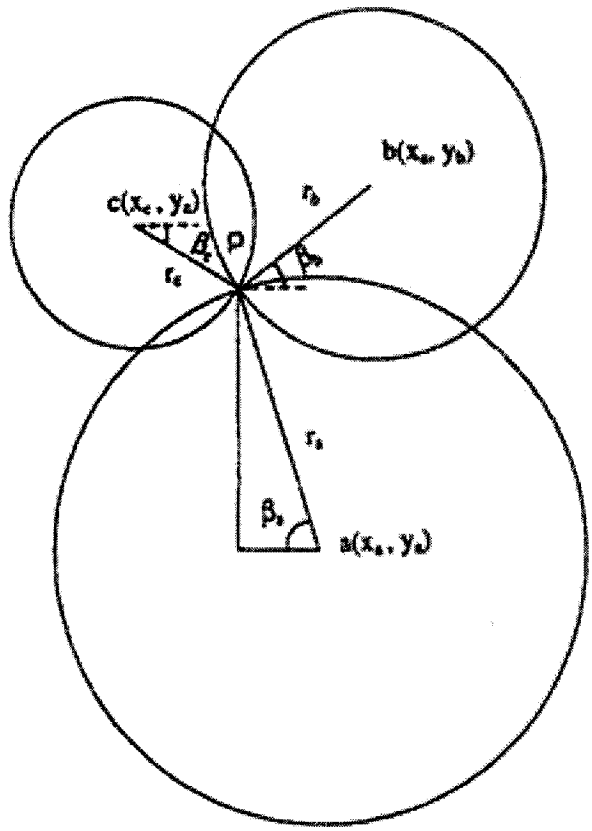

Figure 3.1 -- Schematic illustration of triangulation approach

This means the triangulation approach for position identification requires a minimum of three data. The equation used for position determination is the famous Pythagorean Theorem expressed as:

$$r_n^2 = (x_n - x_p)^2 + (y_n - y_p)^2 \qquad n = a, b, c$$

where x_n and y_n are known positions of the three sensing elements

r_n is the distance between applied force's position and sensing element

x_p and y_p represents the unknown positions of the applied force

If the radii are known for the three circles and the position of the sensing elements are known, it will be possible to determine the position of the applied force, since we will have three equations (with n = a, b, c) and only two unknowns (x_p, y_p). With only three sensing elements, obviously, it will be difficult to obtain the shape as in the matrix arranged sensing elements, but this is just to illustrate the fundamentals of the triangulation approach and its potential to simplify the sensor's structure. From the triangulation equation, one may ask how it is possible to know the distance between the position of applied force and center of the sensing element. Obviously, if the applied force changes position, so does the distance. Therefore, the key idea of this sensor design is using triangulation method to find these distances, which will be discussed in the following section.

The mapping scheme is shown in the next page in Figure 3.2. A similar scheme was adopted in some previous works [70,71]. First, one of the electrodes is selected. Then, a number of lines and circles are drawn with respect to the electrode center, as depicted in Figure 3.2.

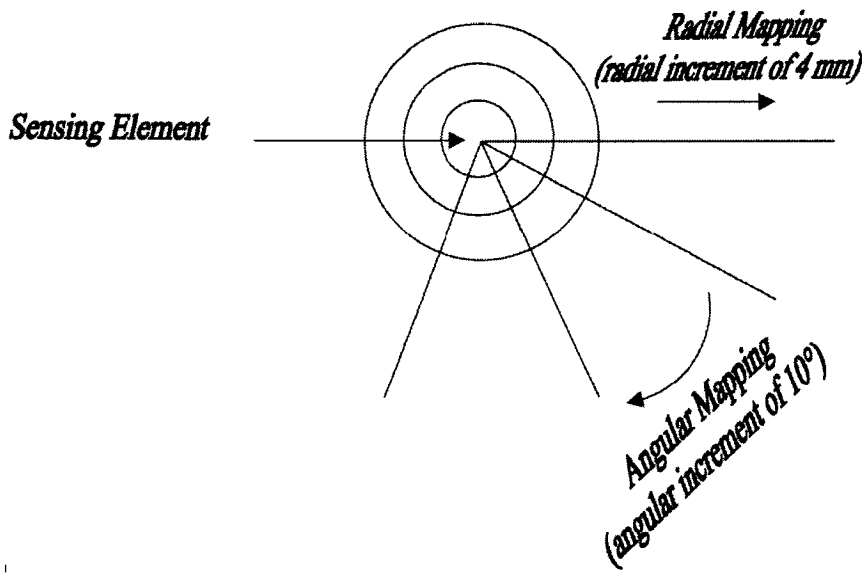

Figure 3.2 -- Schematic illustration of the chosen mapping scheme

The radial and angular increments are respectively 4 mm and 10°.

3.1.1. Calibration of the sensor with three sensing elements

The sensor is shown below in Figure 3.3.

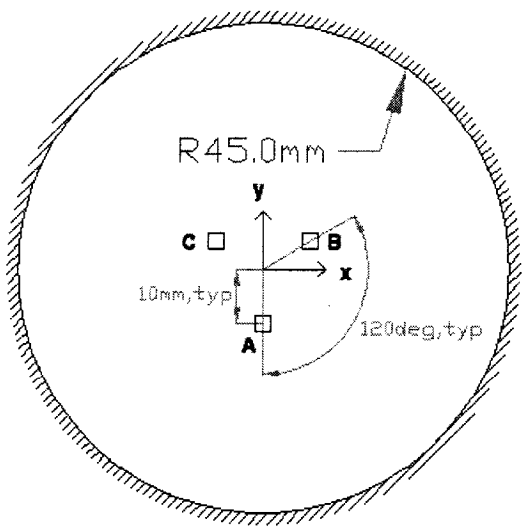

Figure 3.3 – Layout of the sensor with three sensing elements

The PVDF film is considered as a circle which is clamped all around its perimeter. The center of each of the three sensing elements, A, B, and C, is 10 mm away from the center of the membrane, or the origin of the coordinate system. If the centers of all three electrodes are connected to each other, an equilateral triangle will be created. Lines connecting the center of the membrane to the centers of electrodes B and C make angles of 60° and 120° with the x- axis (or the drawn direction of the biaxial PVDF film), respectively. The center of electrode A is located exactly on the y-axis (or the transverse direction of biaxial PVDF film). The following figure shows how the mapping scheme works for this arrangement.

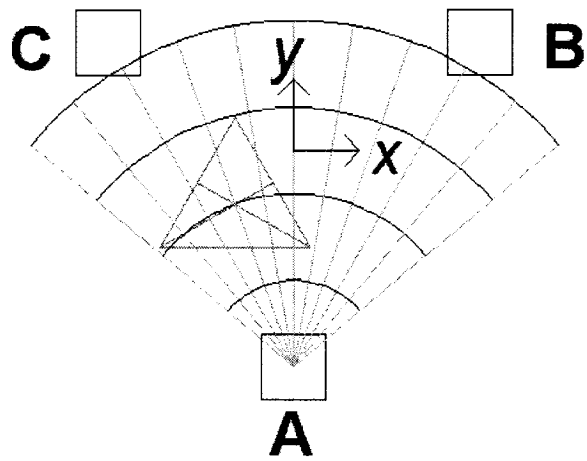

Figure 3.4 -- Mapping scheme for the three sensing element layout; electrode A as reference

The equilateral triangular probe, 7 mm in side, dislocates between intersections of lines and arcs. Here is how it works: for the first set of simulations the probe is moved along the right-most line from one intersection to another with radial increments of 4 mm. For each line, which is drawn at a certain angle with respect to the x- axis, the resulting output electrical charges on the electrode A are obtained. This is followed by plotting a number of curves for each angle as shown in Figure 3.5. In this figure, it is shown how

the output charge changes against distance while moving on lines drawn with different angles, from 35° to 90°, with respect to the drawn direction.

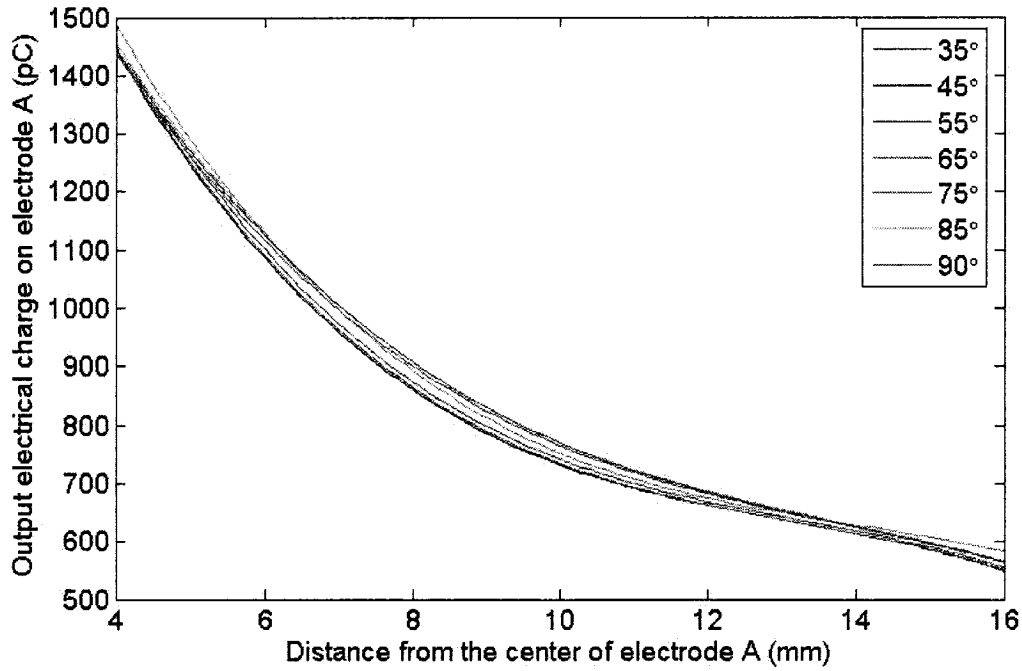

Figure 3.5 -- Charge versus distance variation for a triangular probe, biaxial film

Another mapping is carried out, with respect to the electrode B, which is shown in Figure 3.6.

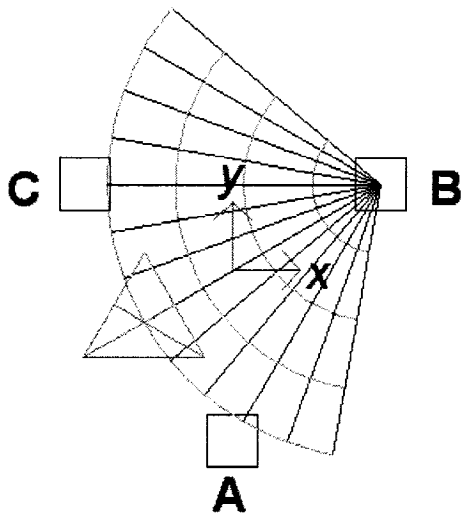

Figure 3.6 -- Mapping scheme; electrode B as reference

Using the same procedure leads to the following curves.

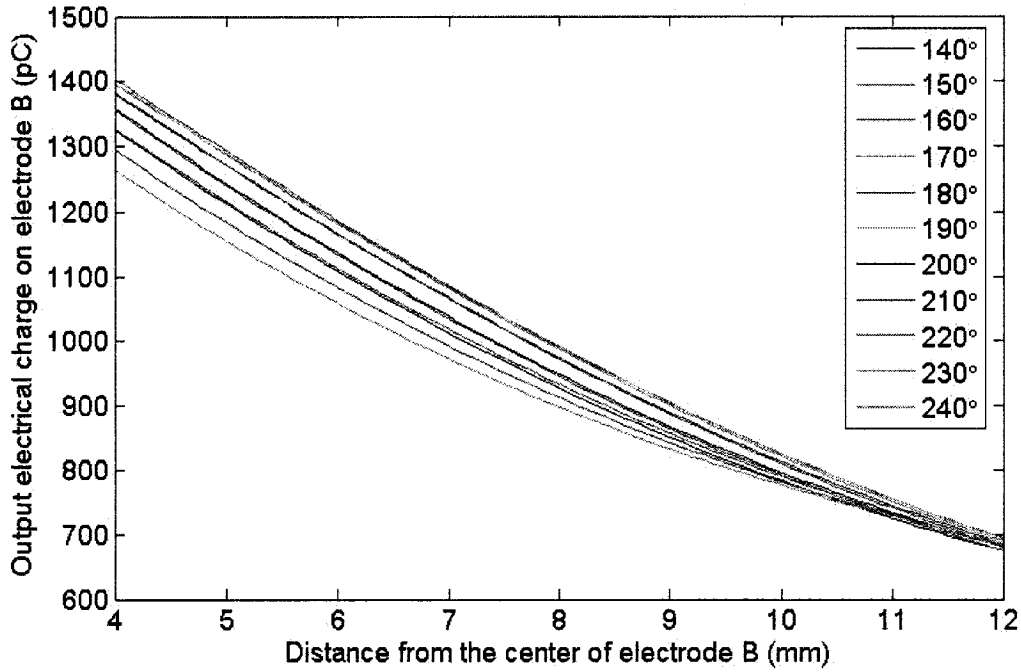

Figure 3.7 -- Charge versus distance variation for a rectangular probe, biaxial film

In the above figure, the lines along which the force moves, make angles with the drawn direction which vary in the range of 140° to 240°. Throughout the entire simulations, the load transferred through the probe was assumed as 1 N. For clarification on the figures 3.5 and 3.7, it is worth mentioning that the upper-most curves in both figures correspond to the smallest angles; i.e. 35° in Figure 3.5 and 140° in Figure 3.7. The lower-most curves represent the largest angles; i.e. 90° in Figure 3.5 and 240° in Figure 3.7.

The next step is utilizing the triangulation technique. As mentioned earlier, this is a method for determining the location of a point in a plane. The earlier description of triangulation approach was based on the distances of an arbitrary point within a plane from three reference points. Here, it is dealt with in a different way: if a force is applied onto the surface of a PVDF film via an arbitrary shape, stresses and consequently

electrical charges will be developed on the electrodes. For a given shape of probe coupled with its fixed dimensions and a known magnitude of applied force, it is possible to find out the loci of points which all share something in common: if a particular force is applied at each of these points via the pre-determined probe, a certain amount of charge will appear on the electrode. The connection of all those points leads into what is called an "isocharge contour". Therefore the procedure for detecting the location of a force is redefined as follows: given the output electrical charges on the three electrodes are, namely, X, Y, and Z, for each electrode the related isocharge contour is drawn. The intersection point of them yields the desired data.

Creation of the isocharge contours can be done by using the charge versus distance curves depicted in figures 3.5 and 3.7. As an example, it is assumed that the charge on electrode A is 650 pC. A horizontal line corresponding to 650 pC is drawn so that it crosses all the graphs. The intersection points are what we need to construct the isocharge contour. Assuming this was done in Fig.3.5, the following pairs of data could be extracted:

$35°, x_1$ $45°, x_2$ $55°, x_3$ $65°, x_4$ $75°, x_5$ $85°, x_6$ $90°, x_7$

Each of these points should be identified in a polar system, the origin of which is the center of the referred electrode. Eventually, they are connected to each other and form an isocharge contour. A polynomial was fit to each set of data in figures 3.5 and 3.7 and finding their coefficients. Then, the obtained equation was set equal to the desired output

charge, and its root was found. The answer is one point of an isocharge contour. Later, the points were joined in AutoCAD using the SPLINE function.

A few triangulations are presented hereafter.

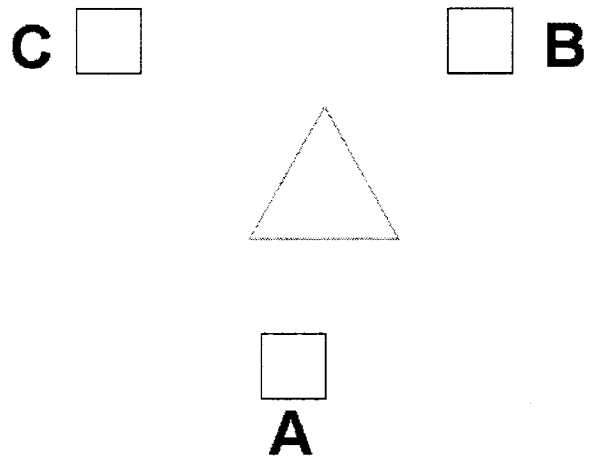

Figure 3.8 – First simulation with a triangular probe

In the first case, as shown in Figure 3.8, the probe was located at 8 mm and 85° with respect to the center of electrode A. These are the attained results in an ANSYS simulation:

Output charge on electrode A: 905.1037 pC

Output charge on electrode B: 731.3554 pC

Output charge on electrode C: 687.9185 pC

By going through the same procedure as described before the following sets of data are obtained:

For electrode A:

35°, 7.510 45°, 7.556 55°, 7.662 65°, 7.867 75°, 7.949 85°, 8.034

90°, 8.032

For electrode B:

140°, 9.931 150°, 10.011 160°, 10.188 170°, 10.382 180°, 10.596 190°, 10.651

200°, 10.629 210°, 10.559 220°, 10.460 230°, 10.356 240°, 10.301

For electrode C:

140°, 11.015 150°, 11.105 160°, 11.268 170°, 11.483 180°, 11.707 190°, 11.772

200°, 11.754 210°, 11.728 220°, 11.617 230°, 11.519 240°, 11.453

Since electrodes B and C are symmetrical with respect to the y- axis or transverse direction, it is possible to create the isocharge contour relative to electrode B and then use the MIRROR command of AutoCAD and to mirror it relative to transverse direction. In the Figure 3.9 all three isocharge contours are drawn.

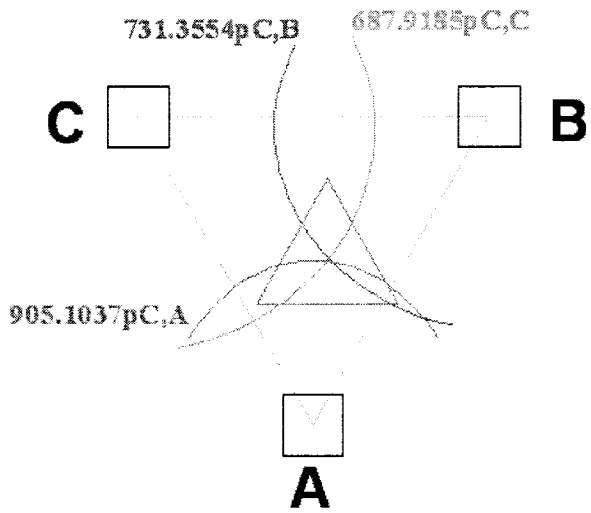

Figure 3.9 — Isocharge contours

Contrary to what is shown in the above figure, the three contours are not concurrent, i.e., they do not intersect in one single point. Hence it was decided to take the coordinates of all three intersecting points and compute their average as a unique yet imaginary intersection point. Since the intersection points are very close to each other, this assumption is logical and acceptable.

Using the DIST command of AutoCAD, the distance between the exact location of the center of the probe and the calculated average was found equal to only 0.122 mm, which is acceptable.

In the next simulation, as shown in Figure 3.10, the triangular probe is located at 8 mm and 135° with respect to the center of electrode A.

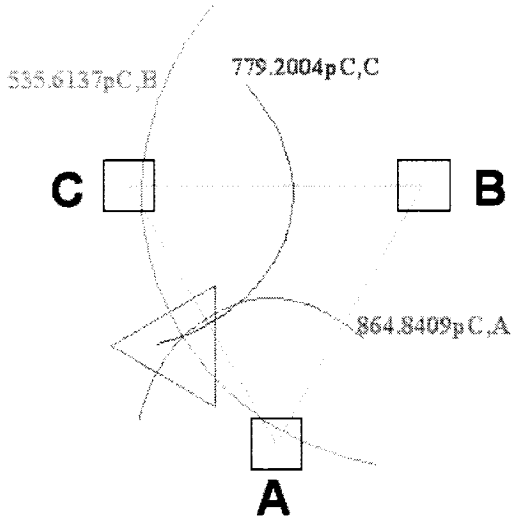

Figure 3.10 — Second simulation with a triangular probe and its isocharge contours

Simulation results are:

Output charge on electrode A: 864.8409 pC

Output charge on electrode B: 535.6137 pC

Output charge on electrode C: 779.2004 pC

This simulation is a bit different from the previous one in the sense that the probe is rotated. The first impression was that a three-electrode system may not work well for a non-circular probe or even if it works, it may give erroneous results when the probe is rotated in its place. The idea behind this simulation was to find out whether a three-electrode system is able to locate the position of the probe whether it is rotated or not. The positioning error was found to be 0.574 mm. Although it is larger than the previous ones, it is still acceptable and ignorable.

Before proceeding to the next simulations, two points should be cleared:

1) In some simulations, the probe had a small overlap with the electrode B. This may raise a concern whether the third piezoelectric coefficient, d_{33}, should be taken into consideration or not because the electrode area is directly touched and under pressure of a force along the 3- or thickness direction. The answer is negative. That is so because, although the electrode B undergoes a force along a direction perpendicular to its face, it is part of a very thin membrane (just 25 μm). As a result, there is no stress or strain in the 3- or thickness direction, which means no charge is produced because of d_{33} effect.
2) Another point to consider is the pyroelectric effect. When a foreign object or probe touches the electroded area of a PVDF film, a sudden change of temperature can occur. That leads into a secondary source of charge generation. At times, this effect can be noticeably large and even dominate other sources like stresses. Throughout simulations, it was assumed that, even if the probe comes into contact with an electrode area, no temperature alteration happens. This means, in effect, that the pyroelectric effect in the entire set of simulations has been ignored.

The results of the preceding simulations, as well as those of four others, are presented in the Table 3.1.

Table 3.1 — Summary of simulation results for a triangular probe

Position of the probe centroid	Positioning error for the three electrode sensor (mm)
8 mm, 85° (with respect to the center of lower-most electrode)	0.122
16 mm, 75° (with respect to the center of lower-most electrode)	0.368
8 mm, 135° (with respect to the center of lower-most electrode), probe rotated 90° CCW	0.574
12 mm, 105° (with respect to the center of lower-most electrode), probe inverted	0.146
Probe at the center, rotated 90° CW	0.03
12 mm, 65° (with respect to the center of lower-most electrode)	Not intersecting

As it is mentioned in the lowest row of Table 3.1, when the probe was located at 12 mm and 65° with respect to the center of electrode A, no result was obtained from the simulation. Because of this failure, the four sensing element layout is tried in order to investigate its possible advantages over the three-element scheme.

3.1.2. Calibration of the sensor with four sensing elements

As illustrated in the Figure 3.11, the triangular probe was located at 12 mm and angle of 65° with respect to the center of electrode D.

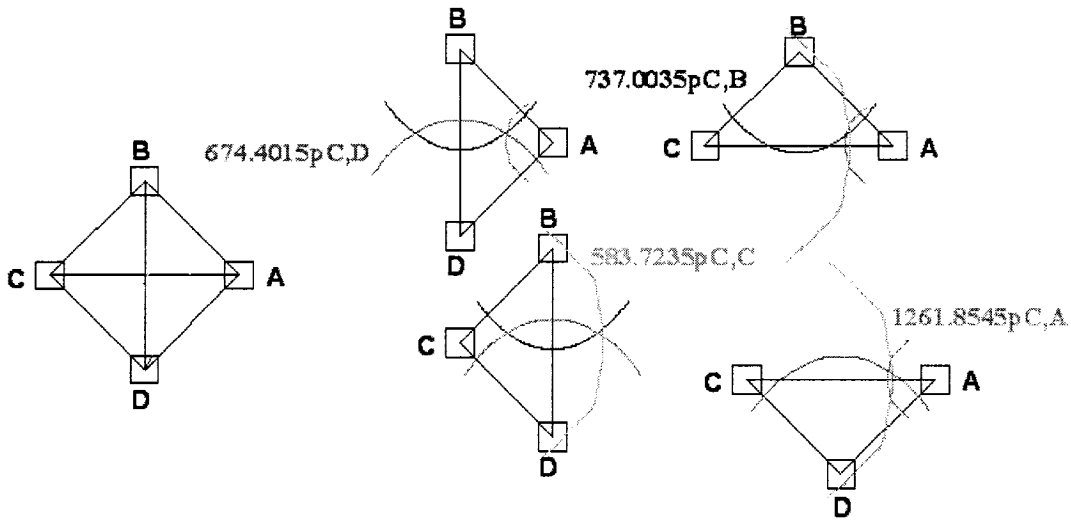

Figure 3.11 — Simulation with a triangular probe for the four sensing element layout

These are the corresponding obtained charges.

For electrode A: 1261.8545 pC

For electrode B: 737.0035 pC

For electrode C: 583.7235 pC

For electrode D: 674.4015 pC

Redoing the triangulation leads into:

--In triangle ABC: x= 5.2977 mm y= 1.6012 mm

--In triangle ACD: x= 5.2649 mm y= 1.2206 mm

--In triangle ABD: x= 5.0040 mm y= 1.0214 mm

--In triangle BCD: x= 5.2358 mm y= 1.0103 mm

Averages of all coordinates are:

x= 5.2006 mm y= 1.2134 mm

This time, the target point is located at x = 5.0714 mm and y = 0.8757 mm. The corresponding positioning error is 0.362 mm.

A close-up of the central area is shown below in Figure 3.12 in order to illustrate how far the exact position of the force is from its calculated position, or the sensor output.

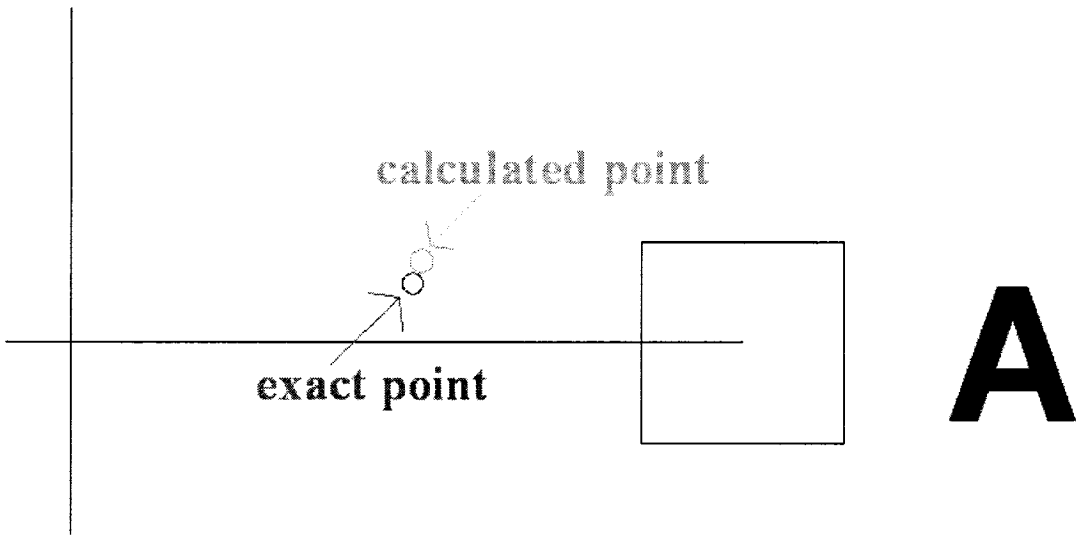

Figure 3.12 -- A close-up comparing exact and calculated positions of the probe

For all preceding cases the four sensing element layout led to valid results. Therefore, the associated calculations and figures are not presented hereafter.

3.2. Rectangular probe

The same mapping scheme used for the triangular probe was utilized here for a rectangular probe of 14 mm by 7 mm size.

3.2.1. Calibration of the sensor with three sensing elements

For the first simulation, as shown in Figure 3.13, the probe was located at 8 mm and 85° with respect to the center of electrode A.

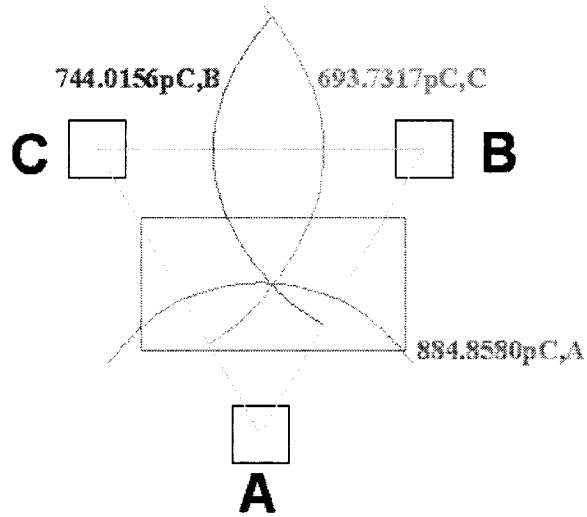

Figure 3.13 — First simulation with a rectangular probe

Simulation results are:

Output charge on electrode A: 884.8580 pC

Output charge on electrode B: 744.0156 pC

Output charge on electrode C: 693.7317 pC

The positioning error was found out to be 0.09 mm.

In the second simulation, as shown in Figure 3.14, the probe was located at 12 mm and 105° with respect to the center of electrode A. Moreover, the probe was rotated 90°.

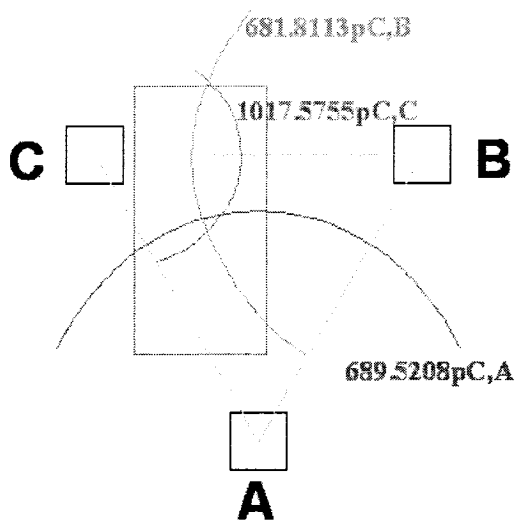

Figure 3.14 — Second simulation with a rectangular probe

Simulation results are:

Output charge on electrode A: 689.5208 pC

Output charge on electrode B: 681.8113 pC

Output charge on electrode C: 1017.5755 pC

The positioning error was found to be 0.538 mm.

The results of the preceding simulations, as well as those of three others, are presented in the Table 3.2.

Table 3.2 — Summary of simulation results for a rectangular probe

Position of the probe centroid	Positioning error for the three electrode sensor (mm)
8 mm, 85° (with respect to the center of lower-most electrode)	0.09
Probe located at the middle of the line connecting electrodes A and C, probe rotated 45° CCW	0.838
12 mm, 105° (with respect to the center of lower-most electrode), probe rotated 90°	0.538
12 mm, 65° (with respect to the center of lower-most electrode)	Not intersecting

As it is noticed from the lowest row of Table 3.2, when the probe was located at 12 mm and 65° with respect to the center of electrode A, no result was obtained from the simulation. Therefore, the four sensing element layout is considered here.

3.2.2. Calibration of the sensor with four sensing elements

Once again, the rectangular probe was located at 12 mm and angle of 65° with respect to the center of electrode D. These are the corresponding obtained charges:

For electrode A: 1326.5660 pC

For electrode B: 754.0258 pC

For electrode C: 583.1396 pC

For electrode D: 688.1919 pC

Redoing the triangulation leads into:

--In triangle ABC: no intersection of the isocharge contours

--In triangle ACD: no intersection of the isocharge contours

--In triangle ABD: x= 6.3497 mm y= 0.9759 mm

--In triangle BCD: x= 5.4631 mm y= 0.8485 mm

Using the results of triangles ABD and BCD results in:

x= 5.9064 mm y= 0.9122 mm

This time the target point is located at x = 5.0714 mm and y = 0.8757 mm. The corresponding positioning error is 0.836 mm. A view of the four triangles along with their isocharge contours is provided below in Figure 3.15.

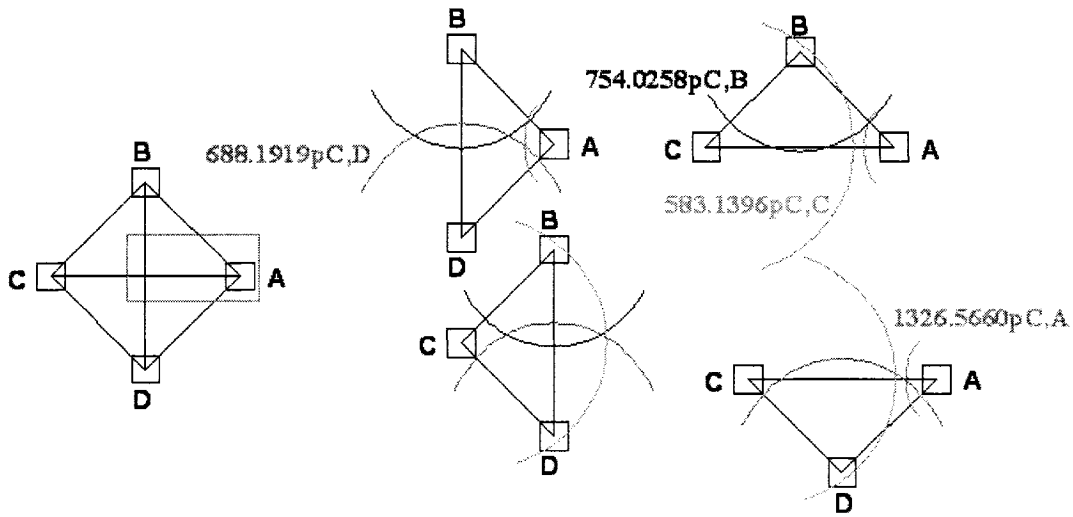

Figure 3.15 — Simulation with a rectangular probe for the four sensing element layout

Therefore, although two of triangles (ABC and ABD) were never used in calculations and no intersection occurred in them, the other two were successfully used and finally an accurate and acceptable result was obtained.

Similar to the case of the triangular probe, since the preceding cases all end in good results for the four sensing element layout, the associated calculations and figures will not be presented hereafter.

In Figure 3.16, numerous isocharge contours for all four sensing elements are put on the same picture. These contours were created by moving a force of 1 N across different points of the central area of the sensor. The isocharge contours shown here were obtained by moving a circular probe of 1 mm radius. For probes with different shapes, the isocharge contours may change according to the shape. Nonetheless, Figure 3.16 gives a clear view of how isocharge contours are created and located on the sensor area.

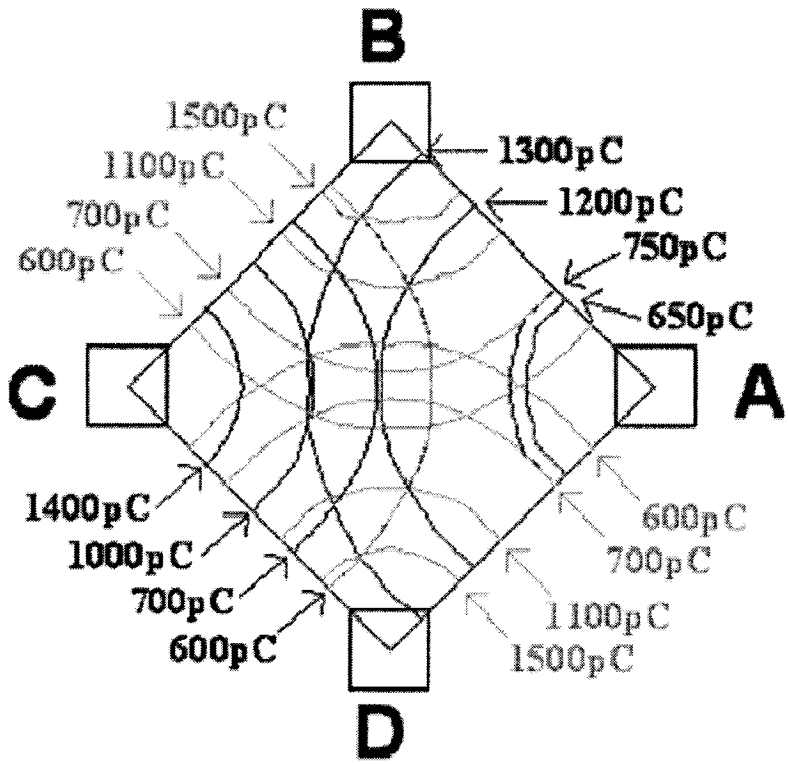

Figure 3.16 — Isocharge contours for all four sensing elements under a force of 1 N

3.3. Simulation results for a uniaxial film

Upon having a quick look on the curves plotted in figures 3.5 & 3.7, questions might be raised on why the curves are almost attached to each other and why they are so close. In response, a similar mapping scheme was performed on a three-electrode layout, with exactly the same dimensions for electrodes, same distances and same angles with respect to each other and the center of membrane. However, this time, it was assumed that the whole pattern was developed on a uniaxial film with the following piezoelectric coefficients:

$$d_{31} = 18\ \frac{pC}{N} \quad \text{and} \quad d_{32} = 2\ \frac{pC}{N}$$

This can be compared with the coefficients for a biaxial film which are $d_{31} = d_{32} = 8\ \frac{pC}{N}$. Referring to a mapping scheme identical to what is illustrated in Figure 3.4, the relevant output curves are shown in figures 3.17 and 3.18.

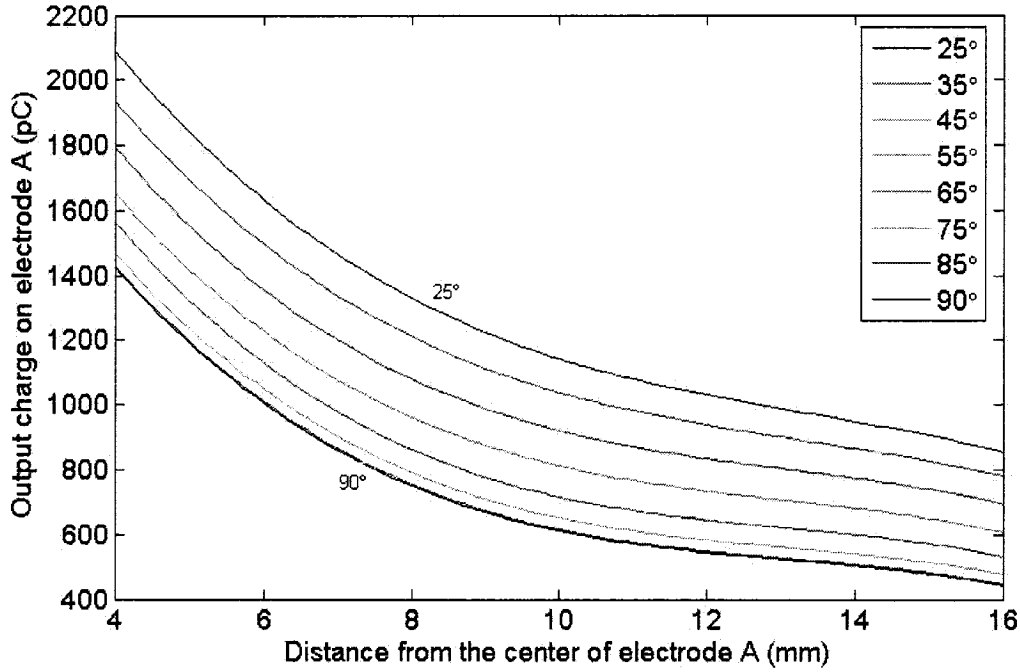

Figure 3.17 -- Charge versus distance curves for electrode A, triangular probe, unaxial film

And with respect to electrode B:

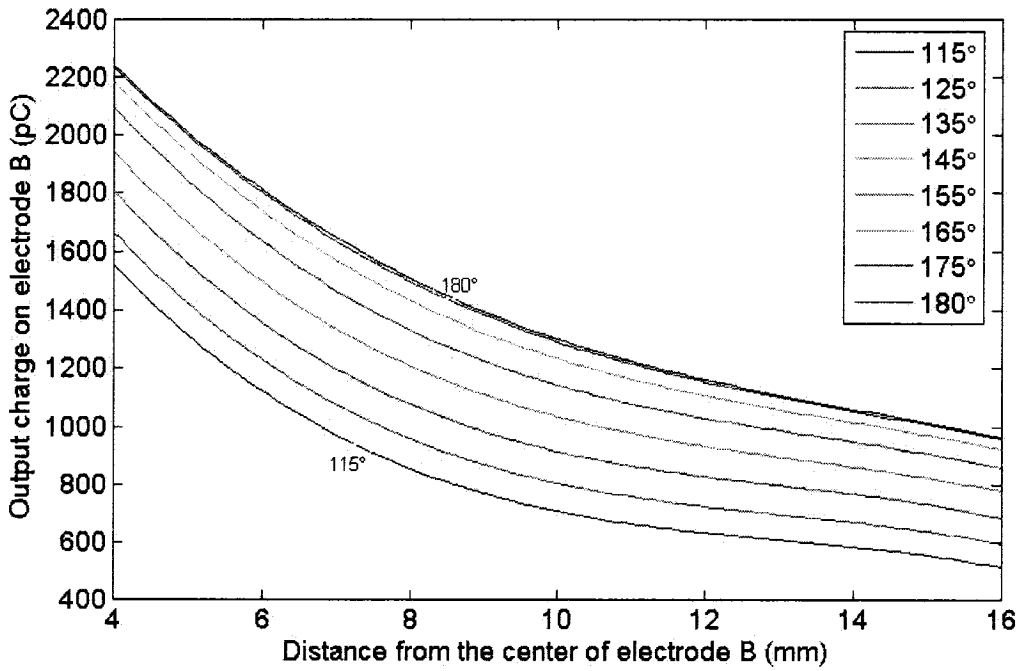

Figure 3.18 -- Charge versus distance curves for electrode B, triangular probe, uniaxial film

As noticed in both figures, the charges vs. distance curves are more distinct and separated. This is a proof of how effective the piezoelectric coefficients can be in the behavior of the system. In these simulations, similar to the triangular probe, the load was taken as 1 N. The mentioned angles are the angles between drawn direction and the lines along which the probe moves.

3.3.1. An equilateral triangular probe

First set of simulations was done for a three-sensing element layout. A triangular probe of the same size, with a side of 7 mm, was selected again. Once again in all the simulations the load was taken as 1 N. As an example of a simulation, the probe was assumed to be at 8 mm and at an angle of 135° with respect to the center of electrode A. Furthermore, the probe rotated 90° counterclockwise. This is depicted below in Figure 3.19.

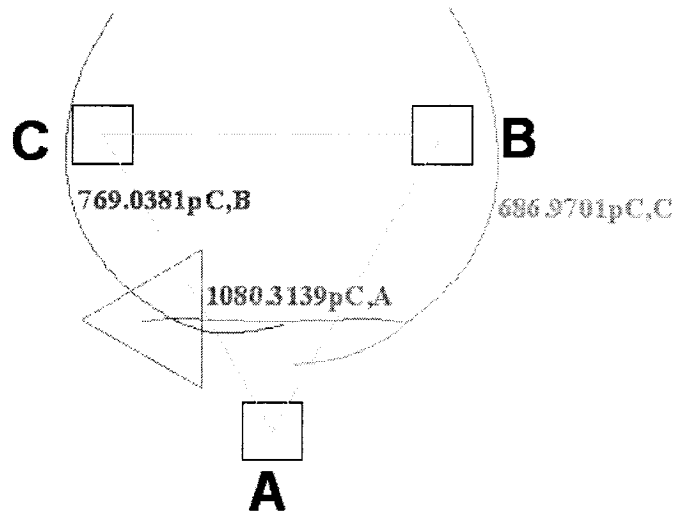

Figure 3.19 — Second simulation for a uniaxial film

There is no result from this simulation because as it shows, the isocharge contours do not intersect with each other.

Because of the unexpected results of some of the previous simulations, as in the biaxial case the four sensing element layout was approached once more. The results are presented in Table 3.3 and are compared with those obtained from the preceding simulations.

Table 3.3 — Summary of simulation results for a rectangular probe

Position of the probe (its centroid)	3-electrode (mm)	4-electrode (mm)
8 mm, 85° (with respect to the center of lower-most electrode)	3.158	Not intersecting
8 mm, 135° (with respect to the center of lower-most electrode), probe rotated 90° CCW	Not intersecting	0.907
12 mm, 105° (with respect to the center of lower-most electrode), probe inverted	1.1822	Not intersecting

Due to the poor and unexpected results of simulations with a triangular probe, instead of running another set of simulations with a rectangular probe, the conclusions would be made in the section 3.5.

3.4. Dependency on the magnitude of the applied load

Following the preceding discussions, several important questions could be raised at this stage: How do the isocharge contours vary with the magnitude of the applied load? Assuming that the position of the load is fixed at a certain point, does the triangulation technique function well for positioning the probe no matter how large the applied load is? How do the output electrical charges on the electrodes alter with the magnitude of load?

To answer these and other related questions, a number of simulations in ANSYS were done on both three-electrode and four-electrode sensors, biaxial films which are described on the oncoming sections. Throughout the simulations the probe was considered equilateral triangular in shape, with a side of 7 mm.

3.4.1. Effect of force on the values of output charges

The probe was put at the center of the membrane and rotated 90° clockwise. The related curves and data are presented in Figure 3.20 and Table 3.4, followed by a set of equations.

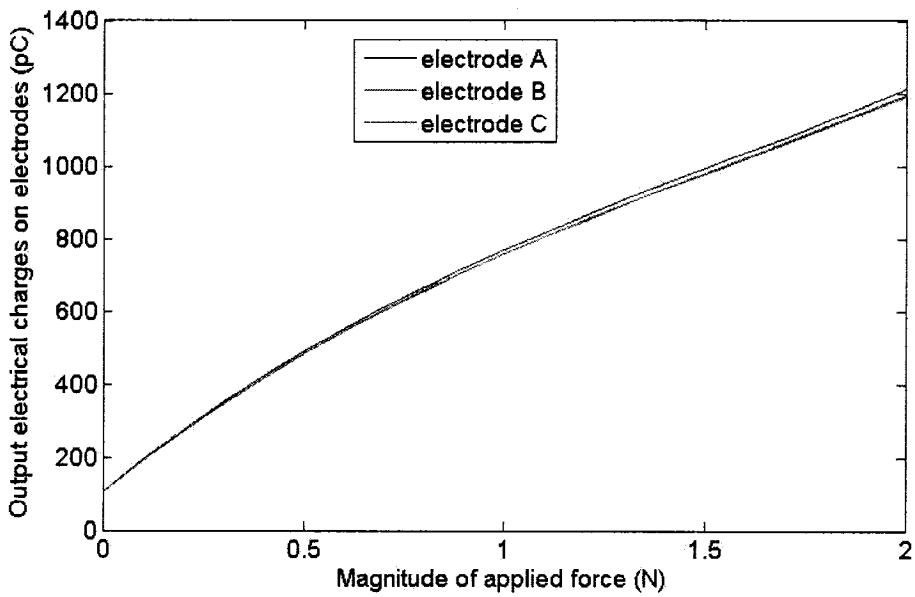

Figure 3.20 -- Charge versus force curves; a three-sensing element layout

Table 3.4 — First set of charge versus force data

Magnitude of applied force (N)	Charge on electrode A (pC)	Charge on electrode B (pC)	Charge on electrode C (pC)
0.25	313.8290	310.1001	309.3626
0.5	489.8100	483.8212	482.6479
1.0	769.4361	759.8014	757.9298
2.0	1210.9906	1195.4595	1192.4616

The associated equations are:

$$\begin{cases} ch_A = 65.389f^3 - 307.326f^2 + 905.811f + 105.562 \\ ch_B = 64.59f^3 - 303.596f^2 + 894.324f + 104.485 \\ ch_C = 64.428f^3 - 302.852f^2 + 892.093f + 104.261 \end{cases}$$

The most distinguishable feature of the above set of equations is that they are similar to each other. This is not surprising because the load is applied at the center of the membrane and virtually at the same distance from all three electrodes. Consequently the charges should vary the same way. However, for forces above 0.5 N, all the curves were still nonlinear. The same was observed when the probe was put at other points and the force was increased.

3.4.2. Effect of force on the accuracy of triangulation technique

Considering that a biaxial film with four electrodes is the most reliable model for yielding accurate results (based on the preceding discussions), the following simulations will cover a four-electrode pattern as well. Here, it will be investigated whether the triangulation method can function properly for another magnitude of force, 2 N this time.

For the first simulation, the triangular probe was put at 8 mm and 85° with reference to the center of the electrode D. The generated curves are shown below in Figure 3.21.

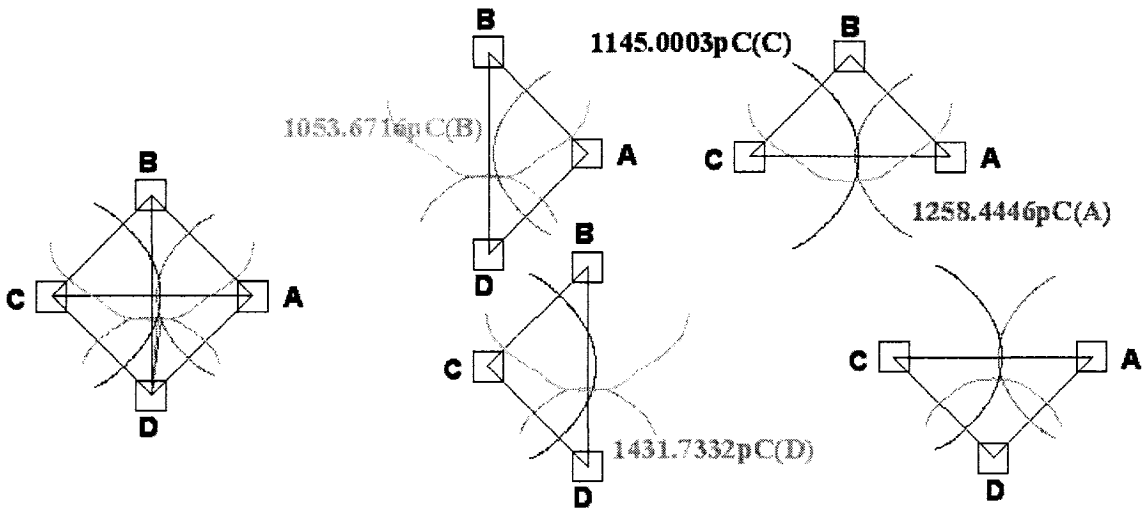

Figure 3.21 – First set of isocharge contours resulting from a force of 2 N

Fortunately, in all four triangles the isocharge contours cross each other. The positioning error is 0.253 mm.

In the second simulation, the triangular probe was put at the center of the membrane and rotated 90° clockwise. The generated curves are shown below in Figure 3.22.

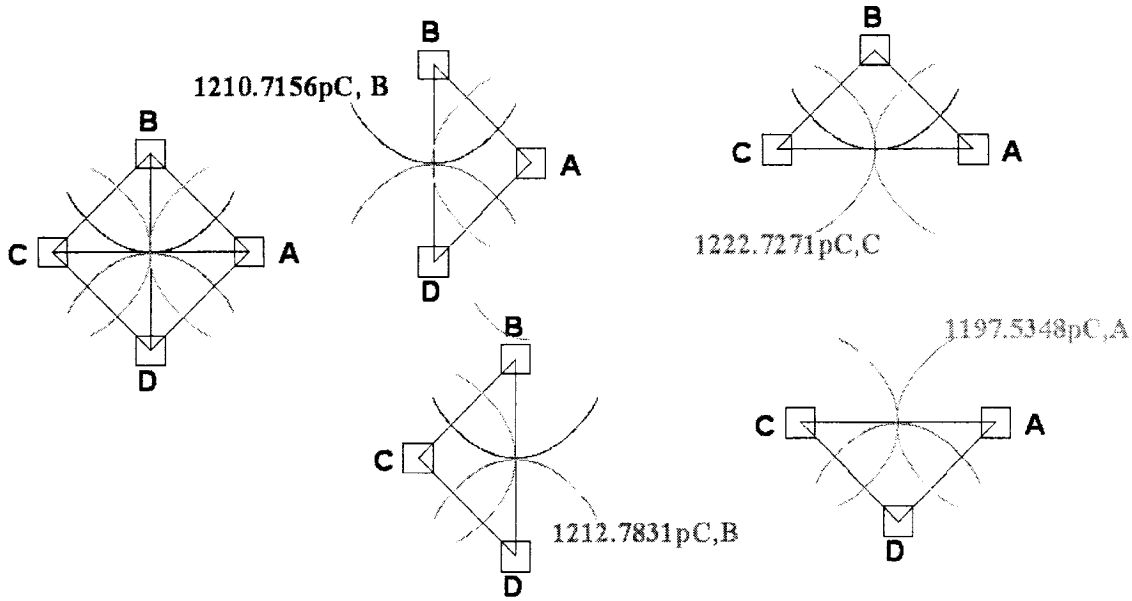

Figure 3.22 -- Probe located at the center of membrane, rotated 90 degrees CW

In two of the four triangles, ABD and BCD, the isocharge contours do not cross each other at three points. However, in the other two, the intersections do occur resulting in a positioning error of 0.267 mm.

The results of the above simulations, as well as those of two other ones, are summarized below in the Table 3.5.

Table 3.5 — Summary of simulation results for a triangular probe

Position of the probe centroid	Positioning error for the three electrode sensor (mm)
8 mm, 85° (with respect to the center of lower-most electrode)	0.253
Probe located at the center of the membrane, rotated 90° CW	0.267
16 mm, 75° (with respect to the center of lower-most electrode)	0.186
8 mm, 135° (with respect to the center of lower-most electrode), rotated 90° CCW	0.145

The related conclusion is presented in section 3.5.

3.4.3. Effect of thickness of the PVDF film on the charge versus force variation

Considering the results reported in the section 3.4.1, the main reason for the nonlinear variation of output charges with respect to the force can be stated as "nonlinear geometrical deformation" of the membrane. Because of the dimensions of the PVDF film and its very high radius-to-thickness ratio, the deformation of this film can be categorized as a "large-deformation problem". This problem becomes an issue when a film or membrane is extremely thin. With that in mind, it would be interesting to see how a thicker membrane behaves upon subjection to the same amounts of load. Do the output charges of electrodes on a thicker PVDF film have a linear relation with the magnitude of force? To answer these questions, first, the website of GoodFellow company, a PVDF manufacturer, was consulted to see if there existed other commercially available, thicker PVDF films. It was noticed that PVDF films are produced in thicknesses of up to 1mm. As two arbitrary choices, two PVDF films with thicknesses of 110 μm and 1 mm were chosen. A three-electrode layout was assumed and various loads were applied through the same triangular probe at 4 mm and 60° with respect to the center of electrode A (the lowermost electrode). The results are juxtaposed in the figures 3.23, 3.24 and 3.25 to see the effect.

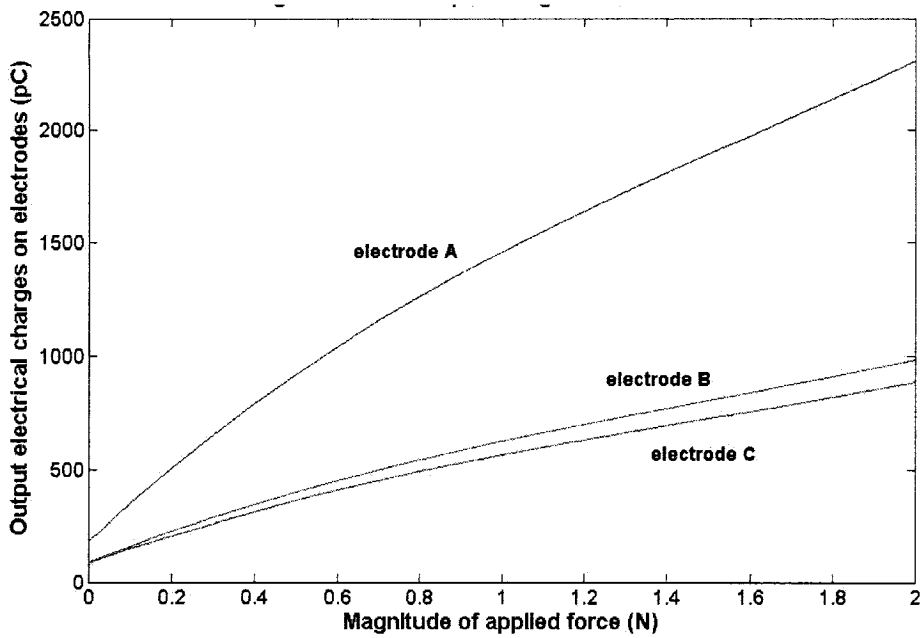

Figure 3.23 – Curves showing variation of output charge vs. force for a 25 micron film

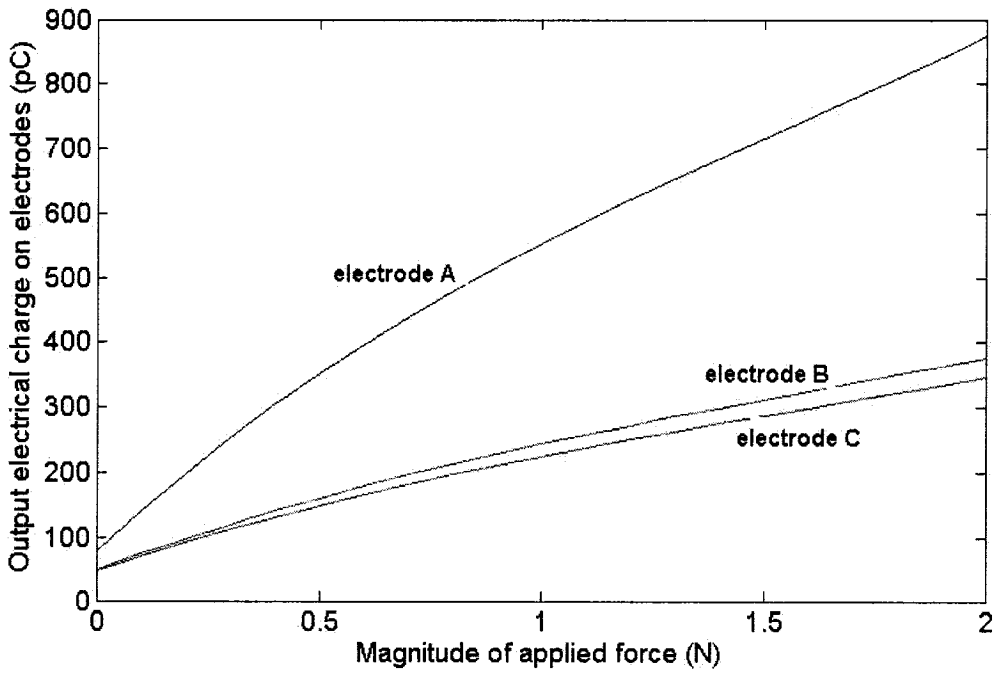

Figure 3.24 -- Curves showing variation of output charge vs. force for a 110 micron film

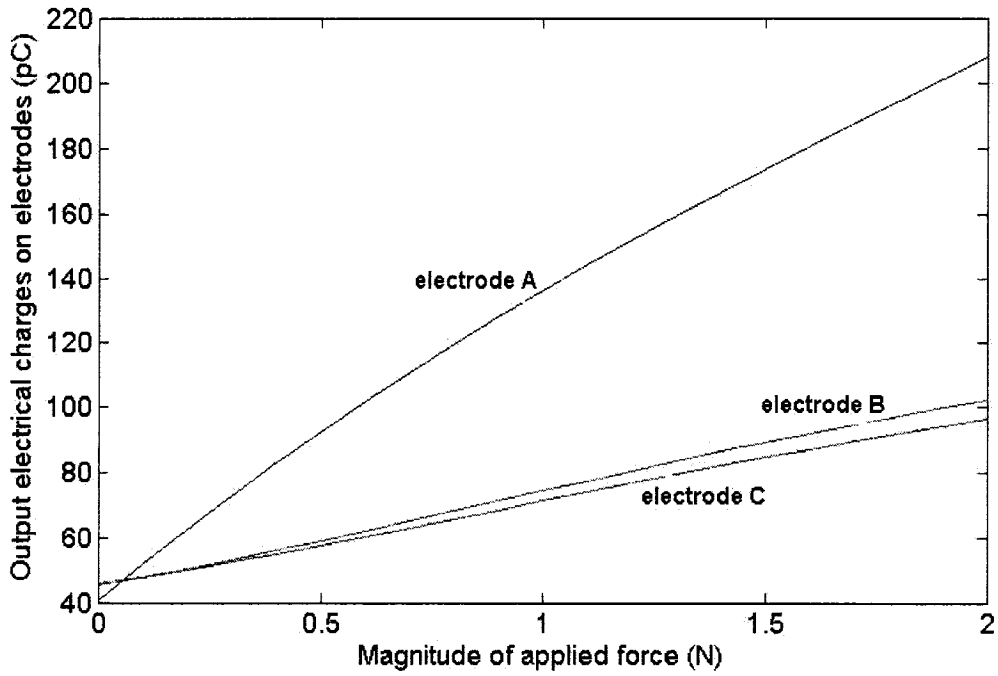

Figure 3.25 -- Curves showing variation of output charge vs. force for a 1 mm film

As perceived from the three previous figures, increase in thickness drives an enhancement in the linearity of the sensor response for all three electrodes. However, the nonlinearity still exists. To verify that, these are the equations relating charge to force when the thickness of PVDF film is 1 mm:

$$\begin{cases} ch_A = 126.3f^3 - 592.4f^2 + 1743.9f + 183 \\ ch_B = 52.679f^3 - 247.820f^2 + 731.498f + 90.838 \\ ch_C = 47.189f^3 - 222.109f^2 + 656.633f + 84.974 \end{cases}$$

The coefficients of 2^{nd} and 3^{rd} degree terms are not negligible at all so a linear approximation is prone to great inaccuracy. Furthermore, with the increase of film thickness higher strains and stresses will develop along the thickness direction of the film. This leads into a bigger role for the d33 coefficient and a third source of charge

generation. Addition of this charge can impair all efforts for linearization of sensor and make it nonlinear.

With all the above results in mind, it can be concluded that the triangulation technique can be used for even larger loads, at least up to 2 N. The only setback is that the related electrical charges on the electrodes do not vary linearly. Therefore, in order to find both magnitude and position of an applied load, the following solutions are recommended:

1) The sensor can be used in a specific band of forces, for instance up to 0.5 N. In this range, the variation of charge against force is linear and interpolations are easier and more accurate.
2) A huge database, or actually a lookup table, for different forces and positions should be created and stored in a computer. Then, for each unknown set of variables (force and position), the results should be compared or matched with the lookup table. The closest one gives the answer. Of course, in this method, the shape and size of an object in contact with the sensor must be known in advance. Moreover, the test results for the particular shape of the object should have been obtained.

3.5. Summary

In this chapter, the application of the sensor for detecting the position and magnitude of an applied force was discussed. After a brief description of the triangulation method, which was used for detecting the position of the applied force, the calibration procedure of the sensor was explained. Calibration was based on a mapping scheme in which, force was applied at different selected points within the central area of the sensor, confined to the edges of the sensing elements. Using the calibration method, and by applying the force through two shapes of probe, triangular and rectangular, a number of charge against distance curves were obtained. These curves were used for creating isocharge contours. For any magnitude of the applied force, the intersection point of the isocharge contours was the point at which the force was applied. When the applied force was concentrated, or when the object in contact with the sensor was circular, this method worked very well for a three-sensing element layout. However, when the applied force was applied through non-circular objects, such as a triangular or a rectangular probe, it was shown that a four-sensing element layout gave more accurate results. By doing the triangulation four times for a four-sensing element layout, and taking the averages of the coordinates of the intersection points, a more accurate knowledge of the application point of the force was obtained. It was shown that for both three- and four-sensing element layouts, using a biaxial film gave better results, compared to using a uniaxial film. As for the variation of the output charge against force, the sensor was linear up to 0.5 N. For magnitudes of forces beyond this value, the variation of the output electrical charge versus the magnitude of the applied force was found to be a cubic polynomial.

Chapter 4 - Detecting the orientation of planar objects

Another point of interest in studying this sensor is investigating its sensitivity to orientation of an object. If the object in contact with the sensor area has sharp corners or irregularities, e.g., a rectangle or a triangle, then the outputs of the sensor depend not only on the location of the object but also on its orientation with respect to the sensing elements. As reported in sections 3.2 and 3.3, the orientation of the probe has a minimal impact on the ability of the sensor to detect and locate the position of its centroid. Yet, there might be some cases in which the unknown parameter is the orientation of the object. In order to find the answer, a number of simulations were implemented with a rectangular 14 mm by 7 mm probe as follows:

1) Under a pre-determined load, the rectangular probe is rotated. Then, the responses, or output charges versus rotation angles, are plotted.
2) Normalization of the plots and inverse relations are investigated. In other words, attempts are made toward finding some information about the force such as its magnitude, the angle of rotation of the probe, or both, using the output electrical charges.
3) At a specific angle, for instance 0°, loads with different magnitudes are applied. Then, the plots of output charges versus loads are produced.

4.1. Rotating the rectangular probe under fixed magnitudes of force

The force is distributed over the area of the rectangular probe to create a uniform pressure. Then, the probe is rotated between 0° to 180° with respect to the x-axis, namely, the drawn direction, in increments of 10°. This is illustrated below in Figure 4.1.

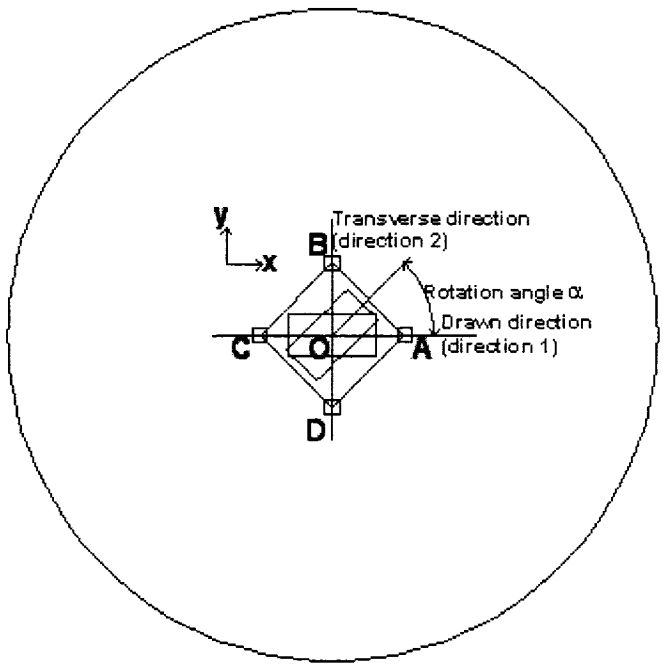

Figure 4.1 – Schematic representation of rotating a rectangular probe

The letter O in the above figure represents the center of the circle, as well as the centroid of the rectangular probe. This simulation is repeated three times for forces with the different magnitudes of 0.5, 1, and 2 N. As described in Chapter 2, SHELL 63 element was selected for meshing the membrane area.

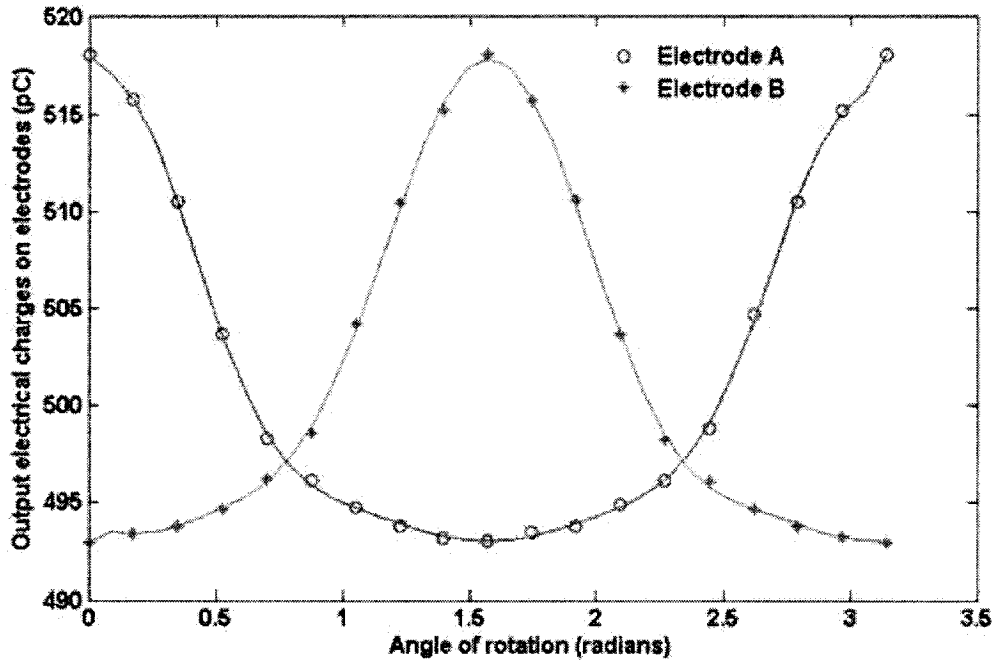

Figure 4.2 -- Charge versus angle of rotation for electrodes A and B when force is 0.5 N

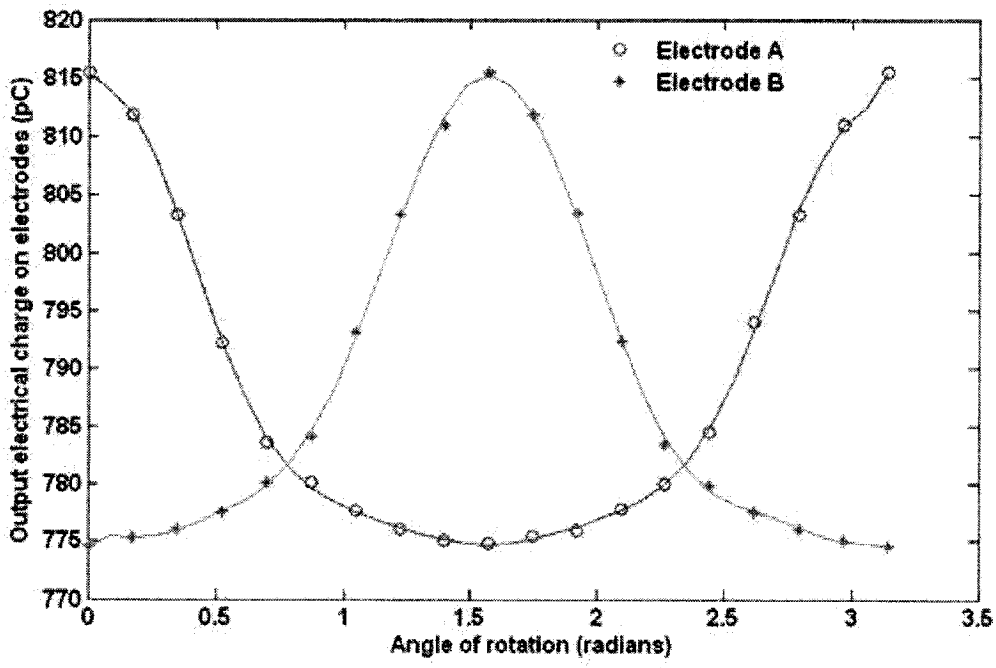

Figure 4.3 -- Charge versus angle of rotation for electrodes A and B when force is 1 N

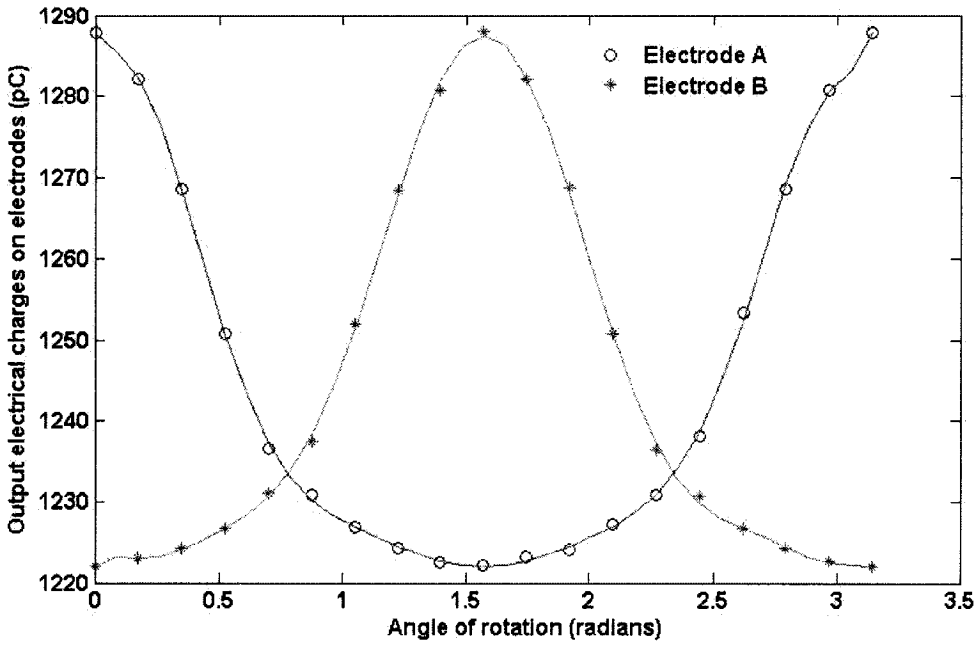

Figure 4.4 -- Charge versus angle of rotation for electrodes A and B when force is 2 N

It is evident that the trend in the variation of charge against angle of rotation is a combination of descend and ascend for both electrodes. As it is clear in all the above three figures, for electrode A there is a unique behaviour: the charge has its maximum amount at an angle of 0° and as the probe keeps rotating toward an angle of 90°, its charge follows a declining trend and reaches its minimum amount at 90° angle. Then, it starts increasing until it peaks again at 180°. The nature of this behaviour remains the same for all magnitudes of loads. Understandably, however, there are differences in the the range of variation of the output charge and its minimum and maximum values.

Likewise, for electrode B there is a unique type of behaviour for all loads. However, this time it is exactly opposite to that of electrode A. For electrode B, the output charge starts from a minimum at 0° and peaks at 90°, then decreases to its original amount at 180°.

One thing that was expected was that, as the sharp corner of the rectangular probe gets closer or points more toward each electrode, the amount of accumulated charge on that electrode increases. This can be attributed to the stress concentration effect; the closer the sharp corner gets to the electrode edge, the higher the stress concentration becomes and therefore the produced charge increases. This is clearly seen in all the figures and is in accordance with the results obtained for a three-element sensor tested by Dargahi [71].

An interesting point here is that, each pair of curves intersect with each other at two points. These two points correspond to the rotational angles of 45° and 135°, respectively. Considering the top view of the entire model shown in Fig.4.1 and the way the angle of rotation is defined, this is expected.

4.1.1. Results of rotation under a force of 1 N

The table 4.1 shows how the charges on all of the four electrodes vary under a constant force of 1 N with rotation of the probe.

Table 4.1 -- Variation of charges versus angle of rotation for all 4 electrodes when force=1N

	0	10	20	30	40	45	50	60	70	80	90
A	815.4188	811.8675	803.3692	792.2980	783.5395	783.2460	780.0506	777.6315	775.9746	774.9705	774.7457
B	774.5725	775.2556	775.9823	777.4814	780.0890	782.2057	784.0523	793.1390	803.3128	810.9675	815.5069
C	815.4861	811.7975	803.4135	792.3564	783.4222	783.1617	779.9739	777.4793	776.0407	774.9639	774.7213
D	774.6369	775.2645	775.9630	777.7834	780.0778	782.1797	784.4396	793.9774	803.3620	810.9844	815.5024

	100	110	120	130	135	140	150	160	170	180
A	775.3645	775.9277	777.7801	780.0293	782.1346	784.4550	793.9624	803.3359	810.9745	815.4188
B	811.8178	803.4393	792.3478	783.4586	783.1180	779.9059	777.4770	775.9895	775.0339	774.5725
C	775.2029	776.0710	777.7899	780.0258	782.1437	784.3987	793.9342	803.3042	810.9475	815.4861
D	811.8214	803.2301	792.3184	783.4363	783.0894	779.8954	777.4710	776.0578	775.0733	774.6369

Now for verifying the existence of an inverse relation (known output charge⇒precise angle of rotation), the 1 N force is taken as an example. In this case, based on the plotted curves and the known data, the following equation is derived between output charge (c) and the angle of rotation (a) for electrode A:

$$c_A = 4.6045a^{10} - 71.577a^9 + 472.81a^8 - 1728.4a^7 + 3808.1a^6 - 5141.5a^5 + 4092.9a^4 - 1688.3a^3 + 242.11a^2 - 28.251a + 815.41 \quad \text{(Eq.4.1)}$$

This is of course a non-linear relation between the charge and the angle of rotation, governed by a 10^{th} degree polynomial. The angle (a) is in radians. As the first try, the charge was assumed to be 810 pC. This is the obtained angle:

0.226171 rad

Upon running a simulation with this angle (which is 12.959°) and a force of 1 N, the charge was 810.397 pC which, compared to the 810 pC, corresponds to an error of %0.049. This is acceptable.

Per reading the Table 4.1 and looking at the figures 4.2 to 4.4 carefully, it is noticed that there is not such a big difference in recorded data from electrode A to C. The same is true for electrodes B and D. As a result, electrodes C and D could be ignored. Just studying electrodes A and B, at least for the case of 1 N force, suffices. For electrode B, the relation between charge and rotational angle is derived as

$$c_B = -4.3112a^{10} + 68.534a^9 - 456.43a^8 + 1648.7a^7 - 3498.2a^6 + 4431.8a^5 - 3299.4a^4 + 1393.3a^3 - 295.58a^2 + 27.241a + 774.57 \quad \text{(Eq.4.2)}$$

in which c_B means charge on electrode B. The angle "a" is again in radians.

The main obstacle here is having an educated guess on what charge on electrode B appears when charge on element A is 800pC. In all of the simulations, the data for all four elements are recorded; so it is easy to have both of the charges at the same time. However, here it is virtually impossible to make smart selection of pairs of charges for electrodes A and B. No clear clue exists as to what the charge on electrode B will be when the charge on electrode A is a certain amount and vice versa. That, in turn, enforces the selection of just one element at time; electrode A is chosen.

As the second try, it is assumed that the measured charge on electrode A is 800 pC. Then the angle of rotation will be:

$c_A = 800$ pC $\Rightarrow$ the angle of rotation = 0.3997 rad or 22.901°

A new simulation was performed in ANSYS, under exactly the same conditions, but with this new angle of rotation. Charge on electrode A was calculated to be 801.553 pC, with an error of %0.194. So this was also acceptable.

As the third try, this time the charge was assumed to be 785 pC. The obtained angle of rotation is

0.671085 rad or 38.445°

Running a new simulation yields an output charge of 783.666 pC which corresponds to an error of %0.17. This time the error is again relatively small and negligible.

As the fourth try, this time the charge was assumed to be 775 pC. Substituting this value in the equation yields an angle of

1.319616 rad or 75.608°

The associated charge obtained from the simulation was 775.398 pC, which amounts to an error of %0.051. This time the error has even decreased, and is truly negligible.

A summary of the preceding results is presented below in the Table 4.2.

Table 4.2 — Summary of the estimation errors for a force of 1 N

Assumed charge on electrode A (pC)	810	800	785	775
Calculated angle of rotation (°)	11.176	22.901	38.445	75.608
Calculated charge on electrode A (pC)	810.363	801.553	783.666	775.398
Associated error in guessing the angle	%0.049	%0.194	%0.17	%0.051

As noticed above, in all cases, the estimation error is very low and thus ignorable. Therefore, it can be concluded that interpolation using polynomials serves very well, at least for computing the rotational angle.

4.1.2. Results of rotation under a force of 0.5 N

Next series of simulations were performed with an applied force of 0.5 N and rotating the probe in the same manner from 0° to 180° at the same location. The equation governing the variation for this case is

$$c_A = 2.8857a^{10} - 44.854a^9 + 296.24a^8 - 1082.6a^7 + 2384.5a^6 - 3217.5a^5 + 2559.2a^4 - 1054.7a^3 + 151.52a^2 - 17.685a + 517.98 \quad \text{(Eq.4.3)}$$

As the first try, the above equation was set equal to 510 pC. Then angle "a" will be:

0.359831 rad or 20.617°

A simulation was conducted with a 0.5 N load and this rotational angle. The resulting charge on element A was 509.333 pC. This results in an acceptable error of %0.131.

As the second try, the measured charge on electrode A is taken as 502.5 pC. Then, the angle of rotation is computed as

$c_A = 502.5$ pC $\Rightarrow$ angle of rotation = 0.554947 rad

A new simulation was done in ANSYS, under exactly the same conditions yet with this new angle of rotation. Charge on electrode A was calculated to be 501.700 pC, associated with an error of %0.159.

As the third try, the measured charge on electrode A is set equal to 495 pC. Then the angle of rotation will be:

$c_A = 495$ pC $\Rightarrow$ angle of rotation = 0.997616 rad

An ANSYS simulation showed the charge on electrode A to be 494.874 pC. An error of %0.025 is reported this time.

Table 4.3 – Summary of the estimation errors for a force of 0.5 N

Assumed charge on electrode A (pC)	510	502.5	495
Calculated angle of rotation (°)	20.617	31.796	57.158
Calculated charge on electrode A (pC)	509.333	501.700	494.874
Associated error in guessing the angle	%0.131	%0.159	%0.025

Once again as tabulated above, in all cases, the estimation error is very low and thus ignorable. Therefore, it can be concluded that interpolation using polynomials serves very well, at least for computing the rotational angle.

Now, with the above data in mind, it is suggested to normalize the already-developed equations and introduce lookup tables. This is described in the next section.

4.2. Normalization of the charge versus rotational angle curves

Normalization was begun with the equation 4.1, which demonstrates the variation of charge versus angle of rotation when the load is 1 N:

$$c_A = 4.6045a^{10} - 71.577a^9 + 472.81a^8 - 1728.4a^7 + 3808.1a^6 - 5141.5a^5 + 4092.9a^4 - 1688.3a^3 + 242.11a^2 - 28.251a + 815.41$$

Dividing all the coefficients by 815.41 leads into

$$C_A = (5.647e\text{-}3)a^{10} - 0.088a^9 + 0.580a^8 - 2.120a^7 + 4.670a^6 - 6.305a^5 + 5.019a^4 - 2.070a^3 + 0.297a^2 - 0.035a + 1 \quad \text{(Eq.4.4)}$$

When the load is 0.5 N

$$c_A = 2.8857a^{10} - 44.854a^9 + 296.24a^8 - 1082.6a^7 + 2384.5a^6 - 3217.5a^5 + 2559.2a^4 - 1054.7a^3 + 151.52a^2 - 17.685a + 517.98 \quad \text{(Eq.4.5)}$$

the normalized relation will be

$$C_A = (5.571e\text{-}3)a^{10} - 0.087a^9 + 0.572a^8 - 2.090a^7 + 4.603a^6 - 6.212a^5 + 4.941a^4 - 2.036a^3 + 0.293a^2 - 0.034a + 1 \quad \text{(Eq.4.6)}$$

Finally, for the 2 N load case, the normalized equation is

$$c_A = 7.3199a^{10} - 113.79a^9 + 751.65a^8 - 2747.8a^7 + 6054.9a^6 - 8175.8a^5 + 6508.5a^4 - 2682.8a^3 + 381.88a^2 - 44.313a + 1287.8 \quad \text{(Eq.4.7)}$$

which leads to the following normalized equation

$$C_A = (5.684e\text{-}3)a^{10} - 0.088a^9 + 0.584a^8 - 2.134a^7 + 4.702a^6 - 6.349a^5 + 5.054a^4 - 2.083a^3 + 0.297a^2 - 0.034a + 1 \quad \text{(Eq.4.8)}$$

The objective of normalization was to seek an equation in the following format:

$$Y=A_1a^{10}+A_2a^9+A_3a^8+A_4a^7+A_5a^6+A_6a^5+A_7a^4+A_8a^3+A_9a^2+A_{10}a+A_{11}$$

in which $A_{11}=1$, and Y is the normalized output charge developed on electrode A, for a range of forces and rotational angles varying from 0 to 90 degrees. Then, the above equation would have coupled it to a lookup table such as Table 4.4.

Table 4.4 — An example of a suggested look-up table

Range of output charge of electrode A (pC)	Factor for scaling down the coefficients of polynomial	The corresponding normal force (N)
493.051 to 517.993	517.98	0.5
774.7457 to 815.4188	815.41	1
1220 to 1290	1287.8	2

This seems to be doable since the A_i coefficients in the equations 4.4, 4.6 and 4.8 are identical. As a result, by taking the average of A_i coefficient for the previous three equations (equations 4.4, 4.6, and 4.8), this normalized equation was derived:

$$C_A = (5.622e\text{-}3)a^{10} - 0.088a^9 + 0.579a^8 - 2.115a^7 + 4.658a^6 - 6.289a^5 + 5.005a^4 - 2.063a^3 + 0.296a^2 - 0.034a + 1 \qquad \text{(Eq.4.9)}$$

Of course a more accurate way of computing the average values for coefficients is running more simulations with other magnitudes of forces, plotting curves to depict the variation of each A_i against the load, and then dividing the area under this curve by the maximum load. Nonetheless, the already extracted coefficients seem to be plausible enough and their differences are by no means considerable. Apparently, this equation should be used in conjunction with Table 4.4.

In Figure 4.5, the variation of the produced charge developed on electrode A versus the applied force is shown when the load on the probe changes in magnitude (provided that the probe is not rotated or the angle of rotation is 0°. The applied force is set at 0.25, 0.5, 1, 2, 3.5, 5 and 7.5 N.

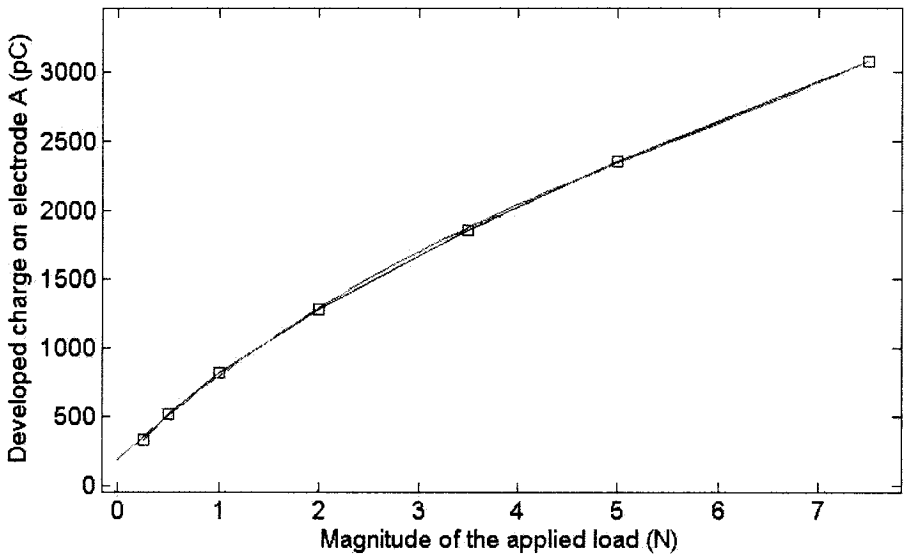

Figure 4.5 — Curve showing the variation of charge on electrode A versus the magnitude of force

In Figure 4.5, the vertical axis is the output charge in pC and the horizontal axis is applied load in Newtons. The data set was fit into a linear 6^{th}-degree polynomial which was found to be:

$$c_A = -0.356f^6 + 7.252f^5 - 56.47f^4 + 218.67f^3 - 480.4f^2 + 1025.3f + 101.41 \quad \text{(Eq.4.10)}$$

Due to the symmetry in geometry and loading, charge on element C is exactly the same as that on element A. Hence, focus is shifted on the behavior of the other two electrodes, namely, B and D. Again, due to the symmetry considerations, just one of them, in this

case element B, will be studied. The curves shown below in Figure 4.6 are associated with the data collected from studying the behavior of electrode B

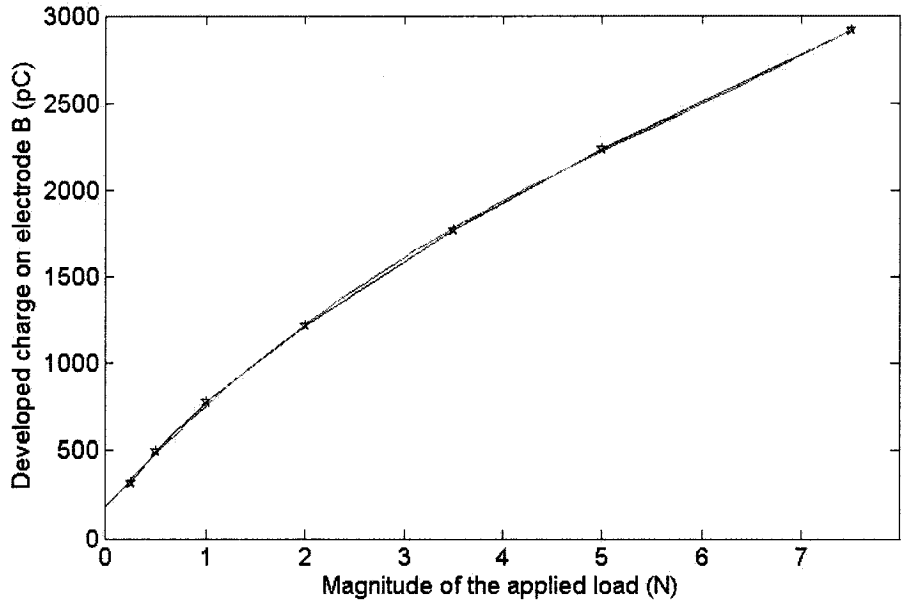

Figure 4.6-- Curve showing the variation of charge on electrode B versus the magnitude of force

and this is the result of curve-fitting

$$c_B = -0.339f^6 + 6.910f^5 - 53.752f^4 + 207.82f^3 - 455.61f^2 + 971.06f + 98.484 \quad \text{(Eq.4.11)}$$

Now back to the equation 4.9 and Table 4.4 and based on what were discussed above, the equation 4.9 can be cast in this form:

$$c_A = \{(5.622e\text{-}3)a^{10} - 0.088a^9 + 0.579a^8 - 2.115a^7 + 4.658a^6 - 6.289a^5 + 5.005a^4 - 2.063a^3 + 0.296a^2 - 0.034a + 1\} * (3.932f^3 - 67.663f^2 + 671.57f + 187.29) \quad \text{(Eq.4.12)}$$

Now, there is a bi-variate equation which incorporates both the angle of rotation and the magnitude of the applied force. Therefore, instead of using the lookup Table 4.4, this equation can be used. The following figure, Figure 4.7, is a three-dimensional illustration

of how the charge on electrode A varies with respect to the angle of rotation of rectangular probe and the force applied on it.

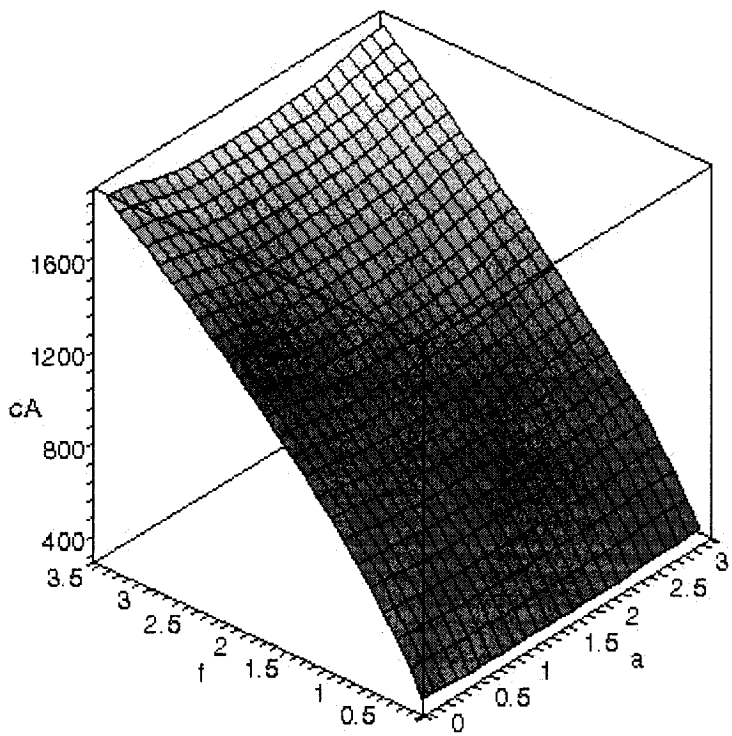

Figure 4.7 -- Surface showing variation of charge on electrode A versus rotation and force

Following a similar discussion, the following equation (Eq.4.13) and three-dimensional surface, Figure 4.8, are derived for the electrode B:

$$c_B = \{-(5.566e\text{-}3)a^{10} + 0.088a^9 - 0.589a^8 + 2.129a^7 - 4.516a^6 + 5.722a^5 - 4.260a^4 + 1.799a^3 - 0.382a^2 + 0.035a + 1\} * (3.744f^3 - 64.245f^2 + 636.42f + 179.6) \qquad \text{(Eq.4.13)}$$

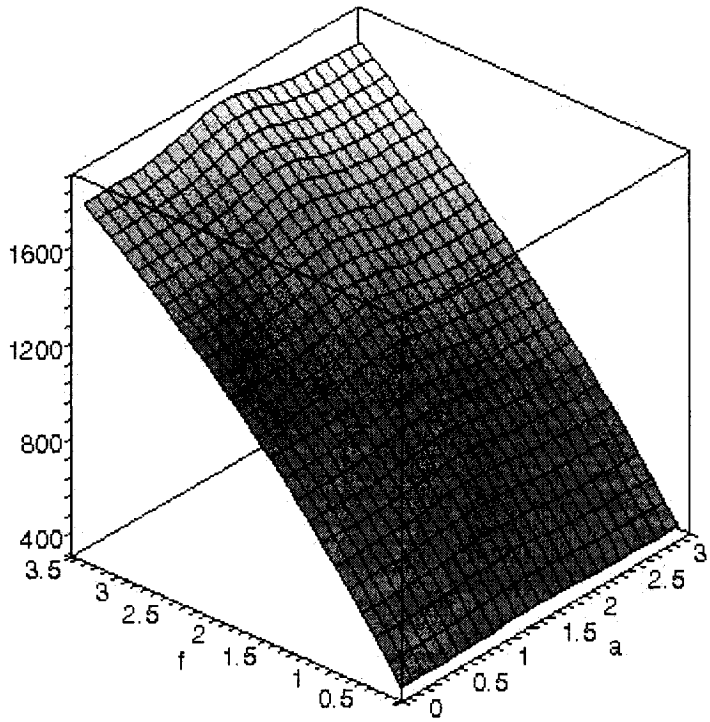

Figure 4.8 — Surface showing variation of charge on electrode B versus rotation and force

In order to investigate the accuracy of the preceding two surfaces, as an example, each of them is intersected with the plane f = 1 N. The resulting curves should be identical to those shown in Figure 4.3. The results are shown in the following figures, Figure 4.9 and Figure 4.10.

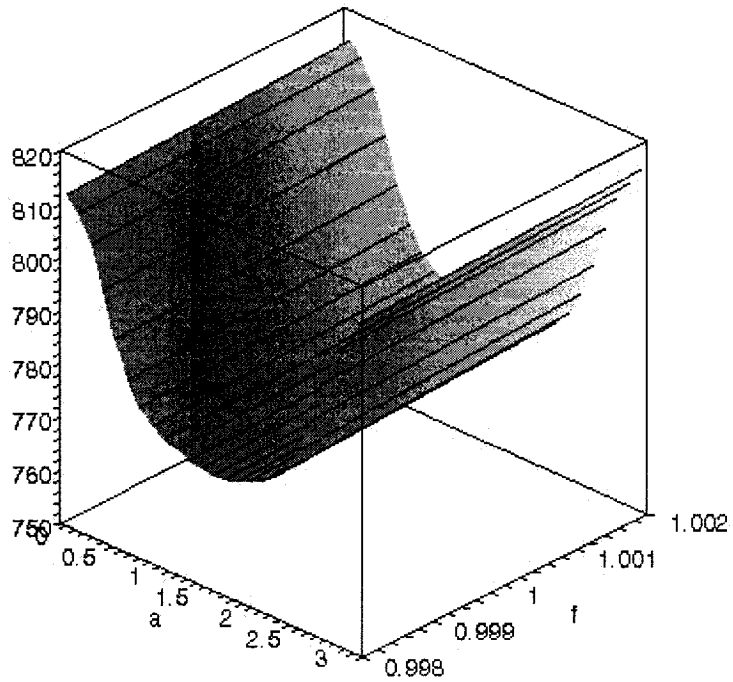

Figure 4.9 — Cross-section showing the charge versus angle of rotation for electrode A when f=1 N

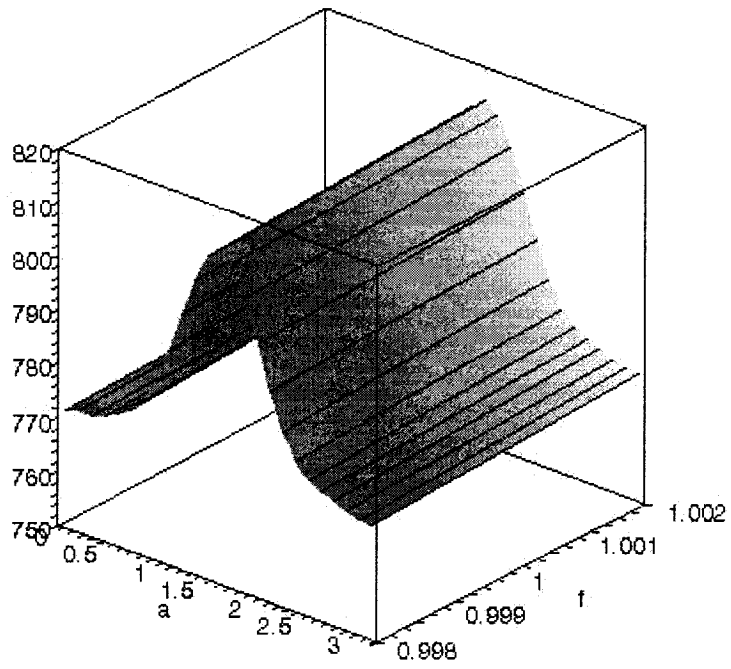

Figure 4.10 — Cross-section showing the charge versus angle of rotation for electrode B when f=1 N

Both of the cross-sections are in excellent agreement with those in Figure 4.3. So, it can be concluded that curve-fitting the data with polynomials can be very accurate.

4.3. Dependency of charge versus rotational angle variation to the magnitude of the applied force

Another point to raise here is how the output charge on the electrodes A and B vary against load at different angles of rotation. In a set of new simulations, first the rotation angle of probe was fixed at a certain amount, and then the magnitude of applied force was varied. The probe was placed at the center of the membrane and fixed at various angles of rotation, varying in increments of 15°. At each of the angles, seven distinct loads were exerted, and the following tables were consecutively developed. The results are presented below in terms of Tables 4.5 and 4.6 and the curves are shown in figures 4.10 and 4.11.

Table 4.5 —Variations of charge on electrode A versus magnitude of applied force at different angles

Applied load(N)	0.25	0.5	1	2	3.5	5	7.5
0°	330.9186	517.9926	815.4188	1285.5662	1861.0251	2357.6680	3074.7370
15°	327.5317	512.5147	806.6272	1273.7729	1841.5369	2331.7033	3048.6809
30°	322.1009	503.6423	792.2980	1250.7828	1808.5984	2289.2054	2992.9576
45°	318.8254	498.1424	783.2460	1236.0298	1786.4875	2262.4128	2951.8836
60°	316.8304	494.7433	777.6315	1226.9267	1773.8005	2244.9666	2934.8950
75°	316.1120	493.4566	775.4363	1223.2715	1767.9400	2253.1875	2919.9589
90°	315.8177	492.9411	774.5725	1220.0613	1765.1786	2235.4733	2916.7023

Table 4.6 -- Variations of charge on electrode B versus magnitude of applied force at different angles

Applied load(N)	0.25	0.5	1	2	3.5	5	7.5
0°	315.8177	492.9411	774.5725	1220.0613	1765.1786	2235.4733	2916.7023
15°	316.2087	493.6134	775.6919	1223.6932	1768.5783	2238.8791	2926.8891
30°	316.7811	494.6581	777.4814	1226.6537	1773.3426	2244.3186	2933.9130
45°	318.4152	497.4850	782.2057	1234.4040	1784.1775	2259.5462	2948.2448
60°	322.4339	504.1732	793.1390	1252.1069	1810.4905	2291.5704	2995.9860
75°	327.3061	512.1518	806.0465	1272.8460	1840.1843	2348.8694	3038.5907
90°	330.9186	517.9926	815.4188	1285.5662	1861.0251	2357.6680	3074.7370

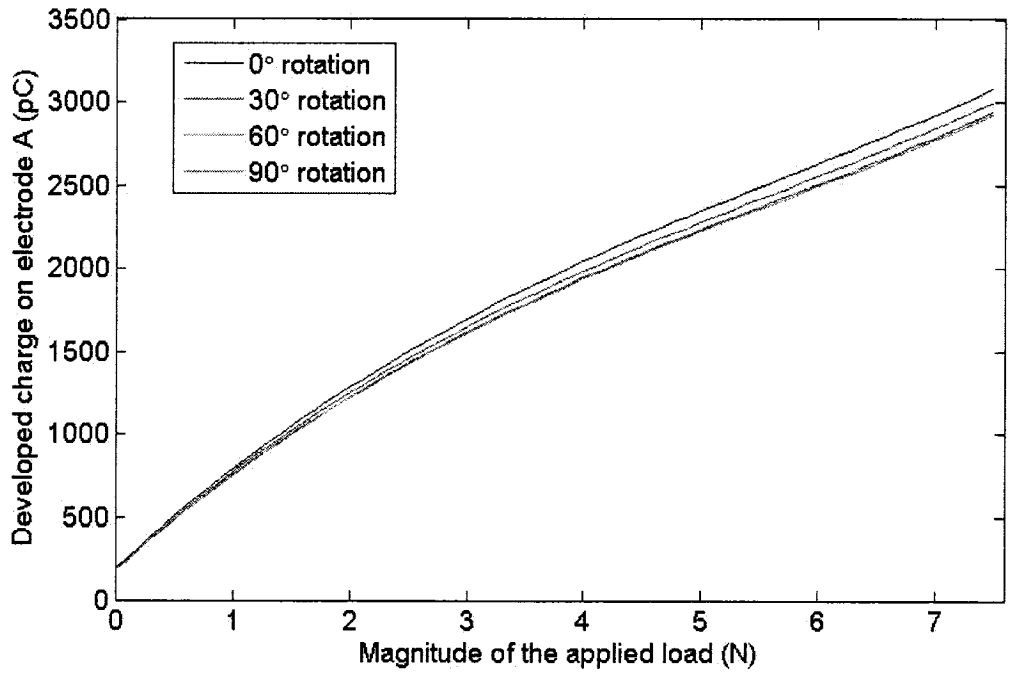

Figure 4.11 — Curves depicting variation of output charge on the electrode A versus the force at different angles

As noticed, the curves follow similar patterns. The upper-most curve corresponds to the 0° angle, and the lower-most one matches the 90°. The other two fill in between.

And for electrode B, the curves are shown below.

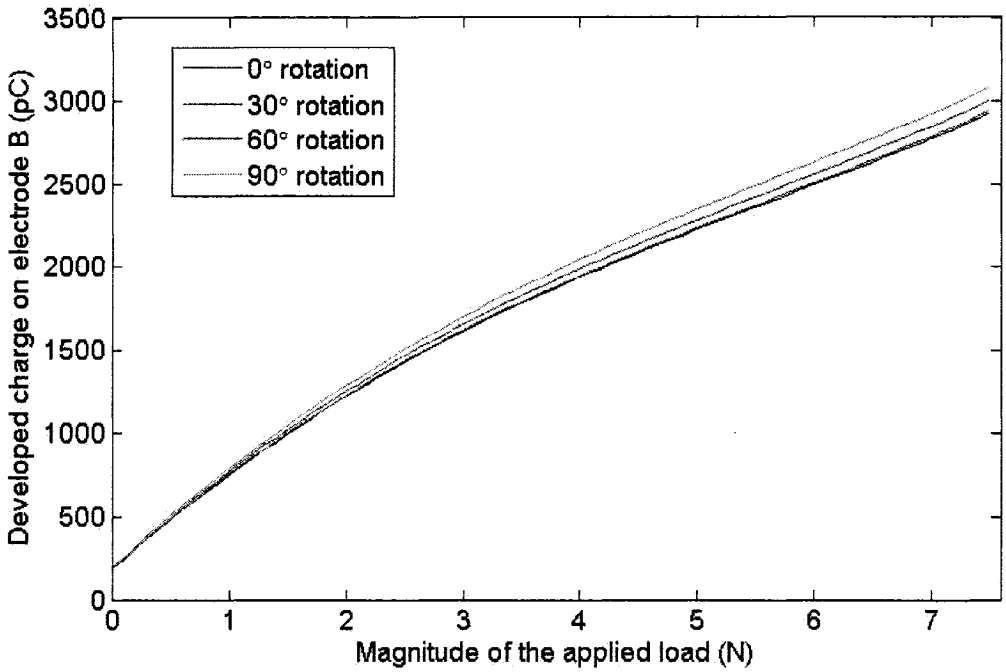

Figure 4.12 — Curves depicting variation of output charge on the electrode B versus the force at different angles

Again, there is not a big difference between the curves. The only difference this time is that the uppermost and lowermost curves correspond to, respectively, 90° and 0° angles.

4.4. Summary

In this chapter, the sensitivity of the sensor to the orientation of the touching object, was investigated. Computer simulations were done by using a rectangular probe of 14 mm by 7 mm size, and applying three magnitudes of forces, namely 0.5 N, 1 N and 2 N. In each simulation, the magnitude of the applied force was fixed, and the probe was rotated between 0° to 180°, in increments of 10°, with respect to the drawn or x- direction of the PVDF film. The obtained charges at different angles were fit into curves, 10^{th}-degree

polynomials. The accuracy of the obtained polynomials was verified by setting them to values in between those of the discrete data. It was noticed that for each magnitude of force, the range of variation of output electrical charge was different. However, all the curves were similar to each other in shape. Therefore, an attempt was made to find a general equation, showing the variation of output charge versus magnitude of the applied force. This was done by normalization of the polynomials. Later, the normalized equation was multiplied by another polynomial, which gave the amount of output charge versus the magnitude of the applied force. In this way, a bi-variate function was obtained, showing the amount of output charge against both the angle of orientation and the magnitude of the applied force. For both electrodes A and B, surfaces were plotted based on their related bi-variate functions. Finally, a different approach was taken to investigate the dependency of the output charges on electrodes on the angles of rotation and magnitudes of the applied force. This time, first the angle of rotation was set at a constant value, and then the magnitude of the force was changed. The results were presented in terms of tables and curves.

Chapter 5 - Experimental works and results

In this chapter, the experimental procedures and the results will be described and discussed. As in the previous chapters which covered the theoretical results, the new set of results will be presented in terms of numbers, figures, graphs and tables.

5.1. Fabrication of the sensor

As previously mentioned, the PVDF film used throughout the experiments was manufactured by the GoodFellow company of the U.S.A. A complete list of its technical specifications including mechanical, electrical, and piezoelectric properties are given in the Appendix I. Because the film was already poled and cut in a square shape of 100 mm by 100 mm dimensions by the manufacturer, no further poling or cutting was required. After performing the micro-fabrication and photolithography procedures on the PVDF film, the finished sensor assembly was clamped between two plexiglass plates into each of which a circular hole was drilled all the way throughout their thicknesses. This way a constrained circular membrane was obtained.

The micro-fabrication and photolithography processes are detailed below in a number of steps.

5.1.1. Overview of the photolithography process

The photolithography process involves seven steps:

- Surface Preparation
- Coating (Spin Coating)
- Pre-Baking (Soft Baking)
- Mask Alignment and Exposure
- Photo resist Removal
- Post-Baking (Hard Baking)
- Etching

Surface Preparation

In this process the PVDF film is glued onto a big silicon wafer (with a radius of 45 mm) using the photo resist (PR). A bare silicon wafer was first cleaned by using both Acetone and deionized water and the photo resist was spin coated on it. The spinning rate was close to 3000 rpm, and the rotation time was 30 seconds. Then, the pre-cut 100 mm square PVDF film was placed over the Silicone wafer and pressed such that the PVDF film became glued to the Silicone wafer substrate. In order to glue the film uniformly, a roller was used to remove the wrinkles and warps as much as possible. Then, the Silicone substrate along with the PVDF was soft baked for 30 seconds at 70°C on a hot plate. This ensured adhesion of the PVDF film to the Silicon substrate.

Spin Coating

The Silicon wafer, together with the PVDF film was held on a spinner chuck by vacuum. Then, the photo resist was dropped onto the surface of the PVDF film. To create a photo resist coating of uniform thickness on the PVDF film, the film and the Silicon wafer were spun. Typically, the spinning rate was in the range of 3000 to 6000 rpm, and the spinning period was 15 to 30 seconds. Usually, the Shipley S1818 photo resist is used in such applications. However, in this research, which was conducted in the micro-fabrication laboratory of Ecole Polytechnic, the Shipley S1813 photo resist was used instead. The thickness of the photo resist is determined primarily by its viscosity and by the spinning rate of the spinner.

Pre-Baking (Soft Baking)

The main object of soft baking is to evaporate the coating solvent and to make the photo resist denser after spin coating. Typical thermal cycles are:

- 40 minutes at 50°C in an oven
- 45 seconds somewhere between 75° to 85°C on a hot plate

In this research, the soft baking was done at 65°C for one minute. Thereafter, the mask was aligned and the film was exposed to the ultra violet rays as explained in the next section.

Mask Alignment and Exposure

The design layout is illustrated in Figure 5.1 which shows one layer of mask on each side of the film. The rectangular areas in solid lines were formed on one side of the film and those areas confined by the dashed lines were formed on the other and overlap as shown. Initially, both of the masks were drawn using AutoCAD; then, they were transferred onto two separate transparent sheets using positive or light-field masks upon which the areas of electrodes were marked as dark areas. When positive or light-field masks are exposed to ultraviolet light, rays pass only through the light areas. This results in polymerization of the exposed areas and helps remove them later during the etching processes. The overlap of each set of solid and dashed areas creates a 3 mm by 3 mm square which is the desired electrode. Because the ultraviolet equipment was unable to expose both sides of the film at the same time, the exposure was done one side at a time.

As for the alignment, the masks were designed and fabricated to have outer dimensions of 120 mm by 120 mm. This is because at the time of design, the biaxial, 25μm thick PVDF films available from the GoodFellow Company had the same size. Because the dimensions of the masks and the PVDF film were identical, alignment was supposed to be done with the help of edges. Therefore, there was no need to put any alignment marks on the masks. However, when the PVDF films were ordered, their size was reduced to 100 mm by 100 mm. Consequently, the masks were cut down to the same sizes and aligned with the PVDF film. The exposure time was approximately 7 seconds.

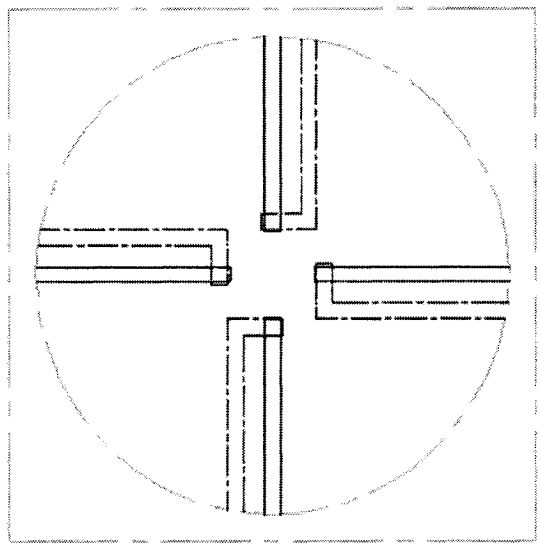

Figure 5.1 -- Mask layout for patterning

Photo resist Removal

In this procedure, the exposed film, along with its Silicon wafer substrate, was immersed in a developer solution. As a result, the polymerized photo resist areas (the areas through which the ultraviolet rays had passed) were removed. Afterwards, the film was rinsed in the deionized water and dried up.

Post Baking

Post baking removes any remaining traces of the coating solvent or developer. This step is necessary in order to harden the photo resist and improve its adhesion to the Silicone substrate. Post baking introduces stresses into the photo resist which may cause it to shrink and, if undertaken for a prolonged period or at elevated temperatures, makes

removal of photo resist considerably more difficult. Post baking is usually done at a temperature of 115°C but for PVDF it is done at 50°C for 30 to 40 minutes in an oven or at 70°C for about one minute on a hot plate. It is important to note that PVDF typically loses some of its piezoelectric and pyroelectric properties at temperatures exceeding 70°C so this is normally considered as the maximum temperature limit. This is of crucial importance when selecting the soft baking and post baking temperatures.

Etching

Once the photo resist is removed, the PVDF sample can be dipped in a commercial aluminum etchant, such as Transene Aluminum etchant A, which etches the aluminum on the PVDF film isotropically without affecting the PVDF. This etchant is comprised of different acids such as Phosphoric acid (%80), Nitric acid (%5), Chloric acid (%5) and water (%10). In order to prevent etching of the area on the other side of the PVDF film, confined between its outer edges and the Silicon wafer, the area was covered with adhesive tapes. As a result, the etching of the aluminum coatings on the back of the PVDF film was prevented. The etching was done at the room temperature. The PVDF film was dipped into the Aluminum etchant and left for about three to four minutes. Finally, the sample was removed from the etchant, rinsed first in acetone, then in deionized water, and dried using Nitrogen gas.

Note: All the above steps were repeated in the same order to create a pattern on the other side of the PVDF film.

5.2. Experimental Setup

The schematic diagram of the experimental measurement setup, developed to analyze the performance of the sensor, is shown in Figure 5.2.

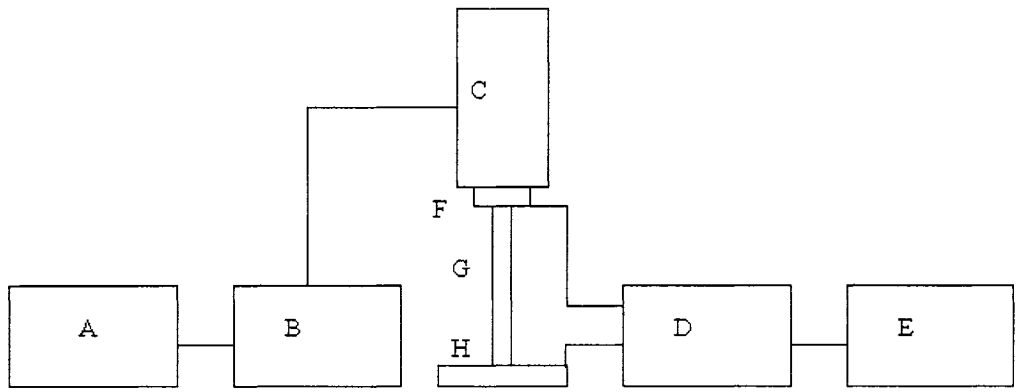

Figure 5.2 -- Experimental Set-up

The components of the setup in the above figure are:

A-Power Amplifier	E- Computer
B- Signal Generator	F-Force Transducer
C-Vibrator	G-Probe
D- A/D Converter	H-Sensor

The probe was driven by a vibration unit (Ling dynamic model V203) that generated a sinusoidal force having a magnitude of 1 N and an excitation frequency of 20 Hz which was transferred to the sensor assembly through the probe. The vibration unit was activated by a signal generator (Agilent 33220A model). The magnitude of the applied force was measured using a force transducer (Kistler, Type 9712B50 model), inserted between the probe and the vibration unit. The generated charges by all of the four sensing elements were measured and monitored on the computer by LabVIEW 7.0 software. The

output of each sensing element was displayed on a separate channel. Hence there were a total of four channels for monitoring the generated charges and an extra channel for monitoring the variation of the applied force. The force transducer ratio was $1\frac{V}{lbf}$ or $225\frac{mV}{N}$.

In keeping with Finite Element simulations two probes were used throughout the experiments. These were respectively an equilateral triangle with a side of 7 mm and a rectangular probe with dimensions of 14 mm by 7 mm. A dynamic sinusoidal load was applied to test each sensor. The peak to peak voltages, output charges and frequency value from all of the four channels were captured by the data acquisition and interface system, as will be detailed in the following section. A list of all the equipment and their specifications, used for running the experiments, is provided in Appendix 4. The layout and dimensions were already discussed in the previous sections. The fabricated assembly is shown in Figure 5.3.

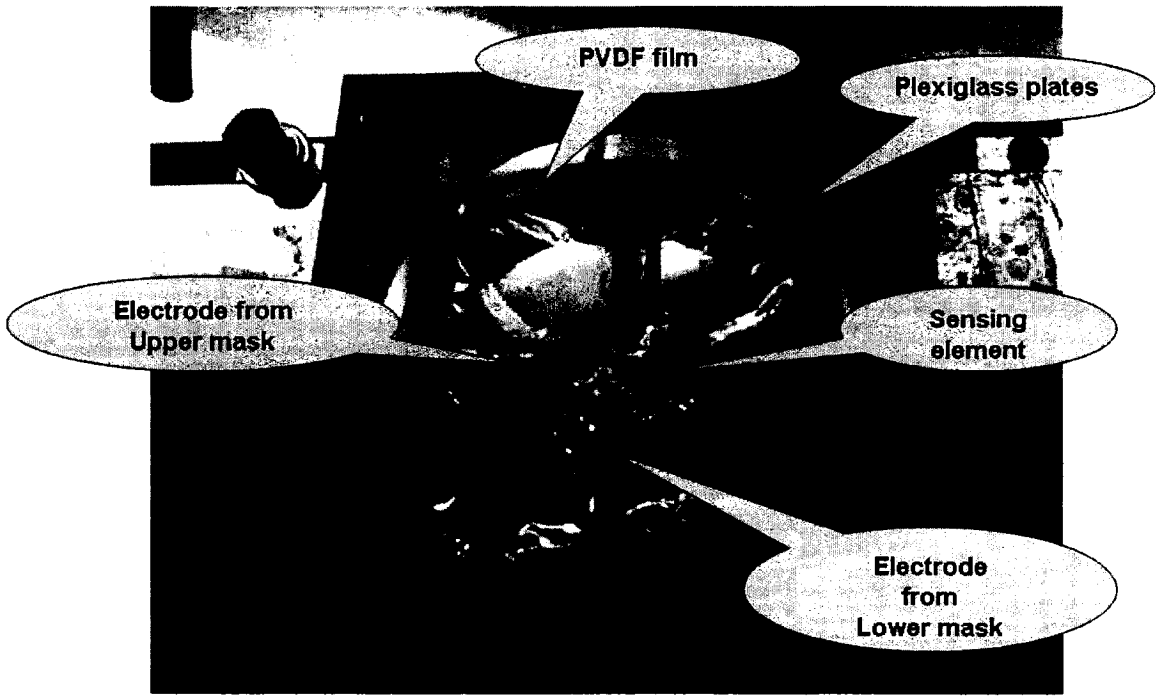

Figure 5.3 -- Plan view of the tactile sensor to be tested

The complete experimental set up with all the electronic components and the display unit is shown in the Figure 5.4. The equivalent electrical circuit of the PVDF film, and its connected experimental setup, is described in the Appendix 5.

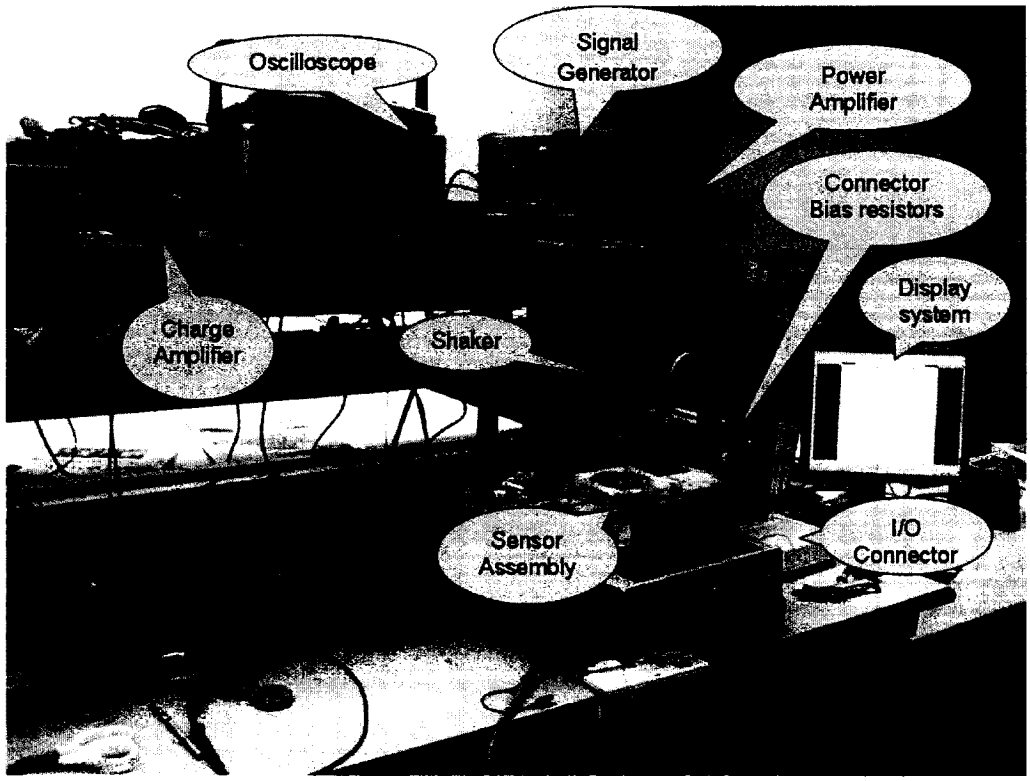

Figure 5.4 – Photograph of the complete setup

The tactile sensor is placed under the Aluminum probe. A dynamic sinusoidal force was applied by the shaker which was activated by the power amplifier and the signal generator. The output from the sensor was fed to the connector box via the bias resistors. The data was then transferred to the data acquisition card inside the computer. The block diagram of the data acquisition system is shown in Figure 5.5.

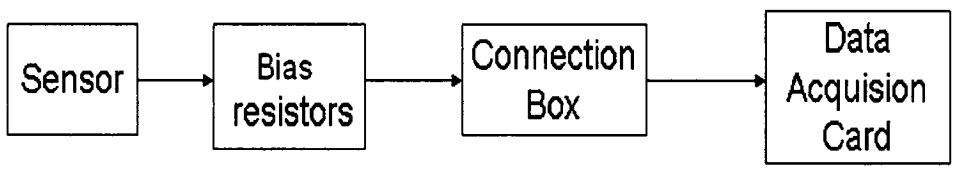

Figure 5.5 — Block diagram of the Data Acquisition System

5.3. Tests and Results

Using the described setup, tests were conducted with probes of different shapes, sizes and orientations. A signal generator stimulated the vibration unit to enable the probe to apply a sinusoidal force to the sensor. Using the voltage to force ratio of the force transducer, $1\frac{V}{Ibf}$ or $0.225\frac{V}{N}$, a sinusoidal force was applied with a magnitude of 1 N and at a frequency of 20 Hz. Throughout the entire tests, contrary to the ANSYS simulations, the magnitude of force was kept at 1 N and the frequency stayed at a constant value of 20 Hz. The main reasons behind selecting these values were that for smaller magnitudes of force and frequency, the output charges did not show smooth and noiseless variation. Particularly for frequencies below 10 Hz, it was too hard to distinguish between the actual response of each sensing element and the existing noise. The same thing applied to forces with magnitudes smaller than 1 N. On the other hand, as the magnitude and frequency of the force rapidly increased, the risks of damaging the thin film and making holes in it, as well as buckling the shaker probe, increased noticeably. All of these facts contributed to choosing the above values as optimum selections without deviating from them.

5.3.1. Results of displacing a triangular probe

An equilateral triangular probe of 7 mm on each side was first selected to exert a sinusoidal load to the membrane. In Figure 5.6, the obtained data corresponding to three different angles, 35°, 65°, and 90°, are shown by markers.

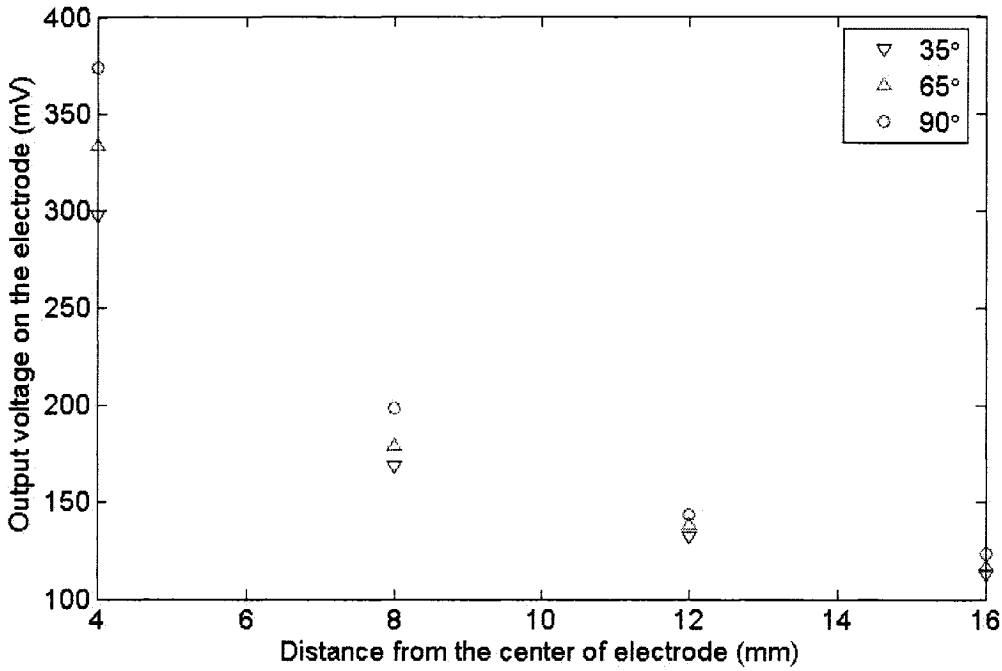

Figure 5.6 – Three sets of charge versus distance data for an electrode using a triangular probe

Putting the data for all angles resulted in a crowded figure, in which it was not possible to distinguish between different sets of data. The following curves in Figure 5.7 show typical voltage versus distance variations for an electrode for more angles.

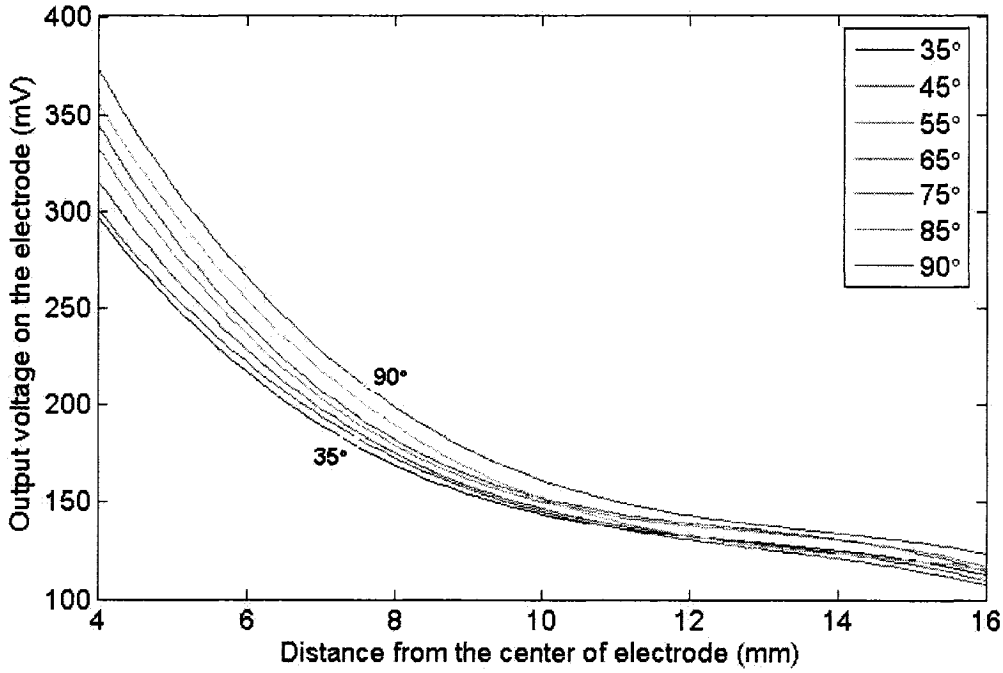

Figure 5.7 -- Typical charge versus distance variation for an electrode using a triangular probe

The mapping scheme adopted for performing the tests was the same as that chosen in chapter 3, which was depicted in figures 3.4 and 3.6. The word "typical" here has been repeated several times to emphasize that not all electrodes follow exactly the same trend. Although the PVDF film is a biaxial film and therefore, it is expected that all the electrodes must demonstrate precisely the same behaviour, the experimental errors as well as fabrication problems are all combined together and lead to different responses. Figure 5.7 depicts the average of the obtained curves for all the four sensing elements and that is why it is called "typical".

By taking a look at Figure 5.7, it is recognized that the system behaviour remains close to what was obtained by Finite Element simulations and is therefore a positive finding. Although the above set of curves depict the variations of "voltage" versus distance, instead of "charge" versus distance, they can still be used for studying the behaviour of

the system. Voltages are related to charges by a coefficient which is obviously the capacitance of the sensing element. If consistency is observed for all the four sensing elements, it makes no difference as to which parameter to choose, voltage or charge. Since during the experiments the results on the computer were voltages, and in order to provide a clearer view of how the system behaved during the runs, the decision was made to select voltages.

Some sample triangulations and their results are presented afterwards. In the first test, as shown in Figure 5.8, the probe was put at 16 mm and 75° with respect to the center of electrode D.

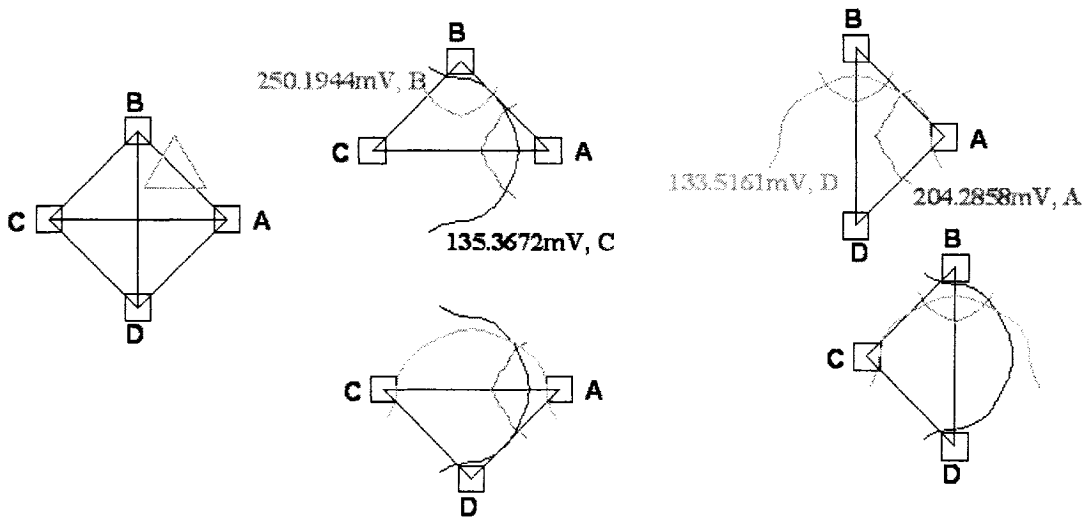

Figure 5.8 – First set of isocharge contours obtained from experiments

The positioning error is 0.372 mm which is acceptable.

In the second test, the probe was put at 8 mm and 135° with respect to the center of electrode D and rotated 90° counterclockwise. This is shown in Figure 5.9.

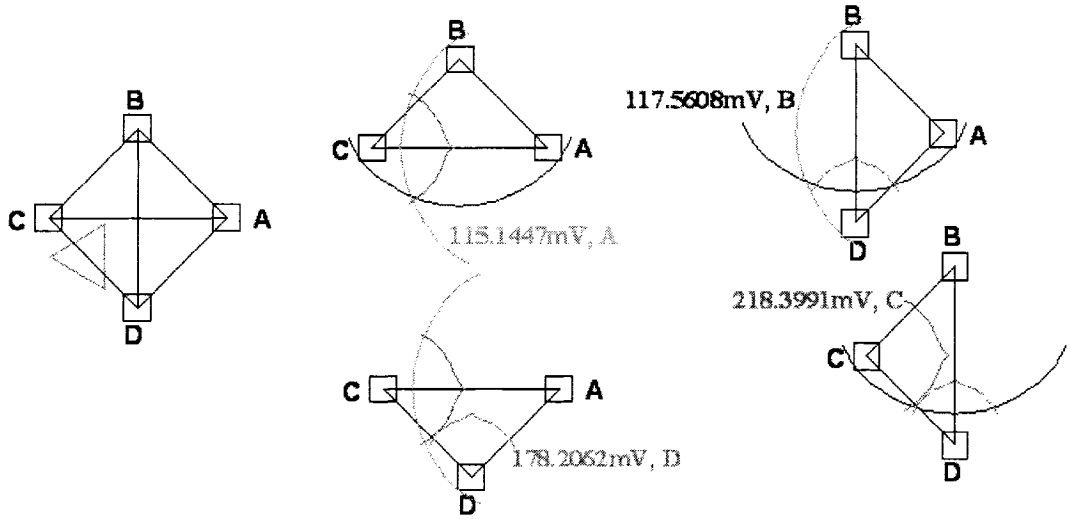

Figure 5.9 -- Second set of experimental isocharge contours

The positioning error was calculated to be 1.411 mm. Although greater than 1 mm, it is still acceptable.

The results for the previous two tests and three more are summarized in Table 5.1.

Table 5.1 — Summary of experimental positioning results for a triangular probe

Position of the probe centroid	Positioning error for the three electrode sensor (mm)
8 mm, 65° (with respect to the center of lower-most electrode)	2.23
16 mm, 75° (with respect to the center of lower-most electrode)	0.372
8 mm, 135° (with respect to the center of lower-most electrode), probe rotated 90° CCW	1.411
12 mm, 105° (with respect to the center of lower-most electrode), probe inverted	1.89
Probe at the center, rotated 90° CW	0.521

There are a few cases in which the positioning error surpasses 1 mm. These are in contrast to theoretical results in which all the errors were less than 1 mm. There are a number of factors which compromised experimental results and these are detailed in section 5.4.

5.3.2. Results of displacing a rectangular probe

To conform to the theoretical approach, a rectangular probe of 14 mm by 7 mm dimensions was selected as the next probe for applying a sinusoidal force to the membrane. In Figure 5.10, the obtained data corresponding to three different angles, 35°, 65°, and 90°, are shown by markers.

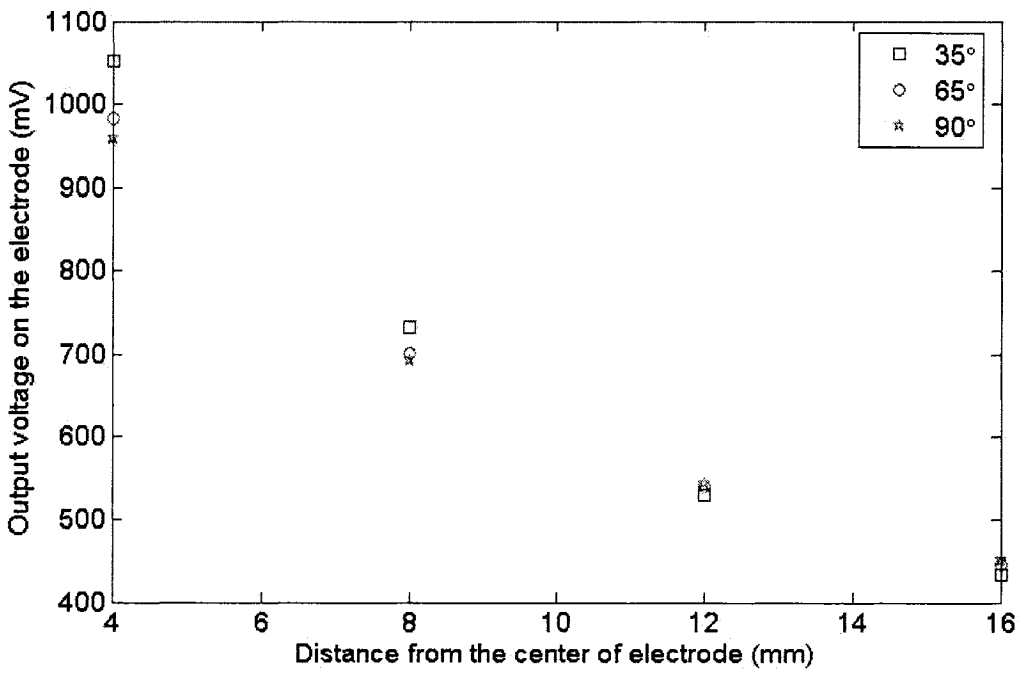

Figure 5.10 – Three sets of charge versus distance data for an electrode using a rectangular probe

Similar to the triangular probe, since putting the data for all angles resulted in a crowded figure, only three sets of data were displayed in the previous figure. The following curves show typical voltage versus distance variations for an electrode.

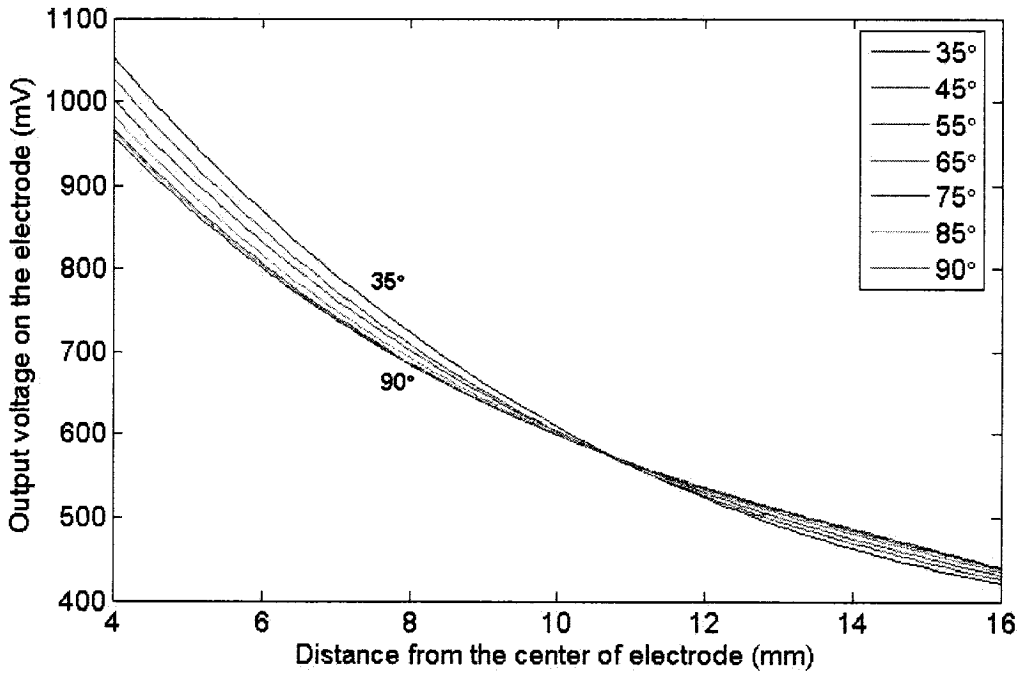

Figure 5.11 -- Typical charge versus distance variation for an electrode using a rectangular probe

Discussions on the logic behind choosing voltages as outputs, and why the term "typical" has been used are similar to those already presented in the preceding section. Therefore, they will not be repeated here. Once again, it is good to see that the system behavior remains close to what was obtained by Finite Element simulations.

A number of tests were performed, this time with the rectangular probe. In the first experiment, as shown in Figure 5.12, the probe was put at 16 mm and 75° with respect to the center of electrode D.

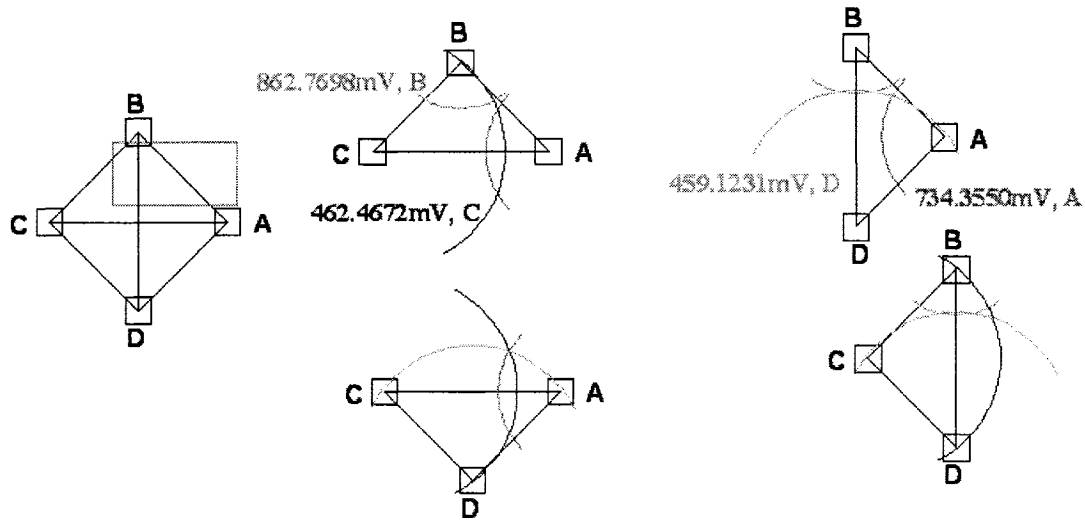

Figure 5.12 – Results of first test with a rectangular probe

The positioning error is 0.764 mm which is acceptable.

In the second test with a rectangular probe, the probe was put at 8 mm and 135° with respect to the center of electrode D and rotated 90° counterclockwise.

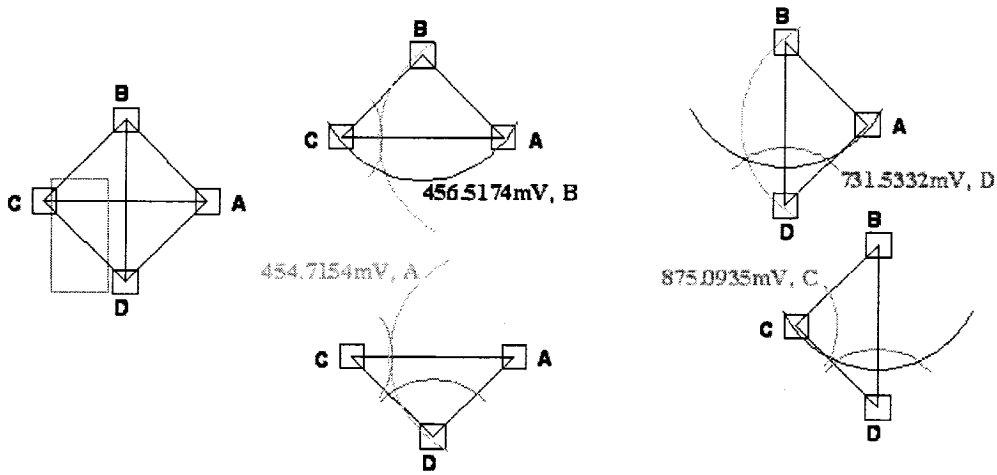

Figure 5.13 -- Results of second test with a rectangular probe

The positioning error was calculated to be 0.792 mm which falls below 1 mm and is acceptable.

The results for the previous two tests and three more are summarized in Table 5.2.

Table 5.2 — Summary of experimental positioning results for a rectangular probe

Position of the probe centroid	Positioning error for the three electrode sensor (mm)
8 mm, 65° (with respect to the center of lower-most electrode)	1.325
16 mm, 75° (with respect to the center of lower-most electrode)	0.764
8 mm, 135° (with respect to the center of lower-most electrode), probe rotated 90° CCW	0.792
12 mm, 105° (with respect to the center of lower-most electrode), probe rotated 45° CW	0.924
Probe at the center, rotated 90° CW	No intersection of contours

There is one case in which the positioning error exceeds 1 mm, in contrast to theoretical results in which all the errors were less than 1 mm. In another case, when the probe is at the center of the membrane and rotated 90°, the centroid cannot be located. The reasons behind the experimental results are detailed in section 6.1.

5.4. Summary

In this chapter, first the fabrication of the sensor by photolithography techniques was discussed. The fabrication procedure was broken down into different steps which were detailed later. This was followed by an explanation of the test setup required for running the tests. The performed tests, along with their results, were given in the following section. On average, there was about 15% discrepancy between the theoretical and

experimental positioning results. The reasons behind the errors are described in section 6.1, discussions. These are coupled by justification of the obtained experimental isocharge contours, the motivation behind choosing a sinusoidal load with certain frequency (20 Hz) and magnitude of applied force (1 N), and comparibility of the results of static (theoretical) and dynamic (experimental) loading of the sensor.

Chapter 6 – Discussions, conclusions and future works

This chapter is devoted to the discussions, conclusions and suggests some future works.

6.1. Discussions

1) In general, piezoelectric materials such as PVDF have a transient response to static loads and/or deflections. Any generated charge and/or deformation to an external stimulation of a PVDF material lasts for a very short time, sometimes even as short as a fraction of a second. This makes measuring and recording their output very difficult and challenging. When a piezoelectric material is connected to an electrical circuit for measuring its output charge, the measurement problem intensifies because of the introduction of other devices and the way they can affect the RC time-constant of the circuit. Hence, in order to facilitate measuring and recording a PVDF output charge, it is more convenient if the applied force is harmonic in nature, especially sinusoidal.

2) The PVDF film used in the experiments is extremely thin (25 microns) and is therefore an extremely lightweight piece of material. Its mass is calculated as:

$$m = (100\,\text{mm} \times 100\,\text{mm})(25\,\mu\text{m})(1760\,\frac{\text{kg}}{\text{m}^3}) = 0.44\,\text{grams}$$

However, since it is only the circular area which is of interest in this study, the mass is even lower with a value of 0.28 grams. In equations of vibrations or dynamic relations, the mass of an object plays a very important role in its dynamical behavior. The smaller the mass is, the more negligible its effect becomes.

3) Another parameter which is prominently raised during dynamic response of a system is its damping ratio. For the tests in this study, because the PVDF film was vibrating in the air and was never confronted with any other source of friction and damping except that of the air itself, the damping ratio could be plausibly ignored.

4) With tiny values of mass and damping ratio, it makes sense to assume that there is not a significant gap between the static and dynamic responses of such a thin PVDF film. It is safe to rely on the experimental data and formulate conclusions on those grounds.

5) It is sufficiently justifiable to say that, in practice, when an object touches a sensor, the nature of force seldom becomes harmonic, or more specifically, sinusoidal. However, some recent studies suggest that during contact and removal of an object from a sensor, the force profile can be accurately estimated with a sinusoidal curve. This further validates the selection of a sinusoidal load and its relevant results.

6) A modal analysis of the pre-stressed membrane indicates that the first natural frequency of the PVDF film under the assigned initial conditions is 117 Hz. This puts the excitation frequency of 20 Hz at one sixth of the first natural frequency. Thus the loading condition can be considered as a quasi-static one which means that the results should not deviate significantly from the static numbers.

7) What primarily matters, though, is the behaviour of the system or the way output charges vary with respect to the position of the probe. Whether the load is static or dynamic does not make such a big difference in these investigations. If the force is sinusoidal, the peak values of system response will be chosen and studied. If these peak values show the same trend as those obtained from a static analysis, then the main objectives are met. The whole system can be calibrated and the dynamic and static results are related to each other by a calibration factor or a coefficient.

8) In ANSYS simulations, a uniform temperature was induced by first defining a thermal expansion coefficient at 25°C and then, applying a uniform temperature of 24°C for the entire membrane area. However, the same thing could not be done in practice. Numerous attempts were made in order to do the same thing by first setting the temperature of a hot plate at an elevated temperature, even up to 40°C, exposing the PVDF film to the generated heat, and finally removing the film from the hot plate area, and exposing it to the ambient temperature. As previously mentioned, the PVDF film was clamped between the two plexiglass plates as previously detailed yet all of the efforts had to be aborted because the desired uniform pretension was not achieved. A non-uniform pretension evidently results in the development and presence of a number of wrinkles on the membrane surface. These wrinkles can affect the mechanical behavior of the membrane in terms of developed strains and/or stresses which transforms into unexpected amounts for output electrical charges on electrodes. Some papers have addressed analysis of membranes with wrinkles but the methods involved are complicated and difficult to put into practice.

9) The PVDF film was modeled as a circular membrane with uniform thickness of 25 μm. Then, the stresses developed along the edges of electrodes were retrieved, plugged into piezoelectric formula, and converted into electrical charges. For an experimental run, however, the output charges should be retrieved by gluing copper tapes on the electroded areas. As shown in Figure 5.3, for measuring the output electrical charge of each electrode, two copper tapes should be glued to the PVDF film, one on each side. In order to maintain the adhesion between the copper tapes and the PVDF surface, adhesive tapes were used. Wires were soldered to each of the copper tapes and connected to other terminals in order to record and measure the developed charges. Considering all of the above factors, it is justifiable to conclude that this system has a very different behaviour than that of an ideal, uniform PVDF film. Because of the added stiffness, especially since the copper and adhesive tapes have a thickness of at least 50 microns each, this makes it twice as thick as that of the PVDF membrane itself. Therefore, the thicknesses of the system, and consequently its stiffness, increase abruptly and drastically near the metallized electrode areas. Moreover, these tapes and the solders add to the entire mass of the system. Bearing in mind that the mass of the membrane is only 0.28 grams, the added masses could equal or even surpass that. All these factors could well account for the differences in results.

10) The next thing to consider is the sensor fabrication problems which was a big challenge because of its scales and dimensions. Although the facilities and equipment in Ecole Polytechnic's micro-fabrication lab were quite adequate, the author and his technical assistant had, nonetheless, to make several trials and errors in order to

achieve the appropriate parameters involved. Eventually, although not flawless, the fabricated sensor was close enough to the desired pattern. As examples of fabrication errors, the inequality of capacitances of the four sensing elements should be mentioned. Based on the theoretical calculations, the capacitance of each sensing element should be:

$$C = \varepsilon_0 \varepsilon_r \frac{A}{d} = (8.854\times10^{-12}\,\frac{C}{m})(11)\frac{(9\times10^{-6})\,m^2}{(25\times10^{-6})\,m} = 35.062\times10^{-12}\ F \approx 35\,pF$$

However, measuring the capacitance of electrodes using an LCR meter showed a disparity between the theoretical and actual capacitances. As an example, two of the four sensing elements had a capacitance of 23 pF which is 37% lower than what it should have been. This can be attributed to the photoresist remaining in between or over the metallized areas of the PVDF film.

11) Two other sources of error could be attributed to incorrect positioning. These could occur when attempting to locate the probe at the right point and when positioning the whole PVDF film between the plexiglass plates. In the first instance, the error could be as large as 1 mm and even larger in the second instance.

12) Another important point to bring up here is the inaccuracy of the shaker system. The shaker assembly does not have a closed-loop feedback system and hence, the force applied by it fluctuates around the preset value. This fluctuation, although small, can induce minor undesired alterations in output charges.

13) The electrical circuit to which the PVDF film and its sensing elements are connected can also play a key role. Therefore, special provisions and considerations should be made in order to obtain plausible results. The equivalent resistance of the circuit

should be kept as low as possible so that the voltage drop is kept to a minimum. Further descriptions are provided in the Appendix 5.

14) As stated at the end of section 5.3.1., the most important point to take into consideration, and the goal of this research, is determining the general trend of charge versus the magnitude and position of the applied force. If the trend remains the same, no matter how big the output charges or voltages are, then the main target of the research is attained.

15) Another thing to consider is the effect of pyroelectric effect. When a foreign object or probe comes into contact with the electrode area of a PVDF film, a sudden change of temperature can occur which leads into a secondary source of charge generation. At times this effect can be noticeably large and dominate the outputs of other sources like stresses. Throughout the simulations, it was assumed that even if the probe did touch an electrode area, no temperature alteration would occur so actually the pyroelectric effect was ignored.

6.2. Conclusions

1) Objectively, when it comes to detecting forces which are applied via non-circular probes, a four-electrode biaxial sensor is the right expediency.

2) On a positive note, for forces with magnitudes other than 1 N, at least in the band with an upper limit of 2 N, the triangulation method always works for detecting the position of the applied force

3) Output electrical charges of the sensor vary linearly against the magnitude of the applied force up to 0.5 N. For magnitudes of forces above this value, although the charge vs. force variation becomes nonlinear, it is possible to approximate the magnitude of the applied force by referring to the figures and equations given in the section 3.4.1.
4) When using a uniaxial film, either with three- or four- electrodes, the system is not effective and reliable enough for detecting centroids of objects or positions of the applied forces when the exerted force is not a concentrated force, or when the shape of the probe is non-circular.
5) Increasing the thickness of the film has a less than desired effect on the linearity of the system. Moreover, it introduces a third source for generation of electrical charge, along the 3- or thickness direction of PVDF film, which adds complexity and further jeopardizes the linearity of the system.

6.3. Future Works

1) One important factor to consider for future works is the pyroelectric response of the PVDF film. In practice, when an object like a tissue touches the PVDF film, it does not necessarily have the same temperature as that of the PVDF film and its sensing elements. This temperature differential can result in abrupt and noticeable outputs from the sensor.

2) Another point to work on for the future is enabling the sensor to detect the shear stress components. With its current configuration, it is not for certain whether the sensor can detect any such component or not. As an example, it is not known clearly whether it can distinguish between a normally applied force of 1 N and another force having a magnitude of 2 N, when exerted at an angle of 30° to the surface of the PVDF film.

3) Design parameters of the sensor can be changed in order to investigate their effects on the performance of the sensor. Distance between the centers of the each pair of opposing sensing elements (such as elements A and C), dimensions of each sensing element, locations and orientations of each sensing element with respect to drawn and transverse directions, and other shapes for sensing elements such as circle, are examples of design parameters which could be investigated upon.

Appendix 1 - Properties of PVDF film manufactured by the GoodFellow company

Chemical Resistance

Acids - concentrated	Good
Acids - dilute	Good
Alcohols	Good
Alkalis	Fair
Aromatic hydrocarbons	Good
Greases and Oils	Good
Halogenated Hydrocarbons	Good-Fair
Halogens	Good-Poor

Electrical Properties

Dielectric constant @1MHz	8.4
Dielectric strength (kV mm^{-1})	13
Dissipation factor @ 1kHz	0.06
Surface resistivity (Ohm/sq)	10^{13}
Volume resistivity (Ohmcm)	10^{14}

Mechanical Properties

Abrasive resistance - ASTM D1044 (mg/1000 cycles)	24
Coefficient of friction	0.2-0.4
Elongation at break (%)	50
Hardness - Rockwell	R77-83
Izod impact strength (J m^{-1})	120-320
Poisson's ratio	0.34
Tensile modulus (GPa)	1.0-3.0
Tensile strength (MPa)	25-60

Physical Properties

Density (g cm^{-3})	1.76
Flammability	V0
Limiting oxygen index (%)	44
Radiation resistance	Fair
Refractive index	1.42
Resistance to Ultra-violet	Excellent
Water absorption - over 24 hours (%)	0.04

Thermal Properties

Coefficient of thermal expansion ($x10^{-6}$ K^{-1})	80-140
Heat-deflection temperature - 0.45MPa (C)	120-150
Heat-deflection temperature - 1.8MPa (C)	80-115
Lower working temperature (C)	-40
Thermal conductivity (W m^{-1} K^{-1})	0.1-0.25 @ 23C
Upper working temperature (C)	135-150

Properties Polyvinylidenefluoride Film

Property		Value		
Material		Uni-axial	Bi-axial	Unoriented
Dielectric Constant @ 1MHz		12 @ 1KHz	11 @ 1KHz	
Dielectric Strength @25μm thick	kV mm^{-1}	approx. 160		
Dissipation Factor @1MHz		0.018 @ 1KHz		
Extension to break - Longitudinal	%	14-20	50	
Extension to break - Transverse	%	300-450	50	
Heat-sealing Temperature	C			204-218
Permeability to Carbon Dioxide @25C	$x10^{-13}$ cm^3. cm cm^{-2} s^{-1} Pa^{-1}			0.2
Permeability to Hydrogen @0C	$x10^{-13}$ cm^3. cm cm^{-2} s^{-1} Pa^{-1}			0.25
Permeability to Hydrogen @25C	$x10^{-13}$ cm^3. cm cm^{-2} s^{-1} Pa^{-1}	0.25		
Permeability to Nitrogen @25C	$x10^{-13}$ cm^3. cm cm^{-2} s^{-1} Pa^{-1}			0.03
Permeability to Oxygen @25C	$x10^{-13}$ cm^3. cm cm^{-2} s^{-1} Pa^{-1}			0.03
Permeability to Water @38C	$x10^{-13}$ cm^3. cm cm^{-2} s^{-1} Pa^{-1}			250
Piezo coefficient - d31	$pC.N^{-1}$	18-20	8	
Piezo coefficient - d32	$pC.N^{-1}$	2	8	
Piezo coefficient - d33	$pC.N^{-1}$	approx. -20	15-16	
Piezo coefficient - d3h	$pC.N^{-1}$	-6.5		
Piezo coefficient - g31	$Vm.N^{-1}$	0.15		
Piezo coefficient - g32	$Vm.N^{-1}$	0.015		
Piezo coefficient - g33	$Vm.N^{-1}$	approx. -0.15	approx. 0.18	
Pyro coefficient - 3	μC m^{-2} K^{-1}	-27	approx. 25	
Shrinkage	%	2.5-25	2	
Tensile modulus - Longitudinal	GPa	1.8-2.7	2	
Tensile modulus - Transverse	GPa	1.7-2.7	2	
Tensile strength - Longitudinal	MPa	180-290	180	
Tensile strength - Transverse	MPa	29-38	180	
Volume Resistivity	Ohmcm	$1.8x10^{15}$	$5x10^{14}$	

Appendix 2 - List of messages appeared in ANSYS during meshing trials with piezoelectric elements

Radius of 30mm, thickness of 25 microns, Solid 227 element, element size 12.5 microns:

Maximum number of elements was surpassed. Meshing aborted.

Radius of 20mm, thickness of 25 microns, Solid 227 element, element size 12.5 microns:

Maximum number of elements was surpassed. Meshing aborted.

Radius of 10mm, thickness of 25 microns, Solid 227 element, element size 12.5 microns:

After a long time, meshing stopped. Then the same old message: "Maximum number of elements was surpassed." popped up. Meshing aborted again.

Radius of 10mm, thickness of 40 microns, Solid 227 element, element size 12.5 microns:

After a long time, meshing was halted. Then the same old message: "Maximum number of elements was surpassed." popped up. Meshing aborted again.

Radius of 10mm, thickness of 40 microns, Solid 227 element, element size 10 microns:

After a long time, meshing stopped. Then the same old message: "Maximum number of elements was surpassed." popped up. Meshing aborted again.

Radius of 10mm, thickness of 110 microns, Solid 227 element, element size 55 microns:

After a long time, meshing stopped. Then the same old message: "Maximum number of elements was surpassed." popped up. Meshing aborted again.

Radius of 10mm, thickness of 110 microns, Solid 227 element, element size 27.5 microns:

After a long time, meshing ended. Then the same old message: "Maximum number of elements was surpassed." popped up. Meshing aborted again.

Radius of 10mm, thickness of 110 microns, Solid 226 element, element size 27.5 microns:

After a long time, meshing stopped. Then the same old message: "Maximum number of elements was surpassed." popped up. Meshing aborted again.

Radius of 10mm, thickness of 110 microns, Solid 226 element, element size 55 microns:

After a long time, meshing was left incomplete. Then the same old message: "Maximum number of elements was surpassed." popped up. Meshing aborted again.

Radius of 10mm, thickness of 110 microns, Solid 226 element, element size 27.5 microns:

After a long time, meshing terminated. Then the same old message: "Maximum number of elements was surpassed." popped up. Meshing aborted again.

Radius of 10mm, thickness of 110 microns, Solid 226 element, element size 10 microns:

After a long time, meshing stopped. Then the same old message: "Maximum number of elements was surpassed." popped up. Meshing aborted again.

Radius of 10mm, thickness of 110 microns, Solid 226 element, element size 5 microns:

After a long time, meshing was halted. Then the same old message: "Maximum number of elements was surpassed." popped up. Meshing aborted again.

Radius of 10mm, thickness of 110 microns, Solid 98 element, element size 55 microns:

After a long time, meshing was finished. Then the same old message: "Maximum number of elements was surpassed." popped up. Meshing aborted again.

Radius of 10mm, thickness of 110 microns, Solid 98 element, element size 55 microns:

After a long time, meshing ended up abruptly. Then the same old message: "Maximum number of elements was surpassed." popped up. Meshing aborted again.

Radius of 10mm, thickness of 110 microns, Solid 98 element

Meshing was done but there were 6 shape violations out of 4067 elements. An attempt to refine the meshing failed.

Radius of 10mm, thickness of 110 microns, Solid 227 element

Meshing was done but there were 1616 shape violations out of 4067 elements. An attempt to refine the meshing failed.

Radius of 10mm, thickness of 110 microns, Solid 226 element

Meshing was done but there were 1430 shape violations out of 4067 elements. An attempt to refine the meshing failed.

Appendix 3 - Code for obtaining the output electrical charges on the sensing elements

```
/CLEAR,NOSTART
/COM,ANSYS RELEASE 9.0   UP20041104     17:18:38   10/29/2006
/PREP7
FLST,3,1,8
FITEM,3, 9.1569E-03, -6.3639E-03,0
K, ,P51X
FLST,3,1,8
FITEM,3, 5.6569E-03, -0.3017E-03,0
K, ,P51X
FLST,3,1,8
FITEM,3, 2.1569E-03, -6.3639E-03,0
K, ,P51X
LSTR,     1,     2
LSTR,     2,     3
LSTR,     3,     1
FLST,2,3,4
FITEM,2,3
FITEM,2,1
FITEM,2,2
AL,P51X
/PLOPTS,INFO,3
/PLOPTS,LEG1,1
/PLOPTS,LEG2,1
/PLOPTS,LEG3,1
/PLOPTS,FRAME,0
/PLOPTS,TITLE,1
/PLOPTS,MINM,1
/PLOPTS,FILE,0
/PLOPTS,LOGO,1
/PLOPTS,WINS,1
/PLOPTS,WP,0
/PLOPTS,DATE,0
/TRIAD,ORIG
/REPLOT
!*
CYL4,0,0,45e-3
BLC5,10e-3,0,3e-3,3e-3
BLC5,0,10e-3,3e-3,3e-3
BLC5,-10e-3,0,3e-3,3e-3
BLC5,0,-10e-3,3e-3,3e-3
```

```
FLST,2,6,5,ORDE,2
FITEM,2,1
FITEM,2,-6
AOVLAP,P51X
FLST,2,6,5,ORDE,3
FITEM,2,1
FITEM,2,3
FITEM,2,-7
AGLUE,P51X
!*
ET,1,SHELL63
!*
KEYOPT,1,1,1
KEYOPT,1,2,0
KEYOPT,1,3,0
KEYOPT,1,5,0
KEYOPT,1,6,0
KEYOPT,1,7,0
KEYOPT,1,8,0
KEYOPT,1,9,0
KEYOPT,1,11,0
!*
R,1,25e-6, , , , , ,
RMORE, , , ,
RMORE
RMORE, ,
!*
!*
MPTEMP,,,,,,,,
MPTEMP,1,0
MPDATA,EX,1,,2e9
MPDATA,PRXY,1,,0.34
MPTEMP,,,,,,,,
MPTEMP,1,0
UIMP,1,REFT,,,25
MPDATA,ALPX,1,,110e-6
SAVE
FLST,2,5,5,ORDE,3
FITEM,2,1
FITEM,2,3
FITEM,2,-6
AESIZE,P51X, ,
FLST,2,1,5,ORDE,1
FITEM,2,7
AESIZE,P51X,1e-3,
MSHAPE,1,2D
```

```
MSHKEY,0
!*
FLST,5,6,5,ORDE,3
FITEM,5,1
FITEM,5,3
FITEM,5,-7
CM,_Y,AREA
ASEL, , , ,P51X
CM,_Y1,AREA
CHKMSH,'AREA'
CMSEL,S,_Y
!*
AMESH,_Y1
!*
CMDELE,_Y
CMDELE,_Y1
CMDELE,_Y2
!*
nlgeom, on
sstif, on
FINISH
/SOL
NSUBST,50,0,0
NEQIT,200
FLST,2,4,4,ORDE,2
FITEM,2,4
FITEM,2,-7
!*
/GO
DL,P51X, ,ALL,0
GPLOT
FLST,2,1,5,ORDE,1
FITEM,2,1
/GO
FLST,2,1,5,ORDE,1
FITEM,2,1
/GO
!*
SFA,P51X,1,PRES,-47130.68396
TUNIF,24,
/STATUS,SOLU
SOLVE
GPLOT
!*
/PSF,PRES,NORM,1,0,1
/PBF,DEFA, ,1
```

```
/PIC,DEFA, ,1
/PSYMB,CS,0
/PSYMB,NDIR,0
/PSYMB,ESYS,0
/PSYMB,LDIV,0
/PSYMB,LDIR,0
/PSYMB,ADIR,0
/PSYMB,ECON,0
/PSYMB,XNODE,0
/PSYMB,DOT,1
/PSYMB,PCONV,
/PSYMB,LAYR,0
/PSYMB,FBCS,0
!*
/PBC,ALL, ,0
/REP
!*
/PNUM,KP,0
/PNUM,LINE,0
/PNUM,AREA,0
/PNUM,VOLU,0
/PNUM,NODE,1
/PNUM,TABN,0
/PNUM,SVAL,0
/NUMBER,0
!*
/PNUM,ELEM,1
/REPLOT
!*
/POST1
!*
!defining the right edge of electrode A
path,reA,5,30,20
ppath,1, ,11.5e-3,1.5e-3
ppath,2, ,11.5e-3,0.75e-3
ppath,3, ,11.5e-3,0
ppath,4, ,11.5e-3,-0.75e-3
ppath,5, ,11.5e-3,-1.5e-3
pdef,sxreA,s,x
pcalc,intg,chrgreA,sxreA,s,((8*9e-6))/(3e-3)
paget,redgeA,table
!defining the left edge of electrode A
path,leA,5,30,20
ppath,1, ,8.5e-3,1.5e-3
ppath,2, ,8.5e-3,0.75e-3
ppath,3, ,8.5e-3,0
```

```
ppath,4, ,8.5e-3,-0.75e-3
ppath,5, ,8.5e-3,-1.5e-3
pdef,sxleA,s,x
pcalc,intg,chrgleA,sxleA,s,((8*9e-6))/(3e-3)
paget,ledgeA,table
!defining the upper edge of electrode A
path,ueA,5,30,20
ppath,1, ,8.5e-3,1.5e-3
ppath,2, ,9.25e-3,1.5e-3
ppath,3, ,10e-3,1.5e-3
ppath,4, ,10.75e-3,1.5e-3
ppath,5, ,11.5e-3,1.5e-3
pdef,syueA,s,y
pcalc,intg,chrgueA,syueA,s,((8*9e-6))/(3e-3)
paget,uedgeA,table
!defining the lower edge of electrode A
path,loeA,5,30,20
ppath,1, ,8.5e-3,-1.5e-3
ppath,2, ,9.25e-3,-1.5e-3
ppath,3, ,10e-3,-1.5e-3
ppath,4, ,10.75e-3,-1.5e-3
ppath,5, ,11.5e-3,-1.5e-3
pdef,syloeA,s,y
pcalc,intg,chrgloeA,syloeA,s,((8*9e-6))/(3e-3)
paget,loedgeA,table
!defining the output charge on electrode A
chargeA_=(redgeA(81,6)+ledgeA(81,6)+uedgeA(81,6)+loedgeA(81,6))/2
!defining the right edge of electrode B
path,reB,5,30,20
ppath,1, ,1.5e-3,11.5e-3
ppath,2, ,1.5e-3,10.75e-3
ppath,3, ,1.5e-3,10e-3
ppath,4, ,1.5e-3,9.25e-3
ppath,5, ,1.5e-3,8.5e-3
pdef,sxreB,s,x
pcalc,intg,chrgreB,sxreB,s,((8*9e-6))/(3e-3)
paget,redgeB,table
!defining the left edge of electrode B
path,leB,5,30,20
ppath,1, ,-1.5e-3,11.5e-3
ppath,2, ,-1.5e-3,10.75e-3
ppath,3, ,-1.5e-3,10e-3
ppath,4, ,-1.5e-3,9.25e-3
ppath,5, ,-1.5e-3,8.5e-3
pdef,sxleB,s,x
pcalc,intg,chrgleB,sxleB,s,((8*9e-6))/(3e-3)
```

```
paget,ledgeB,table
!defining the upper edge of electrode B
path,ueB,5,30,20
ppath,1, ,-1.5e-3,11.5e-3
ppath,2, ,-0.75e-3,11.5e-3
ppath,3, ,0,11.5e-3
ppath,4, ,0.75e-3,11.5e-3
ppath,5, ,1.5e-3,11.5e-3
pdef,syueB,s,y
pcalc,intg,chrgueB,syueB,s,((8*9e-6))/(3e-3)
paget,uedgeB,table
!defining the lower edge of electrode B
path,loeB,5,30,20
ppath,1, ,-1.5e-3,8.5e-3
ppath,2, ,-0.75e-3,8.5e-3
ppath,3, ,0,8.5e-3
ppath,4, ,0.75e-3,8.5e-3
ppath,5, ,1.5e-3,8.5e-3
pdef,syloeB,s,y
pcalc,intg,chrgloeB,syloeB,s,((8*9e-6))/(3e-3)
paget,loedgeB,table
!defining the output charge on electrode B
chargeB_=(redgeB(81,6)+ledgeB(81,6)+uedgeB(81,6)+loedgeB(81,6))/2
!defining the right edge of electrode C
path,reC,5,30,20
ppath,1, ,-8.5e-3,1.5e-3
ppath,2, ,-8.5e-3,0.75e-3
ppath,3, ,-8.5e-3,0
ppath,4, ,-8.5e-3,-0.75e-3
ppath,5, ,-8.5e-3,-1.5e-3
pdef,sxreC,s,x
pcalc,intg,chrgreC,sxreC,s,((8*9e-6))/(3e-3)
paget,redgeC,table
!defining the left edge of electrode C
path,leC,5,30,20
ppath,1, ,-11.5e-3,1.5e-3
ppath,2, ,-11.5e-3,0.75e-3
ppath,3, ,-11.5e-3,0
ppath,4, ,-11.5e-3,-0.75e-3
ppath,5, ,-11.5e-3,-1.5e-3
pdef,sxleC,s,x
pcalc,intg,chrgleC,sxleC,s,((8*9e-6))/(3e-3)
paget,ledgeC,table
!defining the upper edge of electrode C
path,ueC,5,30,20
ppath,1, ,-8.5e-3,1.5e-3
```

```
ppath,2, ,-9.25e-3,1.5e-3
ppath,3, ,-10e-3,1.5e-3
ppath,4, ,-10.75e-3,1.5e-3
ppath,5, ,-11.5e-3,1.5e-3
pdef,syueC,s,y
pcalc,intg,chrgueC,syueC,s,((8*9e-6))/(3e-3)
paget,uedgeC,table
!defining the lower edge of electrode C
path,loeC,5,30,20
ppath,1, ,-8.5e-3,-1.5e-3
ppath,2, ,-9.25e-3,-1.5e-3
ppath,3, ,-10e-3,-1.5e-3
ppath,4, ,-10.75e-3,-1.5e-3
ppath,5, ,-11.5e-3,-1.5e-3
pdef,syloeC,s,y
pcalc,intg,chrgloeC,syloeC,s,((8*9e-6))/(3e-3)
paget,loedgeC,table
!defining the output charge on electrode C
chargeC_=(redgeC(81,6)+ledgeC(81,6)+uedgeC(81,6)+loedgeC(81,6))/2
!defining the right edge of electrode D
path,reD,5,30,20
ppath,1, ,1.5e-3,-11.5e-3
ppath,2, ,1.5e-3,-10.75e-3
ppath,3, ,1.5e-3,-10e-3
ppath,4, ,1.5e-3,-9.25e-3
ppath,5, ,1.5e-3,-8.5e-3
pdef,sxreD,s,x
pcalc,intg,chrgreD,sxreD,s,((8*9e-6))/(3e-3)
paget,redgeD,table
!defining the left edge of electrode D
path,leD,5,30,20
ppath,1, ,-1.5e-3,-11.5e-3
ppath,2, ,-1.5e-3,-10.75e-3
ppath,3, ,-1.5e-3,-10e-3
ppath,4, ,-1.5e-3,-9.25e-3
ppath,5, ,-1.5e-3,-8.5e-3
pdef,sxleD,s,x
pcalc,intg,chrgleD,sxleD,s,((8*9e-6))/(3e-3)
paget,ledgeD,table
!defining the upper edge of electrode D
path,ueD,5,30,20
ppath,1, ,-1.5e-3,-8.5e-3
ppath,2, ,-0.75e-3,-8.5e-3
ppath,3, ,0,-8.5e-3
ppath,4, ,0.75e-3,-8.5e-3
ppath,5, ,1.5e-3,-8.5e-3
```

```
pdef,syueD,s,y
pcalc,intg,chrgueD,syueD,s,((8*9e-6))/(3e-3)
paget,uedgeD,table
!defining the lower edge of electrode D
path,loeD,5,30,20
ppath,1, ,-1.5e-3,-11.5e-3
ppath,2, ,-0.75e-3,-11.5e-3
ppath,3, ,0,-11.5e-3
ppath,4, ,0.75e-3,-11.5e-3
ppath,5, ,1.5e-3,-11.5e-3
pdef,syloeD,s,y
pcalc,intg,chrgloeD,syloeD,s,((8*9e-6))/(3e-3)
paget,loedgeD,table
!defining the output charge on electrode D
chargeD_=(redgeD(81,6)+ledgeD(81,6)+uedgeD(81,6)+loedgeD(81,6))/2
*status,prm_
FINISH
```

Note:

This code is applicable for creating a PVDF film with four sensing elements and applying the load through a probe which has an equilateral triangular shape with a side of 7mm. When using other probes with different shapes, changing the amount of load or displacing the probe to other points some of the parameters should be changed accordingly.

Appendix 4 – List of all the equipment and their specifications, used for running the experiments

- **Dual Mode Power Amplifier:**

  Model 504E, manufactured by Kistler Instrument Corp.

  Useful amplifier factor: $1\frac{V}{lbf}$

- **Signal Generator:**

  Agilent 33220A

  20 MHz Function/Arbitrary Waveform Generator

- **V203 Vibrator:**

  Made by Ling Dynamic Systems LTD.

  Sine force peak: 17.8 N

  Useful frequency Range: 5 ~ 13000 Hz

  Velocity sine peak: $1.49\frac{m}{s}$

  Amplifier rating: 0.048 kVA

  Displacement peak to peak: 5.0 mm

- **Charge Amplifier Type 2634**

  Amplifier factor: $10\ \frac{mV}{lbf}$

- **Oscilloscope:**

  Agilent 54624A Oscilloscope, 100 MHz, 200 $\frac{\text{MSa}}{\text{s}}$, Controller interface: RS-232

- **Force Transducer:**

  Type 9712B50, Kistler Instrument Corp.

  Sensitivity: 92.9 $\frac{\text{mV}}{\text{lbf}}$

  Measuring range: 50 lbf

  Temperature: -50 ~ 120°C

- **Probe:**

  Aluminum bar, connected to the force transducer, passing force to tactile sensor.

Appendix 5 – Equivalent circuit of the measurement setup

The behavior of a piezoelectric film at low frequencies is fairly straightforward to describe in electronic terms. PVDF has a high dielectric constant in contrast to most of the other polymers. PVDF manufacturers typically measure this property at high frequencies, to say not smaller than 1 KHz, and report it in the specifications sheet. For the biaxial PVDF film used in this study, which was manufactured by the GoodFellow company of the U.S.A., the value of this property is reported as 11 at a frequency of 1 KHz. Since the excitation frequency in the next set of experiments is kept at 20 Hz, it could be suggested that the dielectric constant at this frequency might have a very different value, which translates into a different capacitance value for each sensing element. However, according to some earlier studies, for a pure PVDF film the dielectric constant remains literally constant at a wide range of frequencies [83], even down to 30 Hz. This, coupled with the difficulty of measuring it at such a low frequency, allows the assumption that the dielectric property remains 11 at 20 Hz. It is fair to say that the associated error is negligible. Besides, by using an LCR meter, the capacitances of all four sensing elements were measured at the frequency of 120 Hz. The results further corroborated this assumption because all the capacitances were close to their theoretical values and any existent disparities stemmed from fabrication problems of the sensor.

Equivalent circuit of a piezo film

There are two equally valid models for a piezo film (or each sensing element of the sensor in this sensor). The first one is a "voltage" source in series with a capacitor; the other is a charge generator in parallel with a capacitor. The former is more popular so it will be used in this study to build the electric circuit equivalent of the PVDF film.

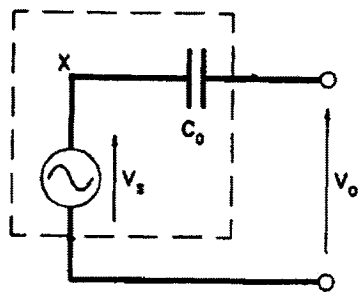

Figure 1 -- Piezo film element as a simple voltage generator

The capacitance of each sensing element, denoted by C_0, can be calculated based on the values of its elements. The voltage source amplitude, denoted by V_o, is equal to the open circuit voltage of a sensing element that can range from microvolts to a couple of volts, depending on the excitation magnitude. This simplified equivalent circuit is of limited value at very high frequencies such as applications in ultrasound transducers. Nevertheless, for low frequency applications, as in this study, it is suitable enough.

Effect of input resistance

The most critical part of an interface circuit is its input resistance (in this case the op-amp buffer or data acquisition card). The input resistance not only affects low frequency

measurement but also the amplitude of the output signal. This is referred to as the "loading effect". The capacitance of each sensing element transforms into impedance, the magnitude of which depends on the frequency of operation and the capacitance measured at a DC circuit. The combination of all these elements produces a voltage divider as shown in Figure 2.

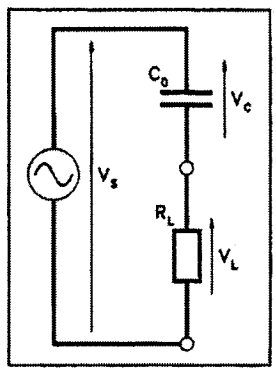

Figure 2 -- The measurement circuit modeled as a voltage divider

V_C is that proportion of the source voltage V_S which is monitored and measured on the computer. The following set of relations and equations helps in determining its magnitude:

$$C = \varepsilon_o \varepsilon_r \frac{A}{d} \quad , \quad X_C = \frac{1}{2\pi f C} \quad ,$$

$$V_C = \frac{X_C . V_S}{\sqrt{X_C{}^2 + R_L{}^2}} = \frac{X_C . V_S}{X_C \sqrt{1 + (\frac{R_L}{X_C})^2}} = \frac{1}{\sqrt{1 + (\frac{R_L}{X_C})^2}} V_S$$

Effect of input capacitance

In addition to input resistance, the input capacitance of an interface circuit can also influence the output electrical charge of sensing elements. This is shown in Figure 3.

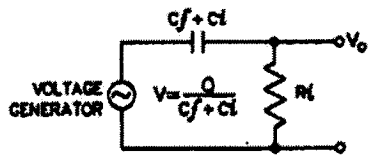

Figure 3 -- Equivalent circuit of a sensing element considering the input capacitance

The input capacitance C_i can be contributed, for instance, by an oscilloscope or a long cable. Since none of these elements exist in the measurement setup, the input capacitance can be ignored. So the circuit shown in Figure 2 suffices for the purposes of this study.

Equivalent circuit of the measurement setup

Referring to Figure 2, the impedance of each sensing element is computed as:

$$X_C = \frac{1}{2\pi fC} = \frac{1}{2\pi(20\,\text{Hz})(35.062\,\text{pF})} = 302.6176\,\text{M}\Omega$$

Unfortunately the precise value of R_L is unavailable. However, it is estimated to be around 500 MΩ. Based on this value, the measured voltage V_C and the developed voltage V_S are related to each other as:

$$V_C = \frac{1}{\sqrt{1+(\frac{R_L}{X_C})^2}} V_S = \frac{1}{\sqrt{1+(\frac{500}{302.618})^2}} = 0.518 V_S$$

Here R_L is the total resistance of the circuit that includes the op-amp buffer, other connections such as solder, copper electrodes and photo resist material in between the faces of each sensing element. It is interesting to observe how the elements of the electronic circuit can attenuate the outputs of the sensing elements. Even if the R_L is taken as being equivalent to X_C, there will be almost 30% drop in voltage at each sensing element. This equivalent circuit is for each of the four sensing elements so there are four circuits in the measurement setup of which each has about the same elements and almost the same amount of parameters.

References

1. Lee M.H. and Nicholls H.R., "Tactile sensing for mechatronics – a state of the art survey", Mechatronics, Vol.9, pp.1-31, 1999.
2. Kawai H., Japan Journal of Applied Physics, Vol.8, No.975, 1969
3. Bergman J.G., McFee J.H. and Crane G.R., Applied Physics Letter, Vol.18, No.203, 1971.
4. Nakamura K. and Wada Y., Journal of Applied Polymer Science, Vol.9, No.161, 1971.
5. GoodFellow company of U.S.A., www.goodfellow.com, 2007.
6. Lang S.B. and Muensit S., "Review of some lesser-known applications of piezoelectric and pyroelectric polymers", Materials Science & Processing, Applied Physics A, Vol.85, pp.125-134, 2006.
7. Lang S.B., Ferroelectrics, Vol.308, No.193, 2004.
8. Razian M.A. and Pepper M.G., "Design, development, and characteristics of an in-shoe triaxial pressure measurement transducer utilizing a single element of piezoelectric copolymer film", IEEE Transactions on Neural Systems and Rehabilitation Engineering, Vol.11, No.3, pp.288-293, 2003.
9. Jiang Z., Funai K., Tanaka M. and Chonan S., "Development of soft tribo-sensor using PVDF film for skin surface contour measurement", Journal of Intelligent Material Systems and Structures, Vol.10, No.6, pp.481-488, 1999.
10. Tanaka M., "Development of tactile sensor for monitoring skin conditions", Journal of Materials Processing Technology, Vol.108, No.2, pp.253-256, 2001.

11. Tanaka M., Furubayashi M., Tanahashi Y. and Chonan S., "Development of an active palpation sensor for detecting prostatic cancer and hypertrophy", Smart Materials and Structures, Vol.9, No.6, pp.878-884, 2000.
12. Dargahi J., "An endoscopic and robotic tooth-like compliance and roughness tactile sensor", Journal of Mechanical Design, Transactions of the ASME, Vol.124, No.3, pp.576-582, 2002.
13. Dargahi J., Parameswaran M. and Payandeh S., "Micromachined piezoelectric tactile sensor for an endoscopic grasper – theory, fabrication and experiments", Journal of Microelectromechanical Systems, Vol.9, No.3, pp.329-335, 2000.
14. Kim D.H., Kim B. and Kang H., "Development of a piezoelectric polymer-based sensorized microgripper for microassembly and micromanipulation", Microsystem Technologies, Vol.10, No.4, pp.275-280, 2004.
15. Taylor G.W., Burns J.R., Kammann S.A., Powers W.B. and Welsh T.R., "The energy harvesting Eel: a small subsurface ocean/river power generator", IEEE Journal of Oceanic Engineering, Vol.26, No.4, pp.539-547, 2001.
16. Ikura M., "Conversion of low-grade heat to electricity using pyroelectric copolymer", Ferroelectrics, Vol.267, pp.403-408, 2002.
17. Ikura M. and Kouchachvili L., "High performance pyroelectric converter", Proceedings of the Sixth IASTED International Conference on European Power and Energy Systems, pp.366-371, 2006.
18. Olsen R.B., Bruno DC.A. and Briscoe J.M., "Pyroelectric conversion cycles", Journal of Applied Physics, Vol.58, No.12, pp.4709-4716, 1985.

19. Shenck N.S. and Paradiso J.A., "Energy scavenging with shoe-mounted piezoelectrics", IEEE Micro, Vol.21, No.3, pp.30-42, 2001.

20. Sohn J.W., Choi S.B. and Lee D.Y., "An investigation on piezoelectric energy harvesting for MEMS power sources", Proceedings of the Institution of Mechanical Engineers, Part C: Journal of Mechanical Engineering Science, Vol.219, No.4, pp.429-436, 2005.

21. Neugschwandtner G.S., Schwodiauer R., Bauer-Gogonea S., Bauer S., Paajanen M. and Lekkala J., "Piezo- and pyroelectricity of a polymer-foam space-charge electret", Journal of Applied Physics, Vol.89, No.8, pp. 4503-4511, 2001.

22. Bauer S., Gerhard-Multhaupt R. and Sessler G.M., "Ferroelectrets: Soft Electroactive Foams for Transducers", Physics Today, Vol.57, No.2, pp.37-44, 2004.

23. Wegener M. and Bauer S., "Microstorms in cellular polymers: A route to soft piezoelectric transducer materials with engineered macroscopic dipoles", ChemPhysChem, Vol.6, No.6, pp.1014-1025, 2005.

24. Screentec Ltd., Oulu, Finland, http://www.screentec.com ,2007.

25. Emfit Ltd., Vaajakoskiv, Finland, http://www.emfit.com ,2007.

26. B-Band Ltd., Vaajakoskiv, Finland, http://www.b-band.com ,2007.

27. Heikkinen L.M., Panula H.E., Lyyra T., Olkkonen H., Kiviranta I., Nevalainen T. and Helminen H.J., "Electromechanical film sensor device for dynamic force recordings from canine limbs", Scandinavian Journal of Laboratory Animal Science, Vol.24, No.2, pp.85-92, 1997.

28. Bauer F., "Metrology of shock waves using piezoelectric polymers", Journal de Physique IV, Vol.1, No.3, pp.427-433, 1991.
29. Bauer F., "Properties of ferroelectric polymers under high pressure and shock loading", Nuclear Instruments & Methods in Physics Research, Section B, Vol.105, No.1-4, pp.212-216, 1995.
30. Coufal H., "Photothermal spectroscopy using a pyroelectric thin-film detector", Applied Physics Letters, Vol.44, No.1, pp.59-61, 1984.
31. Coufal H., "Photothermal spectroscopy of weakly absorbing samples using a thermal wave phase shifter", Applied Physics Letters, Vol.45, No.5, pp.516-518, 1984.
32. Wang C, Mandelis A. and Garcia J.A., "Pd / PVDF thin film hydrogen sensor system based on photopyroelectric purely-thermal-wave interference", Sensors and Actuators B: Chemical, Vol.60, No.2, pp.228-237, 1999.
33. Wang C. and Mandelis A., "Measurement of thermal diffusivity of air using photopyroelectric interferometry", Review of Scientific Instruments, Vol.70, No.5, pp.2372-2378, 1999.
34. Kohler R., Neumann N. and Hofmann G., "Pyroelectric single-element and linear-array sensors based on P(VDF/TrFE) thin films", Sensors and Actuators A (Physical), Vol.A45, No.3, pp.209-218, 1994.
35. Neumann N., Kohler R., Gottfried R. and Hess N., "Pyroelectric sensors and arrays based on P(VDF/TrFE) copolymer films", Integrated Ferroelectrics, Vol.11, No.1-4, pp.1-14, 1995.

36. Binnie T.D., Weller H.J., He Z. and Setiadi D., "Integrated 16×16 PVDF pyroelectric sensor array", IEEE Transactions on Ultrasonics, Ferroelectrics, and Frequency Control, Vol.47, No.6, pp.1413-1420, 2000.

37. Measurement Specialties Inc., U.S.A., http://www.meas-spec.com/myMeas/download/pdf/english/piezo/RB_EG_04.pdf, 2007.

38. Tuzzolino A.J., Economou T.E., McKibben R.B., Simpson J.A., McDonnell J.A.M., Burchell M.J., Vaughan B.A.M., Tsou P., Hanner M.S., Clark B.C. and Brownlee D.E., "Dust flux monitor instrument for the stardust mission to comet wild 2", Journal of Geophysical Research, Vol.108, No. E10, pp. SRD5-1-24, 2003.

39. Brownlee D.E., Tsou P., Anderson J.D., Hanner M.S., Newburn R.L., Sekanina Z., Clark B.C., Horz F., Zolensky M.E., Kissel J., McDonnell J.A.M., Sandford S.A. and Tuzzolino A.J., "Stardust: comet and interstellar dust sample return mission", Journal of Geophysical Research, Vol.108, No. E10, pp.SRD1-1-15, 2003.

40. Luo H. and Hanagud S., "PVDF film sensor and its applications in damage detection", Journal of Aerospace Engineering, Vol.12, No.1, pp.23-30, 1999.

41. Luo H. and Hanagud S., "PVDF sensor and its applications in delamination response detection", Structural Dynamics & Materials Conference, Vol.1, pp.720-728, 1997.

42. Kato T., Yamamoto A. and Higuchi T., "Shape recognition using piezoelectric thin films", IEEE International Conference on Industrial Technology, Vol.1, pt.1, pp.112-116, 2003.

43. Dargahi J., "Piezoelectric and pyroelectric transient signal analysis for detecting the temperature of an object for robotic tactile sensing", Sensors and Actuators – A Physical, Vol.71, pp.89-97, 1998.

44. Fisch A., Mavroidis C., Melli-Huber J. and Bar-Cohen Y., "Haptic devices for virtual reality , telepresence, and human-assistive robotics", in Bar-Cohen Y. and Breazeal C. (Editions), Biologically-Inspired Intelligent Robots, SPIE Press, Bellingham, Washington, 2003.

45. Rao N.P., Dargahi J., Kahrizi M. and Prasad S., "Design and fabrication of a microtactile sensor", Canadian Conference on Electrical and Computer Engineering Towards a Caring and Humane Technology, Montreal, Canada, 2003.

46. Crowder R.M., Automation and Robotics, available at: www.soton.ac.uk/~rmcl/robotics/artactile.htm., 1998.

47. Dargahi J. and Payandeh S., "Surface texture measurement by combining signals from two sensing elements of a piezoelectric tactile sensor", Proceedings of the SPIE International Conference on Sensor Fusion: Architectures, Algorithms and Applications, Orlando, Florida, pp.122-128, 1998.

48. Son J.S., Cutkosky M.R. and Howe R.D., "Comparison of contact sensor localization abilities during manipulation", Robotics and Autonomous Systems, Vol.17, No.4, pp.217-233, 1996.

49. Wen Z., Wu Y., Zhang Z., Xu S., Huang S. and Li Y., "Development of an integrated vacuum microelectronic tactile sensor array", Sensors and Actuators A: Physical, Vol. 103, No.3, pp.301-306, 2003.

50. Jacoff A., Messina E. and Evans J., "Performance evaluation of autonomous mobile robots", Industrial Robot: An International Journal, Vol.29, No.3, pp.259-267, 2002.

51. Harsanyi G., "Polymer films in sensor applications: a review of present uses and future possibilities", Sensor Review, Vol.20, No.2, pp.98-105, 2000.

52. Dargahi J. and Najarian S., "An endoscopic force position grasper with minimum sensors", Canadian Journal of Electrical and Computer Engineering, Vol.28, Nos ¾, pp.155-161, 2004c.

53. Sodhi D.S., "Crushing failure during ice-structure interaction", Engineering Fracture Mechanics, Vol.68, Nos.17-18, pp.1889-1921, 2001.

54. Lehtinen H., Kaarmila P., Blom M., Kauppi I. and Kerva J., "Mobile robots evolving in industrial applications", Proceedings of the 31st International Symposium on Robotics, Montreal, pp.96-101, 2000.

55. Miyaii K., Sugiura S., Inaba H., Takamoto S. and Omata S., "Myocardial tactile stiffness during acute reduction of coronary blood flow", The Annals of Thoracic Surgery, Vol.69, No.1, pp.151-155, 2000.

56. Dargahi J., Eastwood A. and Kemp I.J., "Combined force and position polyvinylidene fluoride (PVDF) robotic tactile sensing system", Proceedings of SPIE International Conference, Orlando, Florida, pp.20-25, 1997.

57. Singh H., Dargahi J. and Sedaghati R., "Experimental and finite element analysis of an endoscopic tooth-like tactile sensor", Proceedings of the Second IEEE International Conference on Sensors, Toronto, Canada, 2003.

58. Dargahi J., Payandeh S. and Parameswaran M., "A micromachined piezoelectric teeth-like laparoscopic tactile sensor: theory, fabrication, and experiments", Proceedings of IEEE International Conference on Robotics and Automation, pp.299-340, 1999

59. Gaspari A. and Di Lorenzo N., "State of the art of robotics in general surgery", Business Briefing: Global Healthcare, pp.1-6, 2002.

60. Sastry S.S., Cohn M. and Tendick F., "Millirobotics for remote, minimally invasive surgery", Robotics and Autonomous Systems, Vol.21, No.3, pp. 305-316, 1997.

61. Uchio Y., Ochi M., Adachi N., Kawasaki K. and Iwasa J., "Arthroscopic assessment of human cartilage stiffness of the femoral condyles and the patella with a new tactile sensor", Medical Engineering & Physics, Vol.24, No.6, pp.431-435, 2002.

62. Dario P., "Tactile sensing-technology and applications", Sensors and Actuators A Physical, Vol.26, pp.251-261, 1991.

63. Dario P. and Buttazzo G., "An anthropomorphic robot finger for investigating artificial tactile perception", International Journal of Robotics Research, Vol.6, No.3, pp.25-48, 1987.

64. Dargahi J., Normandeau M., Milne J., Parameswaran M. and Payandeh S., "A microstrain gauge endoscopic tactile sensor using two sensing elements",

Proceedings of the SPIE International Conference on Sensor Fusion: Architecture, Algorithms, and Applications, Orlando, Vol.4051, pp.349-357, 2000.

65. Dargahi J., "A study of the human hand as an ideal tactile sensor used in robotic and endoscopic applications", Proceedings of the CSME International Conference, Montreal, Canada, pp.21-22, 2001a.
66. Dargahi J., "A study of the human hand as an ideal tactile sensor used in robotic and endoscopic applications", Proceedings of the CSME International Conference, Montreal, Canada, pp.21-22, 2001b.
67. Lee M.H. and Nicholls H.R., "Tactile sensing for mechatronics – a state of the art surgery", Mechatronic, Vol.9, No.1, pp.1-31, 1999.
68. Reston R.R. and Kolesar E.S., "Robotic tactile sensor array fabricated from a piezoelectric polyvinylidene fluoride film", National Aerospace and Electronics Conference, Daton, USA, pp.1139-1144, 1990.
69. Kolesar E.S., Reston P.R., Ford D.G. and Fitch R.C., "Multiplexed piezoelectric polymer tactile sensor", Journal of Robotic Systems, Vol.9, No.1, pp.37-63, 1992.
70. Dargahi J., "A piezoelectric tactile sensor with three sensing elements for robotic, endoscopic and prosthetic applications", Sensors and Actuators Physical A, Vol.80, pp.23-30, 2000.
71. Dargahi J. and Najarian S., "A supported membrane type sensor for medical tactile mapping", Sensor Review Journal, Vol.24, No.3, pp.284-297, 2004.
72. Timoshenko S. and Woinowsky-Krieger S., "Theory of plates and shells", 2nd edition, McGraw-Hill, 1959.

73. Timoshenko S., Weaver W. and Young D.H., "Vibration problems in engineering", 5th edition, John Wiley & Sons, 1990.

74. Ölçer Nurettin Y., "General solution to the equation of the vibrating membrane", Journal of Sound and Vibrations, Vol.6, No.3, pp.365-374, 1967.

75. Laura P.A.A., Rossit C.A. and Malfa S.La, "Transverse vibrations of composite, circular annular membranes: exact solution", Journal of Sound and Vibration, Vol.216, No.1, pp.190-193, 1998.

76. Wei G.W., "Vibration analysis by discrete singular convolution", Journal of Sound and Vibration, Vol.244, No.3, pp.535-553, 2001.

77. Žitňan P., "Vibration analysis of membranes and plates by a discrete least squares technique", Journal of Sound and Vibration, Vol.195, No.4, pp.595-605, 1996.

78. York II Allen R., Sulsky Deborah and Schreyer Howard L., "The material point method for simulation of thin membranes", International Journal for Numerical Methods in Engineering, Vol.44, pp.1429-1456, 1999.

79. Katsikadelis J.T., Nerantzaki M.S. and Tsiatas G.C., "The analog equation method for large deflection analysis of membranes. A boundary-only solution", Computational Mechanics, Vol.27, pp.513-523, 2001.

80. Katsikadelis J.T. and Tsiatas G.C., "The analog equation method for large deflection analysis of heterogeneous orthotropic membranes: a boundary-only solution", Engineering Analysis with Boundary Elements, Vol.25, pp.655-667, 2001.

81. Katsikadelis J.T. and Nerantzaki M.S., "The boundary element method for nonlinear problems", Engineering Analysis with Boundary Elements, Vol.23, pp.365-373, 1999.

82. Brignell J. and White N., "Intelligent Sensor Systems", Institute of Physics Publishing, 1996.

83. Mohamed N.S. and Arof A.K., "Investigation of electrical and electromechanical properties of PVDF-based polymer electrolytes", Journal of Power Sources, Vol.132, pp.229-234, 2004.